TU

TECHNISCHE UNIVERSITÄT WIEN

Dissertation

Precipitation strengthening in multi-particle systems

ausgeführt zum Zwecke der Erlangung des akademischen Grades eines Doktors der technischen Wissenschaften unter der Leitung von

O.Univ.Prof. Dipl.-Ing. Dr.techn. Ernst Kozeschnik

E308

Institute of Materials Science and Technology

eingereicht an der Technischen Universitat Wien

Faculty of Mechanical and Industrial Engineering

von

Mohammad Reza Ahmadi

0928570

Dr. Bruno Buchwieser-Gasse 1 No. 1213, Mödling, 2340, Austria

Wien, am August 2014 **Mohammad Reza Ahmadi**

تقدیم به ساحت مقدس حضرت ولی عصر (عج)، پدر و مادرم

To my Father and mother

Acknowledgment

It has been a valuable and fruitful time during my study in at the Institute of Materials Science and Technology of Vienna University of Technology in Austria. I have received technical advice, motivation and encouragement from a number of people working in our group. At first, I appreciate to my supervisor Professor Ernst Kozeschnik for his valuable guidance through my doctoral thesis. I have learnt so much from him not only in my Ph.D title but also I have learnt the correct way of research. I have also received worthy advice and helpful discussion from Dr. Falahati. I am grateful to professor Christof Sommitsch for accepting review of this work. I express thank to my friends and colleagues of the Institute for their assistance and making enjoyable working environment, particularly, Erwin, Bernhard, Lawrence, Peter, Beatrix, Anette, Heinz, Tomasz, Yao, Matthias, Mohammadian, Alice, Piotr, Markus Rath, Siamak, Markus Kozeschnik, Carina, Roman, Christian, Stefan and, especially, Kerem Ilyas Öksüz that we have a pleasure time in the same office.

I owe an extra special thank you to my father and my wife, who encouraged me, and to my mother, who supported me in all respects.

Introduction of present research

Precipitation strengthening is one of the main strengthening mechanisms in crystalline materials, which has been discovered more than hundred years ago. The primary progress in precipitation strengthening was focused on experimental results. In 1940, Mott and Nabarro investigated this mechanism more scientifically by considering interaction between a dislocation and particle. Evaluation of the yield strength by this mechanism is complex, when randomly distributed precipitates have different sizes during aging. To advance strengthening equations for simulation of the yield strength, a set of simplification were applied, which decreased the accuracy of simulations substantially.

In the present thesis, main focus is put on the development of strengthening equations based on physical parameters instead of existing phenomenological parameters. In the following, the highlights of some selected publications of the author are summarized and discussed briefly.

Kurzfassung

Die vorliegende Dissertation beschreibt die Hauptaspekte eines physikalischen Modells für Ausscheidungshärtung in kristallinen Werkstoffen. Für die Evaluierung des Anstiegs der Streckgrenze wird ein System von Gleichungen abgeleitet, basierend auf der Interaktion zwischen Versetzungen und Ausscheidungen. Verschiedene Schermechanismen und Mechanismen ohne Scherung werden, basierend auf den zugrunde liegenden physikalischen Parametern, kritisch diskutiert. Der in dieser Dissertation verfolgte Ansatz erlaubt uns auch, Gleichungen für die Härtung nicht-sphärischer Ausscheidungen zu entwickeln, wobei der effektive Radius von der relativen Orientierung zwischen Partikel und der Richtung der Versetzungswanderung abhängt. Die Genauigkeit des Modells wird mittels Simulation der Streckgrenzenentwicklung in ausscheidungsgehärteter Ni-Basis Superlegierung Allvac® 718PlusTM validiert.

Abstract

The present thesis describes the main aspects of a physical model for precipitation strengthening in crystalline materials. For evaluation of the yield strength increase, a set of equations is derived based on the interaction between dislocations and precipitates. Different shearing and non-shearing mechanisms are discussed critically based on the underlying physical parameters. The approach followed in this thesis enables us to develop strengthening equations for non-spherical precipitates, too, where the effective radius is depending on the relative orientation between particle and the direction of dislocation movement. The accuracy of the model is verified by simulation of the yield strength evolution in the precipitation-strengthened Ni-base superalloy Allvac® 718Plus™.

Table of Contents

1 Introduction

Precipitation strengthening (or precipitation hardening) has been discovered more than hundred years ago by Wilm in Al-alloys containing Cu and Mg (Duralumin) [1]. During 1903-1911, Duralumin became one of the most demanded alloys by industry. The first fundamental investigations on the mechanism of precipitation and aging of Duralumin were carried out by Merica et al. [2, 3]. By 1932, more than hundred precipitation hardening systems with fourteen base metals were explored by these researchers and reviewed comprehensively by Cahn [4].

The present concept of precipitation hardening is based on the work of Mott and Nabarro [5] proposed in 1940. In their model, Mott and Nabarro investigated the interaction between a single dislocation and the internal stress surrounding a particle, which causes strengthening. In a consistent and comprehensive theory, Orowan [6] first formulated an equation, which describes the interaction between dislocations and non-shearing particles. Later, Ashby [7] modified the Orowan equation to the form, which is currently used most often in calculation of the yield strength increase due to precipitation. In 1971, Brown and Ham [8] published a comprehensive critical review, in which they outline some improvement of models for different strengthening mechanisms. Their work was followed up by Ardell in 1985 [9]. This author proposed simplifications of previous physical models, in order to use the strengthening equations more conveniently. For this purpose, phenomenological components in the treatment of phase fractions and assumptions such as, for instance, distribution of particles with the same size, were introduced. Some uncertainty in determination of input parameters remained, however, such as the dislocation type (edge or screw) or chemical energies and the shear modulus of precipitates.

In the present thesis, focus is put on a deeper understanding of the interplay of *physical parameters* in the original models. Additionally, new developments of physical parameters, such as, a recent description of the 2D distance between randomly arranged particles by Sonderegger et al. [10], are incorporated in the yield strength expressions. The conventional strengthening equations of coherent and strong precipitates, as proposed by Brown and Ham [8], are modified and strengthening equations for non-spherical precipitates are developed [11]. Finally, a comprehensive set of equations is

presented for a predictive evaluation of the yield strength and verified on example of the Ni-base superalloy Allvac® 718Plus™ during aging.

2 The precipitation strengthening model

In this section, the basic concepts behind our strengthening model are formulated in terms of the dislocation line tension and resistance force caused by precipitates. For a quantitative description of the dislocation – particle interaction, energy changes along the dislocation and inside and around the precipitate are the key input quantities.

2.1 Dislocation line tension *T*

For the evaluation of the dislocation line tension, first, the energy content of a linear dislocation in an isotropic elastic crystal far from the surface and other dislocations is formulated. In this case, the dislocation energy depends on the orientation of the dislocation in the crystal. The dislocation line tension, counted per unit length of dislocation, has been calculated by Cottrell [12] and Foreman [13] as

$$E(\theta)=\frac{G b^2}{4\pi}\left(\frac{1-\upsilon(\cos\theta)^2}{1-\upsilon}\right)\ln\left(\frac{r_o}{r_i}\right), \qquad (1)$$

where G is the shear modulus, θ is the angle between the dislocation line and its Burgers vector, b is the magnitude of the Burgers vector, υ is Poisson's ratio, and r_o is the outer cut-off distance. r_o is the distance to the closest parallel dislocation of opposite sign, which is the distance between two particles along the dislocation line for shearable precipitates [8, 9] and the average planar particle diameter for non-shearable precipitates [7, 9]. r_i is the inner cut-off distance, which is the dislocation core radius with values between b and $4b$ [9]. The energy of the dislocation, $E(\theta)$, is a function of the angle θ between the Burgers vector and the tangent to the dislocation line. Since θ=0 for screw dislocations and θ=π/2 for edge dislocations, the character of a dislocation determines its energy. Eq. (1) shows that an edge dislocation stores more energy compared to a screw dislocation.

The difference between the dislocation energy and the line tension, $T(\theta)$, which also depends on θ, according to the relation given by Brown and Ham [8] is proposed as

$$T(\theta)=E(\theta)+\frac{d^2E(\theta)}{d\theta^2}, \qquad (2)$$

and, finally,

$$T(\theta)=\frac{G b^2}{4\pi}\left(\frac{1+\upsilon-3\upsilon(\sin\theta)^2}{1-\upsilon}\right)\ln\left(\frac{r_o}{r_i}\right). \quad (3)$$

In the following treatment, the symbol T for $T(\theta)$ is used and the angle dependence for the sake of brevity is omitted explicitly in writing.

2.2 Interaction between dislocations and precipitates

The process of bowing out of a dislocation between spherical precipitates as a consequence of an external shear force is described by the equilibrium between the line tension T of the dislocation, the dislocation bending angle (outer cut-off angle) Ψ and the critical resolved shear stress τ with the precipitate resistance force F. According to [8], this equilibrium, which is shown in Fig. 1, is expressed as

$$\tau b L=2T\cos\frac{\Psi}{2}=F. \quad (4)$$

In this equation, τ is the external shear stress and L is the distance between two particles along the dislocation.

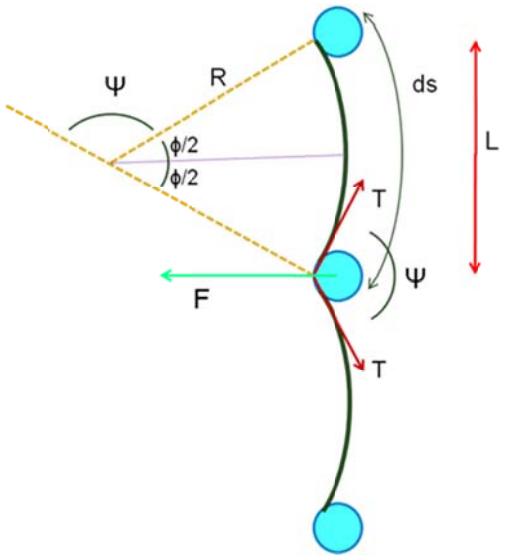

Fig. 1. Balance force between a precipitate and a dislocation

2.3 Shearing mechanisms

When dislocations enter and shear (cut) a spherical precipitate, the maximum resistance force exerted by the precipitate is proportional to the projection of the dislocation line

tension in the direction of movement $F_m = 2T\cos(\Psi_c/2)$, as depicted in Fig. 1. If the critical outer cut-off angle is between 120°≤Ψc≤180°, a particle is denoted as *weak* and shearable. Between 0°≤ Ψ_c≤120°, the particle is considered as *strong* and shearable. The angle Ψ_c strongly depends on the size of the particle and dislocation character.

For weak and shearable particles, it is assumed that ϕ_c=sin ϕ_c = *ds/R,* where *R* is the radius of the dislocation curvature at the critical breaking stress. Accordingly, Eq. (4) is simplified (see Fig. 1) as

$$\tau = \frac{2T}{bL_{\text{eff}}}\cos\frac{\Psi_c}{2}. \qquad (5)$$

In this equation, L_{eff} is the distance between two precipitates along the dislocation in the critical configuration for weak and shearable particles. L_{eff} is different from the surface to surface distance between two particles, L_s, because, for weak and shearable precipitates, dislocations cut the precipitates when the outer cut-off angle is between 120°≤ Ψ_c ≤180° and are released from the particle sooner. Consequently, the distance between two precipitates is increased along the dislocation, and $L_{\text{eff}} > L_s$. This effect is shown schematically in Fig. 2.

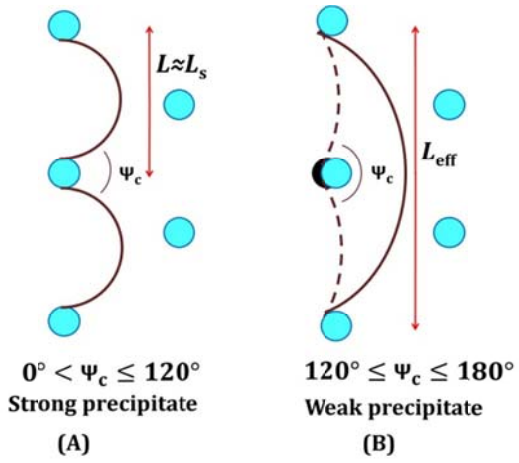

Fig. 2. Free distance between two precipitates along dislocation line in a random array. (a) The precipitates are shearable and strong. (b) The precipitates are shearable and weak.

The relation between L_s and L_{eff} has been evaluated by Friedel [14] between too small particles with

$$L_s = L_{eff}\left[\cos\frac{\Psi_c}{2}\right]^{\frac{1}{2}}. \quad (6)$$

Using Eqs. (4)-(6), one obtains

$$\tau = \frac{2T}{b\,L_s}\left[\frac{F_m}{2T}\right]^{\frac{3}{2}}. \quad (7)$$

Eq. (7) represents a general relation, which is used to express the shear stress according to different strengthening mechanisms for weak and shearable precipitates. Eq. (4) is applicable for strong and shearable precipitates by assuming $L = L_s$ at the critical value when $\Psi = \Psi_c$ (see Fig. 2(A)) as

$$\tau = J\frac{2T\left[\cos\left(\Psi_c/2\right)\right]}{b\,L_s} = J\frac{F_m}{b\,L_s}. \quad (8)$$

F_m corresponds to the maximum resistance force of precipitates that can be achieved and it is formulated for different strengthening mechanisms contributing to shearing, subsequently.

In this equation, the parameter J is a correction coefficient, which depends on the mean free distance between particles. A value of J=0.8 is used, based on the Ashby model [7] for random arrangement of particles instead of particles in an ordered, periodic arrangement. Using the Sonderegger model [10], the free distance L_s between two particles can alternatively be calculated from Eqs. (38)-(39), later. A constant value of J=1 is used in this case.

2.3.1 Coherency effect

If a precipitate is embedded coherently in some given matrix phase, the difference between lattice parameters of matrix and precipitate produces a strain field, which potentially interacts with a moving dislocation. Depending on the magnitude of misfit, this mechanism often provides the most important strengthening contribution for coherent particles.

2.3.1.1 Weak and shearable precipitates

Gerold and Haberkorn [15] proposed a strengthening model for weak and shearable precipitates based on isotropic elasticity theory. Accordingly, the force F between a straight dislocation and a spherical coherent precipitate on a slip plane is

$$F\left(\frac{z}{\bar{r}}\right)=4Gb\varepsilon\bar{r}\chi\left(\frac{z}{\bar{r}}\right), \tag{9}$$

with

$$\varepsilon=\frac{1}{3}\left(\frac{1+\upsilon}{1-\upsilon}\right)\frac{\Delta a}{a}\approx\frac{2}{3}|\delta|. \tag{10}$$

Here, ε is the constrained strain produced by the stress free strain of lattice misfit δ [16], a is the lattice parameter of the matrix, $\bar{r}$ is the mean radius of precipitates and Δa is the difference between lattice parameters of matrix and precipitate. $\chi\left(z/\bar{r}\right)$ is a function depending on the interaction between the dislocation in the slip plane and the precipitate. z denotes the distance between the slip plane and the precipitate center. The values of the $\chi\left(z/\bar{r}\right)$ function can be expressed by the following functions for an edge dislocation [15],

$$\chi\left(\frac{z}{\bar{r}}\right)=2\left(\frac{z}{\bar{r}}\right)\sqrt{1-\left(\frac{z}{\bar{r}}\right)^2} \quad \text{if} \quad \left(\frac{z}{\bar{r}}\right)^2\le\frac{3}{4}, \tag{11}$$

$$\chi\left(\frac{z}{\bar{r}}\right)=\frac{3\sqrt{3}}{8\left(\frac{z}{\bar{r}}\right)^2} \quad \text{if} \quad \left(\frac{z}{\bar{r}}\right)^2\ge\frac{3}{4}, \tag{12}$$

and for a screw dislocation,

$$\chi\left(\frac{z}{\bar{r}}\right)=\frac{1}{2}\left(\frac{z}{\bar{r}}\right) \quad \text{if} \quad \left(\frac{z}{\bar{r}}\right)\le 1, \tag{13}$$

$$\chi\left(\frac{z}{\bar{r}}\right)=\frac{1}{2\left(\frac{z}{\bar{r}}\right)^2} \quad \text{if} \quad \left(\frac{z}{\bar{r}}\right)\ge 1, \tag{14}$$

By applying the Pythagorean mixture law, as proposed by Brown and Ham [8], and combining Eqs. (7) and (9), strengthening due to the coherency misfit mechanism for weak and shearable precipitates from center of the precipitate up to infinity can finally be expressed as [17]

$$\tau_{\mathrm{Coh,weak}}^{2}=\frac{1}{b^{2}L_{\mathrm{s}}^{2}\,2T}\int_{0}^{\infty}F^{3}\left(\frac{z}{\bar{r}}\right)\frac{dz}{\bar{r}}. \tag{15}$$

For an edge dislocation,

$$\tau_{\mathrm{Coh,weak}}=\left(\frac{592}{35}\frac{G^{3}\,b\,\varepsilon^{3}\left(\bar{r}\right)^{3}}{L_{\mathrm{s}}^{2}\,T\left(\pi/2\right)}\right)^{\frac{1}{2}}, \tag{16}$$

and for a screw dislocation,

$$\tau_{\mathrm{Coh,weak}}=\left(\frac{9}{5}\frac{G^{3}\,b\,\varepsilon^{3}\left(\bar{r}\right)^{3}}{L_{\mathrm{s}}^{2}\,T\left(0\right)}\right)^{\frac{1}{2}}. \tag{17}$$

2.3.1.2 Strong and shearable precipitates

Eq. (15) is used to describe the effect of coherency strain when the size of the precipitates is small or the outer cut-off angle is higher than 120°. In the case of large precipitates, which can bend dislocations to angles below 120°, the Friedel relation, Eq. (6), is no longer valid for Eqs. (15)-(17). The concept of strong precipitates is also dependent on the position of the dislocation in the slip plane with respect to the precipitate (z value). For example, at $\left(z/\bar{r}\right)$=0, a large precipitate acts as weak and shearable. When the $\left(z/\bar{r}\right)$ parameter is confined between $\left(T/\left(4G\varepsilon b\bar{r}\right)\right)\le\left(z/\bar{r}\right)\le\left(3^{1.5}G\varepsilon b\bar{r}/\left(4T\right)\right)^{0.5}$ for edge dislocations, and $\left(T/\left(G\varepsilon b\bar{r}\right)\right)\le\left(z/\bar{r}\right)\le\left(G\varepsilon b\bar{r}/\left(T\right)\right)^{0.5}$ for screw dislocations, precipitates have the capability of producing the bending condition corresponding to a strong precipitate.

In Fig. 3, three different regions, A, B and C, are distinguished to describe the interaction between a screw dislocation and a large precipitate, where region B is strong and shearable, and regions A and C are weak and shearable.

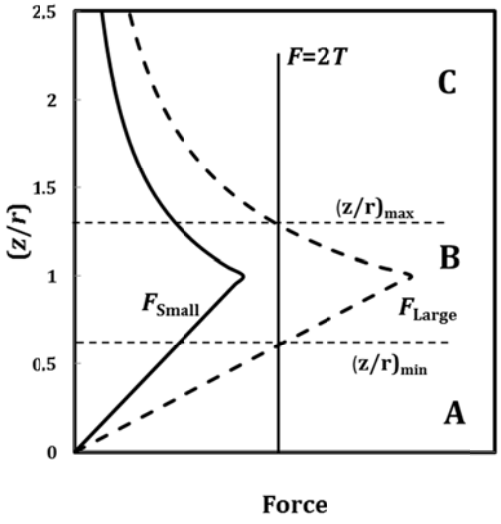

Fig. 3. Resistance force of small and large precipitates, schematically. The interaction between large precipitates and a dislocation produces two 'weak' regions (A and C) and one 'strong' region (B).

Ignoring the effect of the coherency and weak mechanism (c-w) in regions A and C, Brown and Ham [8] proposed an expression for the shear stress increment of strong precipitates, where Ψ is close to 0° but the precipitate still acts as shearable, as [18]

$$\tau_{\text{strong,B\&H}} = J\frac{M\,T}{b\,L_{\text{s}}}\left(\psi(r)\right)^{\frac{1}{4}} = J\frac{M\,T}{b\,r}\sqrt{\frac{3f}{2\pi}}\left(\psi(r)\right)^{\frac{1}{4}}, \tag{18}$$

with

$$\psi(r) = \frac{Gb\varepsilon r}{T}, \tag{19}$$

and

$$f = \left(\frac{2\pi}{3}\right)\left(\frac{r}{L_{\text{s}}}\right)^{2}. \tag{20}$$

f is the precipitate phase fraction. M is a constant equal to 2 and $2^{1/2}\times 3^{3/8}$ for screw and edge dislocations, respectively.

Considering the strengthening effect due to the regions A and C delivers a correction factor [18] for the shear stress of large precipitates for both, edge and screw dislocations with

$$\tau_{\text{total}} = \left\{ \left(\frac{1}{J\sqrt{5}} \right)^{q} + 1 \right\}^{\frac{1}{q}} \times \tau_{\text{strong,B\&H}} \,, \tag{21}$$

where q is a variable between one and two. Eq. (21) shows that identical correction terms of the simplified model description for the yield strength increment of strong precipitates is required for both screw and edge dislocations.

Consequently, the Brown and Ham equation (Eq. (18)) needs a modification to reflect these contributions. If one accepts J = 0.81 as a correction factor for randomly distributed precipitates in a slip plane, and q=1.4 for the mixture of contributions from weak and strong mechanisms [9], the strengthening equation for strong coherent precipitates from Brown and Ham [8] significantly underestimates the strengthening contribution by ~ 30%. This aspect is discussed in detail in ref. [18].

2.3.2 Modulus effect

When a dislocation passes through a precipitate, the dislocation energies inside and outside the precipitate are different due to different chemical composition and/or crystal structure of precipitate and matrix. In 1962, Siems et al. [19] used Snell's Law to explain this mechanism based on the condition

$$U_1 \sin\alpha_1 = U_2 \sin\alpha_2 \,. \tag{22}$$

In this equation, U_1 and U_2 are the dislocation energy inside the precipitate and the matrix, respectively. α_1 and α_2 represent the angles between the dislocation and the normal of the precipitate/matrix interface. This is shown schematically in Fig. 4.

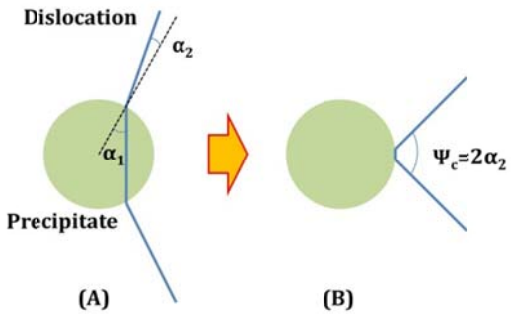

Fig. 4. Dislocation treatment inside precipitate, when Young's modulus of the precipitate is lower than Young's modulus of the matrix.

In the Siems et al. model [20], the dislocation energy inside the precipitate is assumed to be lower than that in the matrix ($U_1 < U_2$). The yield strength increment, due to the weak and shearable conditions, is [21]

$$\tau_{\mathrm{Mod,weak}} = \frac{2T}{b L_{\mathrm{s}}}\left[1-\left(\frac{U_1^2}{U_2^2}\right)\right]^{\frac{3}{4}}. \tag{23}$$

and for strong and shearable precipitates [21], we get

$$\tau_{\mathrm{Mod,strong}} = J\frac{2T}{b L_{\mathrm{s}}}\left[1-\left(\frac{U_1^2}{U_2^2}\right)\right]^{\frac{1}{2}}. \tag{24}$$

with

$$\frac{U_1}{U_2} = \frac{E_{\mathrm{p}}\log\frac{r_s}{r_{\mathrm{i}}}}{E\log\frac{r_{\mathrm{o}}}{r_{\mathrm{i}}}} + \frac{\log\frac{r_{\mathrm{o}}}{r_{\mathrm{s}}}}{\log\frac{r_{\mathrm{o}}}{r_{\mathrm{i}}}}. \tag{25}$$

In this equation, r_s is the equivalent precipitate radius defined in different models. This will be further discussed later. E_{p} is the energy of a dislocation per unit length in infinite media of precipitate.

In 1983, Nembach [22] considered modulus strengthening numerically by evaluating the interaction force between a dislocation and a spherical precipitate with different shear modulus from the matrix. In this model, the maximum interaction force becomes

$$F_{\mathrm{m}} = \omega_1\left|G_{\mathrm{p}} - G\right| b^2\left(\frac{r_s}{b}\right)^{\omega_2}. \tag{26}$$

where ω_1 and ω_2 are constants representing the dislocation core energy inside and outside the precipitate. Depending on the models used in [22], ω_1 varies from 0.0175 to 0.0722. ω_2 adopts a value of 0.81±0.09. By replacing the force in Eqs. (7) and (8) with F_{m} in Eq. (26), the shear stress according to the weak and strong modulus mechanism will be defined.

In the model of Nembach [22], the absolute value of the difference in shear modules between precipitate and matrix enters the equation. Consequently, this model applies to both situations, where the modulus of the precipitate is larger or smaller, as well.

2.3.3 Chemical effects

Dislocations entering a particle lead to breaking of chemical bonds. The rearrangement of chemical bonds into a different local chemical environment leads to strengthening. Generally, this effect is denoted as *chemical strengthening*. It is commonly distinguished between anti-phase boundary, stacking fault and interfacial effects.

2.3.3.1 Anti-phase boundary effect

If particles in a matrix show chemical ordering, the anti-phase boundary effect often represents the major strengthening mechanism. When a dislocation passes through an ordered precipitate, it destroys the periodic atomic arrangement in its slip plane. The disordered plane, which is left behind, is called anti-phase boundary (APB).

In ordered crystal structures, the shearing dislocations travel in groups, where the number of dislocations in a group depends on the type of order structure (e.g. face-centered cubic $L1_2$, tetragonal $D0_{22}$). This observation is important for the interpretation of the ability of precipitates to restore to the perfect order structure after the precipitate-dislocation interaction. The first dislocation, which is denoted as leading dislocation, creates an anti-phase boundary in the precipitate. The second one, which is called trailing dislocation, compensates the effect of the first one and restores the ordered structure again. Depending on the size of the precipitate, two regimes are distinguished.

2.3.3.1.1 Weak and shearable precipitates

This regime is operative if the precipitates are small, i.e. the outer cut-off angle is Ψ_c >120°. The disordered precipitates stimulate the trailing dislocations towards the leading dislocation. This compensates, partly, the APB strengthening effect of the leading dislocation. The strengthening equation for the APB effect can be expressed by using Eq. (27) with $F_m=2\gamma_{APB}\, r_s$ as [17]

$$\tau_{\mathrm{APB,weak}} = \frac{2}{s}\left\{\frac{2T}{b\,L_s}\left[\frac{2\gamma_{\mathrm{APB}}\,r_s}{2T}\right]^{\frac{3}{2}} - \beta\zeta\left(\frac{r_s}{L_{\mathrm{s}}}\right)\right\}. \tag{27}$$

where γ_{APB} is the anti-phase boundary energy of the precipitate and β is a constant between 0.0 and 1.0. β is close to 1.0 when the trailing dislocation is straight. s is the number of pair dislocations in the group and the function $\zeta(r_s/L_{\mathrm{s}})$ corresponds to the pulling tension of precipitates on the trailing dislocation. It is given as [23]

$$\zeta\left(\frac{r_s}{L_{\mathrm{s}}}\right) = \frac{16}{3\pi}\frac{\gamma_{\mathrm{APB}}\,r_s^2}{bL_{\mathrm{s}}^2}. \tag{28}$$

2.3.3.1.2 Strong and shearable precipitates

When the precipitates are large, application of Eq. (27) becomes critical because the precipitates produce a high APB force. Hüther and Reppich [24] obtained a general expression for strong and shearable ordered particles as

$$\tau_{\mathrm{APB,strong}} = \left(\frac{2V\,T}{\pi\,b\,L_{\mathrm{s}}}\right)\left(\frac{\pi\,\gamma_{APB}\,r_s}{V\,T} - 1\right)^{\frac{1}{2}}. \tag{29}$$

where V is a parameter introduced for remaining dislocation segments incorporating also some other uncertainties. Its value is assumed to be 2.8 in ref. [25].

2.3.3.2 Stacking fault effect

In some crystalline materials, the dislocation energy of a single dislocation can be reduced by dissociation into two partial dislocations. This process leads to a stacking fault (SF) in the slip plane between the partial dislocations 1 (P.1) and 2 (P.2). When the stacking fault energy (SFE) of the precipitate is lower than that of the matrix, the width of the ribbon band between two partials inside and outside of the precipitate differs. This difference produces a retarding force in front of the dislocation movement, which depends on the precipitate size and the width of the stacking fault in the matrix W_{m} and inside the precipitate W_{p}. Hirsch and Kelley [26] derived the maximum force as

$$F_{\mathrm{m}} = 2\left(\gamma_{\mathrm{SFM}} - \gamma_{\mathrm{SFP}}\right)\left(W_{\mathrm{eff}}\,r_s - \frac{W_{\mathrm{eff}}^2}{4}\right)^{\frac{1}{2}}, \tag{30}$$

$$W_{\text{eff}} = \frac{2K(\theta)}{(\gamma_{\text{SFM}} + \gamma_{\text{SFP}})}, \tag{31}$$

$$K(\theta) = \frac{G b_{\text{p}}^2 (2-\upsilon)}{8\pi(1-\upsilon)}\left(1 - \frac{2\upsilon\cos(2\theta)}{(2-\upsilon)}\right). \tag{32}$$

W_{eff} is the distance between P.1 and P.2, when P.1 is located at the precipitate circumference, $K(\theta)$ is the elastic energy per unit length between two partial dislocations and b_{p} is the magnitude of the Burgers vector in the precipitate. On replacing F_{m} in Eqs. (7) and (8) by Eq. (30), finally, the yield stress increment for the weak mechanism is obtained.

2.3.3.3 Interfacial effect

When a dislocation cuts a coherent precipitate, two new ledges form. One is created after entering the precipitate, the other one after leaving it. These ledges cause an increment in the interfacial area in these regions. The maximum force related to this mechanism is expressed by $F_{\text{m}}=2\gamma_{\text{IFE}}$ b [9], where γ_{IFE} is the energy of the precipitate-matrix interface created by dislocation slip. Replacing F_{m} in Eqs. (7) and (8) delivers the yield strength increment due to the interfacial effect.

2.4 Non-Shearing mechanism

Ashby [7] suggested a widely used expression for the ultimate shear stress related to non-shearable precipitates. He introduced simplifying assumptions for the outer cut-off radius of the precipitate into the original Orowan equation and, furthermore, made assumptions on the dislocation character. Ashby considered the exact shape of the dislocation when a dislocation approaches a Frank-Read configuration between two precipitates. In this situation, which is shown in Fig. 1, the dislocation escapes the precipitate as soon as the outer cut-off radius reaches an angle of Ψ=0. Brown and Ham [8] approximated the condition of randomly distributed obstacles and formulated the critical shear stress as,

$$\tau_{\text{Orowan}} = J\frac{2\left[E(0).E(\pi/2)\right]^{0.5}}{b\,L_{\text{s}}}. \tag{33}$$

Insertion of Eq. (1) with θ=0 and θ=π/2 in Eq. (33) restores the well-known Orowan equation, which is,

$$\tau_{\text{Orowan}} = \frac{J\,G\,b}{2\,\pi\,\sqrt{1-\upsilon}\,L_{\text{s}}}\ln\left(\frac{2\,r_{s}}{r_{\text{i}}}\right). \tag{34}$$

3 Discussion

The present set of strengthening equations shows that the maximum shear stress before yielding depends on the dislocation line tension T, the mean distance between two particles, the precipitate resistance force F, which is a function of precipitate radius or outer cut-off radius, and the particular strengthening mechanism. In contrast, conventional strengthening equations are often functions of the mean radius, phase fraction as well as physical and phenomenological coefficients [6-9, 15, 21-23, 27, 28]. When substituting the actual precipitate distribution by only the mean radius and phase fraction of precipitates, the calculated yield strength increments can become substantially different from experimental results. The differences usually arise from simplifications in the development of the strengthening equations. The most prominent are displayed in Fig. 5.

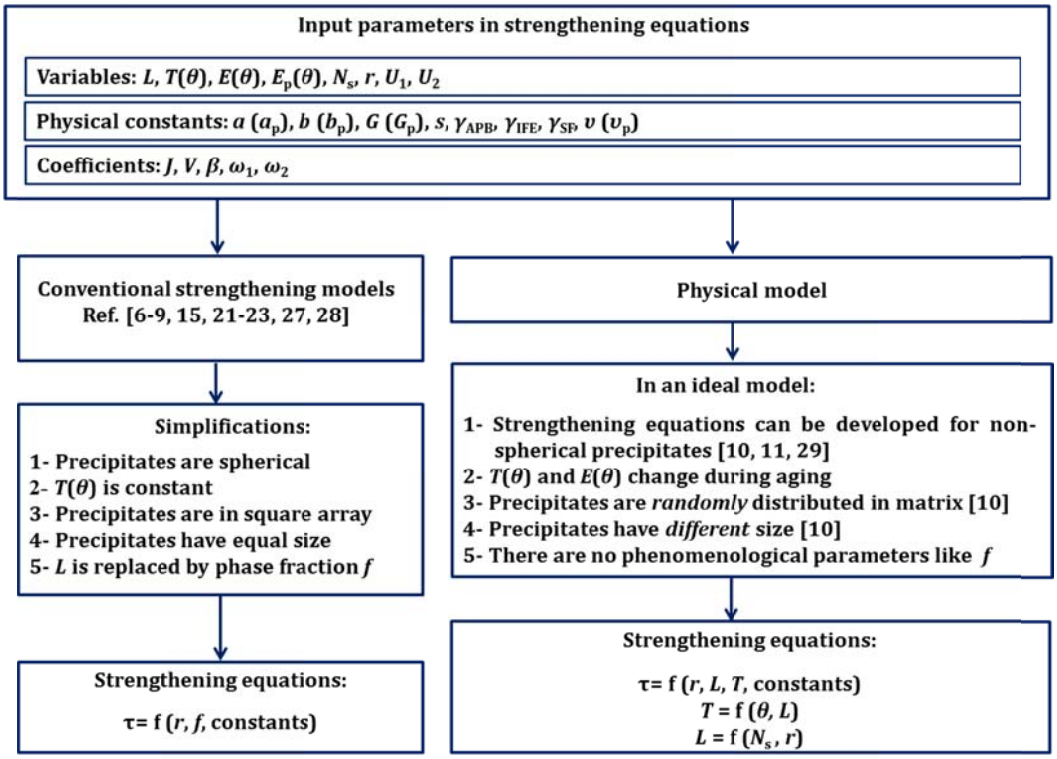

Fig. 5. Evolution of yield strength equations in conventional and physical model

For a predictive simulation of the total shear stress, refining the values of input variables instead of changing and adapting phenomenological coefficients in order to close the gap between experimental and simulation results are proposed. In a survey for evaluation of final yield strength in binary Ni-Al system, Ardell and Huang [30] have listed eight

different values between 0.129 J/m^{-2} and 0.188 J/m^{-2} for the anti-phase boundary energy (γ_{APB}) of γ' from different references, while Douin et al. [31] measured γ_{APB}=0.111 J/m^{-2} by using weak-beam electron microscopy.

In the present model, the strengthening equations are connected to the incipient physical parameters, which are varying during aging and unnecessary simplifications commonly used in conventional models are avoided. This is discussed in detail later.

3.1 Non-spherical precipitates

In some precipitation strengthening systems, for instance, Al-Mg-Si, Al-Cu, Al-Cu-Mg, Al-Zn-Mg and some Ni-base superalloys (Inconel 718, Rene 62, Udimet 630), precipitates are non-spherical. For these cases, the conventional strengthening equations are not applicable and it is difficult to advance these equations on a rigorous basis as long as they contain purely phenomenological parameters. Three different approaches are reported in literatures to simulate the yield strength for non-spherical precipitates:

(i) Myhr et al. [32], in the Al-Mg-Si system, assumed that prolate precipitates are spherical and applied conventional strengthening equations, thus simply ignoring the shape effect.

(ii) Nie and Muddle [33] modified the Orowan equation, Eqs. (33)-(34), for cylindrical disc shape precipitates in the Al-Cu-Sn system by using a stereological method. They assumed that the aspect ratio is higher that 40 (diameter / thickness) and simulated the yield strength increment based on this assumption. In their model, they assumed that the precipitates are not shearable at all and ignored all shearing mechanisms. This model has been developed for rod shape precipitates in aluminum and magnesium alloys, too [34, 35].

(iii) Computer simulations of moving dislocations in their slip plane were used in the method of Zhu and Starke [36], where the moving dislocations are crossing rod-shape particles elongated in ⟨100⟩ direction or circular platelet particles extended in the {100} planes [37-39]. Similar to Nie and Muddle [33], this method does not account for the case of coherent and shearable precipitates.

In our approach, as outlined in section 2, the strengthening equations are functions of physical parameters only, which can straightforwardly be advanced for prolate and

oblate precipitates considering all shearing and non-shearing strengthening mechanisms [11, 29].

3.2 Dislocation line tension

The dislocation line tension varies in the course of particle aging processes due to changes in the mean free distance between two particles along the dislocation line and the angle between the dislocation line with the Burgers vector θ due to the dislocation bending behind a particle [40].

In the early stages of aging, precipitates are considered as being weak and the dislocation character remains unaffected when the dislocation is nearly straight. Once the precipitates grow, the dislocation character changes during bending behind the strong precipitates. Dieter [40] measured the dislocation energy per unit length based on Eq. (1) in annealed crystals. He assumed that r_o = 10^{-7} m and r_i =$2{\cdot}10^{-10}$ m; then $\ln(r_o/r_i)\approx 2\pi$. After replacing the parameters for outer and inner cut-off radius and using $\upsilon=1/3$, the resulting dislocation energies for screw and edge dislocations become $E(0)=(1/2)Gb^2$ and $E(\pi/2)=(3/4)Gb^2$, respectively. In the same way, using Eq. (3), the dislocation line tension for screw and edge dislocations are $T(0)=Gb^2$ and $T(\pi/2)=(1/4)Gb^2$, respectively. In contrast, Ardell [9] proposed $\ln(r_o/r_i)\approx 4$ at peak strength. These different assumptions in conventional models produce rather large differences in the absolute value of the strengthening effect, thus indicating that the dislocation line tension is a critical parameter for precipitation strengthening. For simulation of the yield strength, the dislocation line tension is proposed to be $T=(1/2)Gb^2$ in Refs.[8, 9, 15, 21, 24, 26, 39].

In practical simulation, accurate result can only be obtained after performing a thorough characterization of the dislocation character, which is a mixture of edge or screw, and by accurately determining the free distance between two particles. Both these parameters are dynamic in nature and vary during aging.

3.3 Free distance between precipitates

3.3.1 Spherical precipitates

The free distance between two particles is a crucial input quantity in precipitation strengthening theory. In his early model, Ashby [7] assumed that all precipitates have the same size and that they are distributed on a square array without preferential point for nucleation. Based on these assumptions, the free distance between two precipitates, $L_{s,c}$, is represented as [7]

$$L_{s,c} = \left[\frac{1}{\sqrt{N_s}} - 2r_s \right], \tag{35}$$

where $L_{s,c}$ is the surface to surface distance between two particles located in the square arrangement and N_s is the number of particles, which intersect unit area of slip plane. The relation between N_s and the number of particles per unit volume of the matrix, N_v, is

$$N_s = 2\, r\, N_v. \tag{36}$$

Whereas the square array is a reasonable approximation of the real situation for many alloy systems, in other precipitation hardening materials, such as aluminum alloys AA2xxx and AA6xxx or γ''-hardened superalloys, precipitates nucleate in a close-packed triangular array [41]. In this case, $L_{s,c}$ should be modified to the following form, where the surface to surface distance between two particles located in triangular arrangement, $L_{s,t}$, is

$$L_{s,t} = \left[\frac{\sqrt{2/\sqrt{3}}}{\sqrt{2\, r\, N_v}} - 2r_s \right]. \tag{37}$$

In general, strengthening models based on Eqs. (35) and (37) (see the work of Russell and Brown [21], Kelly [42] and Fullman [43]) are physically correct when the ordered precipitates have same sizes. However, their accuracy decreases for small particles with $r<0.04\bar{r}$, where $\bar{r}$ is the mean radius of the precipitate distribution. Moreover, when being applicable for $r<0.04\bar{r}$, the results are not satisfying at $\bar{r}$. The phase fraction of precipitates has a similar effect on the free distance of two particles. In a numerical analysis, Sonderegger et al. [10] simulated the shearing of particles in the dislocation

slip plane for 10^5 randomly distributed precipitates in 100 size classes in volume. They calculated the free distance distribution between two particles by varying radius at constant phase fraction and vice versa. Their simulation result showed that the deviation between classical models and numerical simulation could be 70% and more for the classical models.

These authors presented an alternative model for arbitrary precipitate sizes and randomly distributed particles in a matrix. In this model, precipitates are divided into discrete size classes. Each class contains precipitates from within a specific radius interval, r_c, and a number density of particles, $n_{v,c}$. A general formulation for the free distance between two particles in the slip plane is derived as

$$L_{\mathrm{s}} = \sqrt{\frac{\ln 3}{2\pi \sum_{c} n_{v,c} r_c} + \left(2 r_{ss}\right)^2} - 2 r_{ss}\,, \tag{38}$$

and

$$r_{ss} = \sqrt{\frac{2}{3}} \frac{\sum_{\mathrm{c}} n_{v,c} r_c^2}{\sum_{c} n_{v,c} r_c}\,, \tag{39}$$

where r_{ss} is the mean projected radius. The Sonderegger et al. model delivers more accurate results for various size distributions and different phase fractions. The difference in free distance between two particles obtained from Eq. (38) and numerical analysis described in Ref. [10] is in all cases less than 30%.

3.3.2 Non-spherical precipitates

Eqs. (38) and (39) have been established for spherical particles. For ellipsoid precipitates in fcc structure, Sonderegger and Kozeschnik [29] introduced a correction factor for λ_{ss}, depending on a shape factor h, as

$$L_{\mathrm{s,ell}} = h^{\frac{1}{6}} \cdot \left(\frac{2 + h^2}{3}\right)^{\frac{-1}{4}} L_{\mathrm{s}}\,, \tag{40}$$

$$h = \frac{c}{a}, \tag{41}$$

where $L_{s,ell}$ is the free distance between two ellipsoidal precipitates. c is the half axes of the particle parallel to its rotational axes and a is the according half length perpendicular to the rotational axes. In this model, precipitates can be rotational needle-shaped ellipsoids (prolate particles), which are elongated in <100> directions, or rotational lens-shaped ellipsoids (oblate particles) elongated in {100} planes.

3.4 Equivalent radius

3.4.1 Spherical precipitates

The spatial extension of the interfering part between a dislocation and a precipitate, the so-called equivalent radius, varies between 0 and the radius of the precipitate. There are two approaches to measure the equivalent radius, one by Ardell [9] and the second by Brown & Ham [8]. Ardell considered the projection of the precipitate onto a plane perpendicular to the slip plane of the dislocations. The resulting geometric figure is a circle with radius r and area πr^2. Ardell then replaced this circle by a rectangle with the same area and same height in z direction. The average planar radius in this model is then

$$r_{s,a} = \frac{\pi}{4}\bar{r}. \tag{42}$$

In the Brown and Ham approach, the volume effect is taken into account. Brown and Ham replaced the spherical precipitate by a cylindrical precipitate with the same volume ($4/3\ \pi r^3$) and same height in z direction. The mean radius of the circular section in the dislocation slip plane in this model is [8, 28]

$$r_{s,b} = \sqrt{\frac{2}{3}}\bar{r}. \tag{43}$$

3.4.2 Non-spherical precipitates

3.4.2.1 Shearing mechanism

Eqs. (42) and (43) are applicable for spherical particles, but, in fact, precipitates often have different shapes and orientations. Examples for fcc-structured non-spherical

precipitates are β'' needles oriented in <100> directions in aluminum 6xxx series, and θ'' and γ'' precipitates extended in {100} planes in aluminum 2xxx series and Inconel 718, respectively. In the present modeling, the needle-shaped particles in an fcc-structure are described by the prolate-type precipitate in <100> directions (h>c/a) and the lens-shape precipitates are represented by oblate-type extending in {100} planes (h<c/a) [11].

In the case, where an edge or screw dislocation encounters each precipitate orientation with the same probability, the average mean values $\overline{\omega}_{\mathrm{eq}}$ are found as

$$\overline{\omega}_{\mathrm{eq,edge}}(h)=\left\{\frac{1}{3}\left[\sqrt{\frac{3}{2+h^2}}+2\sqrt{\frac{6}{1+5h^2}}\right]h^{\frac{2}{3}}\right\}r_s, \tag{44}$$

$$\overline{\omega}_{\mathrm{eq,screw}}(h)=\left\{\frac{1}{3}\left[\frac{1}{h}+2\sqrt{\frac{2}{1+h^2}}\right]h^{\frac{2}{3}}\right\}r_s, \tag{45}$$

$$\overline{\omega}_{\mathrm{eq}}(h)=P_1\overline{\omega}_{\mathrm{eq,edge}}(h)+P_2\overline{\omega}_{\mathrm{eq,screw}}(h), \tag{46}$$

where $\overline{\omega}_{\mathrm{eq,edge}}(h)$ and $\overline{\omega}_{\mathrm{eq,screw}}(h)$ are referred to as the *effective equivalent radius* in front of edge and screw dislocations in the slip plane, respectively, and P_1 and P_2 are the fractions of edge and screw dislocations , respectively.

Eq. (46) defines a coefficient for ellipsoidal precipitates for the shearing mechanism. Replacing r_s by $\overline{\omega}_{\mathrm{eq}}(h)$ in strengthening equations introduces a more general relation, which is applicable for spherical precipitates, too [11].

3.4.2.2 Non-shearing mechanism

In the non-shearing mechanism (Orowan mechanism), dislocations are blocked in front of the precipitates and do not shear them. Consequently, the precipitate-dislocation interaction is independent of the intrinsic precipitate properties. The outer cut-off radius, R_{eq}, is the full width of the particles cross-section normal to the direction of dislocation movement.

The geometry of the particles relative to the moving dislocations for the Orowan mechanism is the same as for the shearing mechanism, which leads to mean outer cut-off radii of

$$\overline{R}_{\mathrm{eq,edge}}(h)=\left\{\frac{1}{3}\left[\sqrt{\frac{3}{2+h^2}}+\sqrt{\frac{3}{h^2}+\frac{3}{2+h^2}}\right]h^{\frac{2}{3}}\right\}2\,r_s\,, \tag{47}$$

$$\overline{R}_{\mathrm{eq,screw}}(h)=\left\{\frac{1}{3}\left[\sqrt{\frac{1}{h^2}+\frac{9}{2+h^2}}+\frac{1}{h}\right]h^{\frac{2}{3}}\right\}2\,r_s \tag{48}$$

$$\overline{R}_{\mathrm{eq}}(h)=P_1\overline{R}_{\mathrm{eq,edge}}(h)+P_2\overline{R}_{\mathrm{eq,screw}}(h). \tag{49}$$

where $\overline{R}_{\mathrm{eq,edge}}(h)$ and $\overline{R}_{\mathrm{eq,screw}}(h)$ are referred to as the *equivalent outer cut-off radii* in front of edge and screw dislocations in the slip plane, respectively.

Eq. (49) defines a coefficient for ellipsoidal precipitates in the Orowan mechanism. Replacing $2r_s$ by $\overline{R}_{\mathrm{eq}}(h)$ in Eq. (34) provides a general equation, which is applicable for spherical and ellipsoidal precipitates.

3.5 Superposition of strengthening mechanisms

In precipitation-strengthened multi-component and/or multi-phase materials, the different nature and size of particles will lead to a situation where the total strengthening effect is given by a mixture of different strengthening mechanisms. Even with just one kind of precipitate, a distribution of particle sizes in different slip planes of dislocations must be expected, thus, representing a situation where each precipitate has different strengthening potential and the total strength contribution must in some way be superposed.

For a prediction of the combined effect of all individual strengthening contributions, several investigations have been performed and various approaches exist [8-11, 45-46]. The basic result of these studies can be lumped up in the superposition expression

$$\tau_{\mathrm{total}}^{q}=\sum\nolimits_{i=1}^{n}\Delta\tau_i^{q}\,, \tag{50}$$

where q is an exponent, which commonly lies between 1 and 2. Eq. (50) delivers the shear stress of a precipitation-strengthened material with a mixture of operative strengthening mechanisms.

Numerical studies of Forman and Makin [47] for two types of obstacles with the same strength provide good agreement to the overall strength with a value of q=2 (Pythagorean superposition). The same result is also proposed by Koppenaal [46]. In another investigation, Ardell [9] applied computer simulations to determine the value of q for a mixture of two randomly distributed precipitate populations with distinct strength. He proposed that, for a combination of just weak mechanisms (WM) or just strong mechanisms (SM), q should be chosen close to 1.8. Otherwise, when two different mechanisms of weak and strong type are acting together, q should be given a value close to 1.4. Merging of weak and strong mechanisms in a multi-particle system (1, 2, ...) is demonstrated in Fig. 6 for the simplified case of only two particle types.

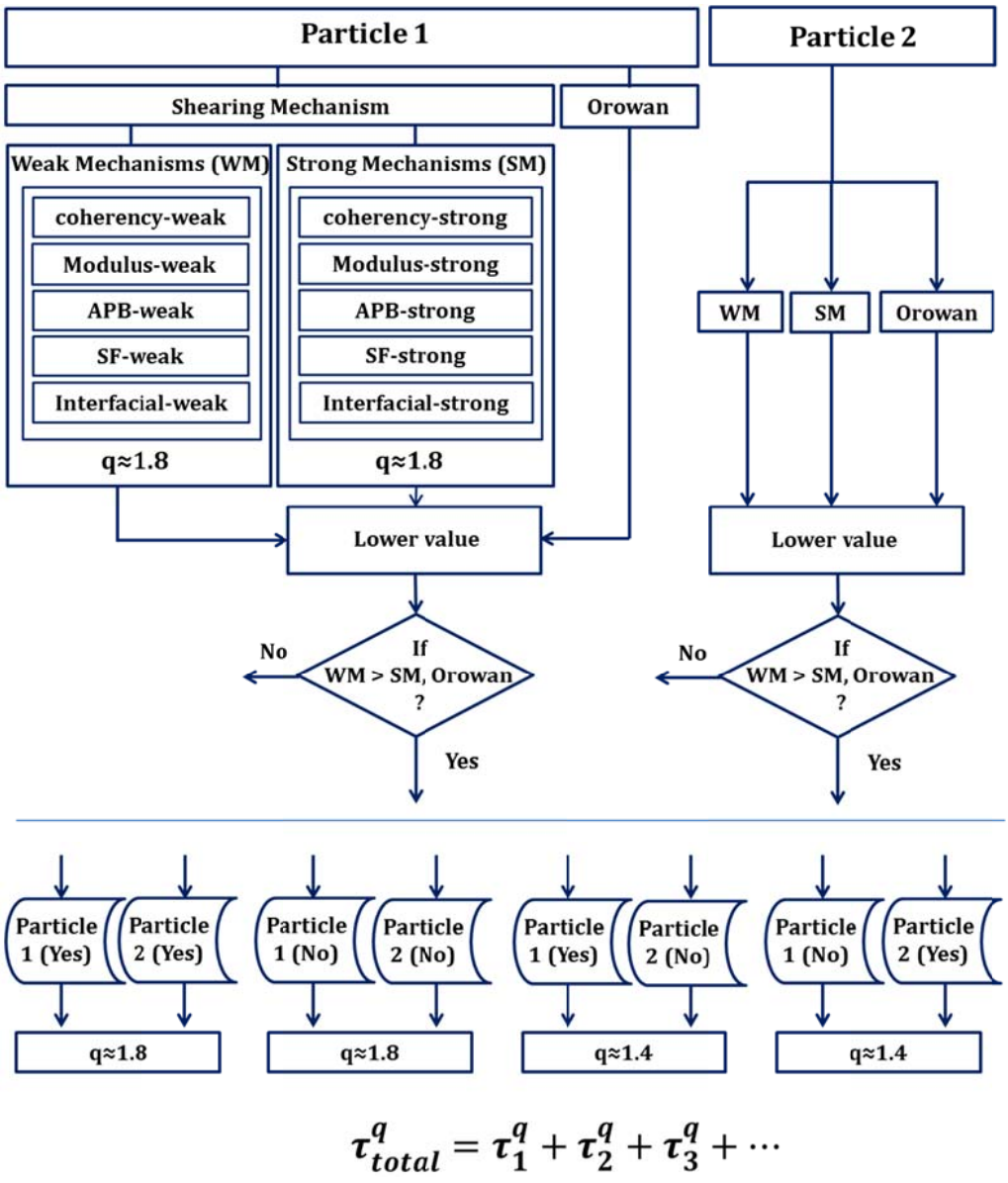

Fig. 6. Combination of different strengthening weak mechanisms (WM) and strong mechanisms (SM) in a single or multi-particle system.

In this figure, the q value for the weak and shearable mechanism and the strong and shearable mechanism is approximately 1.8. The operative strengthening mechanism for a specific precipitate is the one with lower strength among the weak mechanisms (WM), strong mechanisms (SM) and the Orowan mechanism. When there are different particles in the matrix, the mixture law of Ardell [9] should be used. As shown in the flowchart, q is 1.8 when the operative strengthening mechanism in different particles is the WM. In the same way, q is 1.8, when the operative strengthening mechanism in different particles is SM or Orowan. For the combination of WM with SM or Orowan, q is 1.4. In the present study, this procedure is utilized for superposition of all shearable and non-shearable effects including coherency, modulus, APB, stacking fault and interfacial effects.

4 Yield strength prediction in Ni-base alloy 718Plus

The performance of gas turbines and aero-engines can be improved by increasing the operating temperature of these devices. Whereas the Ni-base superalloy Inconel 718 shows superior mechanical properties up to 650°C [48], the alloy Allvac® 718Plus™ (hereafter 718Plus) developed by ATI Allvac in 2004 can be operated at even 55K higher service temperature. For the yield strength modeling, an integrated approach considering all types of contributions to the final yield strength (σ_y) is used, which has been implemented in the solid-state transformation kinetics software MatCalc, version 5.60 (rel 0.005) [49-51].

The composition of 718plus used in this survey is given in table 1.

Table 1: Chemical composition of alloy 718plus.

	Al	Co	Cr	Nb	C	Fe	Mo	Ti	W	Ni
%Wt	1.46	9.13	17.42	5.48	0.028	9.66	2.72	0.71	1.04	balance

A conventional heat treatment process is applied in this work. The specimens are solution annealed at 975°C for 60 minutes, water quenched and aged at 788°C for different aging times (1, 5, 10, 25 and 50 hours).

The final yield strength (σ_y) in this type of annealed crystalline material is constituted by grain boundary strengthening ($\sigma_{y,g}$), solid solution strengthening ($\sigma_{y,s}$) and precipitation strengthening ($\sigma_{y,p}$), which are simply combined linearly [52] as

$$\sigma_y = \sigma_{y,g} + \sigma_{y,s} + \sigma_{y,p} \quad (51)$$

In the following, the models for the individual strengthening contributions to σ_y are briefly reviewed.

4.1 Grain boundary effect

Grain boundaries act as impenetrable barriers for dislocation movement, and contribute, together with the friction stress σ_i, to the yield strength of a crystalline matrix. This concept was formulated by Hall [53] and expanded by Petch [54] as

$$\sigma_{y,g} = \sigma_i + \frac{k_{lock}}{\sqrt{D}}. \quad (52)$$

σ_i is the friction stress of the crystal lattice to dislocation movement, k_{lock} is the locking parameter of grain boundary hardening and D is the grain diameter [40, 54]. Thompson [55] determined the friction stress of Ni-based superalloys as σ_i=21.8 MPa and k_{lock}=0.158 MPa $m^{1/2}$. The measured grain size of 718Plus after quenching is approximately 20 µm. Consequently, the grain size effect produces an increment in final yield strength equal to $\sigma_{y,g}$ =56 MPa

4.2 Solid solution strengthening

The common equation describing the solid solution strengthening effect, as reviewed by Butt [56], is

$$\sigma_{y,s,i} = k_{s,i}\, C_i^p. \quad (53)$$

Here, $k_{s,i}$ is a strengthening constant for solute i, C_i is the concentration of solute i and p is a constant often equal to 1/2 [57, 58]. $\sigma_{y,s,i}$ defines the yield strength increment due to solute i.

For evaluation of the yield strength in multicomponent systems, Gypen and Deruyttere [59] proposed a method to integrate the overall yield strength increment of different alloying components based on the equation,

$$\sigma_{y,s} = \left(\sum_i \left(k_{s,i} C_i^p \right)^q \right)^{\frac{1}{q}} \quad (54)$$

where q=2 and p=1/2. Mishima et al. [60] defined $k_{s,i}$ experimentally for different alloying elements in binary systems Ni-X, with X being an element from the transition metal group. Their results are summarized in table 2.

Table 2 $k_{s,i}$ strengthening constants of different alloying elements in Ni, from ref. [60]

Alloying element	**Al**	**Co**	**Cr**	**Nb**	**C**	**Fe**	**Mo**	**Ti**	**W**
Strengthening constant (MPa At. Fraction$^{-1/2}$)	225	39.4	337	1183	1061	153	1015	775	977

Fig. 7 shows the evolution of the computed solid solution yield strength contributions of individual alloying elements in 718Plus during isothermal aging at 788°C based on the results of the thermo-kinetic precipitation simulation [61].

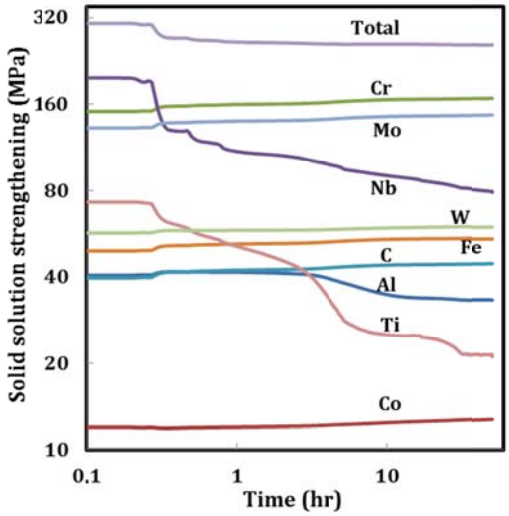

Fig. 7. Computed solid solution yield strength increments of different alloying elements based on the thermo-kinetic precipitation simulation [61].

4.3 Precipitation strengthening

The precipitation strengthening equations in section 2 build upon knowledge of the number density and mean radii of precipitates either from experiment or thermo-kinetic simulation. Accordingly, the yield strength increases roughly proportional to the precipitate mean radius r and number density N_s, and inversely proportional to the precipitate free distance L_s. Consequently, the final yield strength after a specific heat treatment can be evaluated, if the precipitate distribution (number density and radius distribution) and precipitate properties (lattice mismatch, etc.) are known.

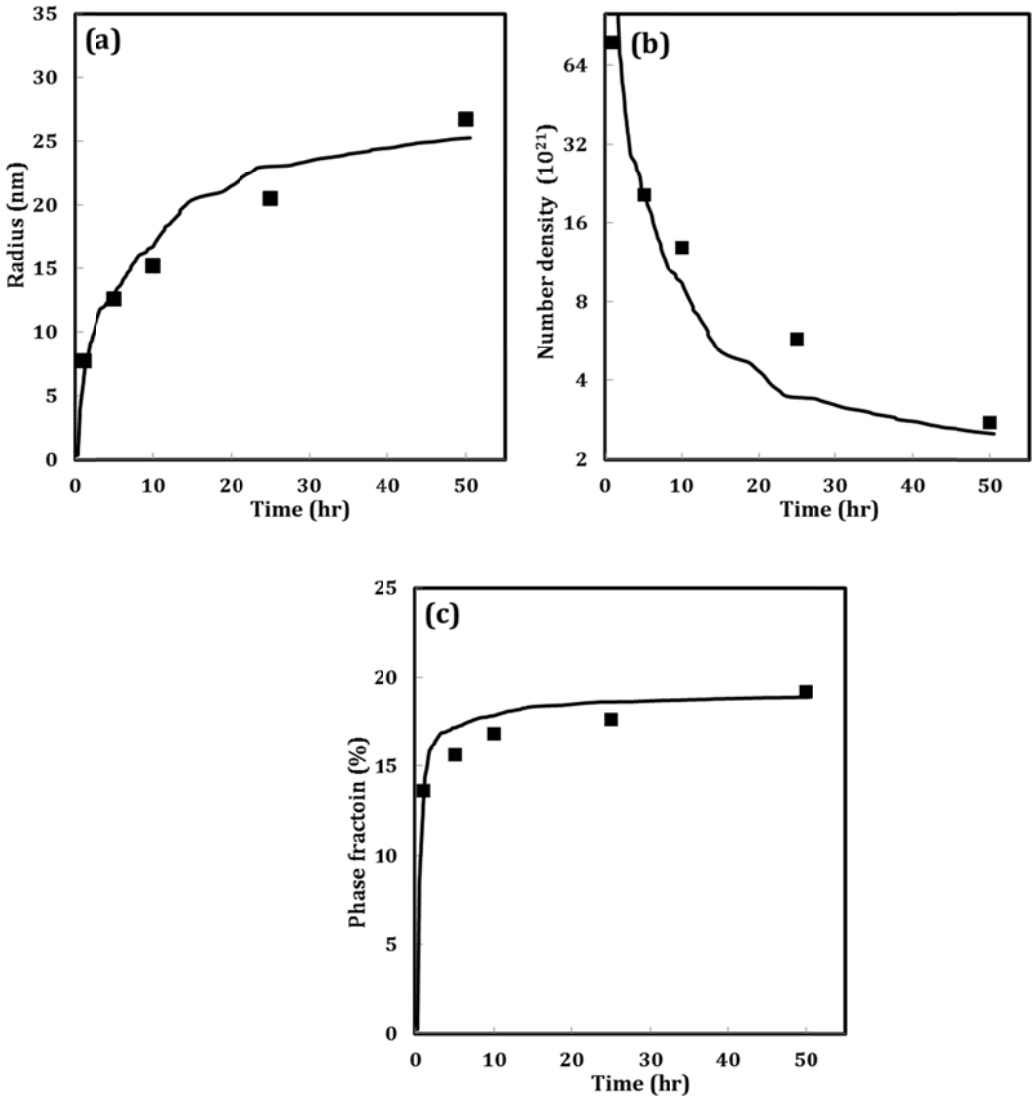

Fig. 8. Simulation result of (a) mean radii (b) number densities and (c) phase fractions of γ' aged at 788°C compared with experimental TEM results (symbols) [61]

Fig. 9 (a) compares the simulated coherency strengthening effect in the weak and strong regimes to predictions based on the Orowan mechanism for γ' precipitates. The lowest strengthening value is assumed to define the operative strengthening mechanism, as outlined in section 3.5. The input parameters of our simulations are summarized in table 3, where the strengthening parameters from the literature as well as parameters obtained from our present microstructural investigation are listed [61, 62].

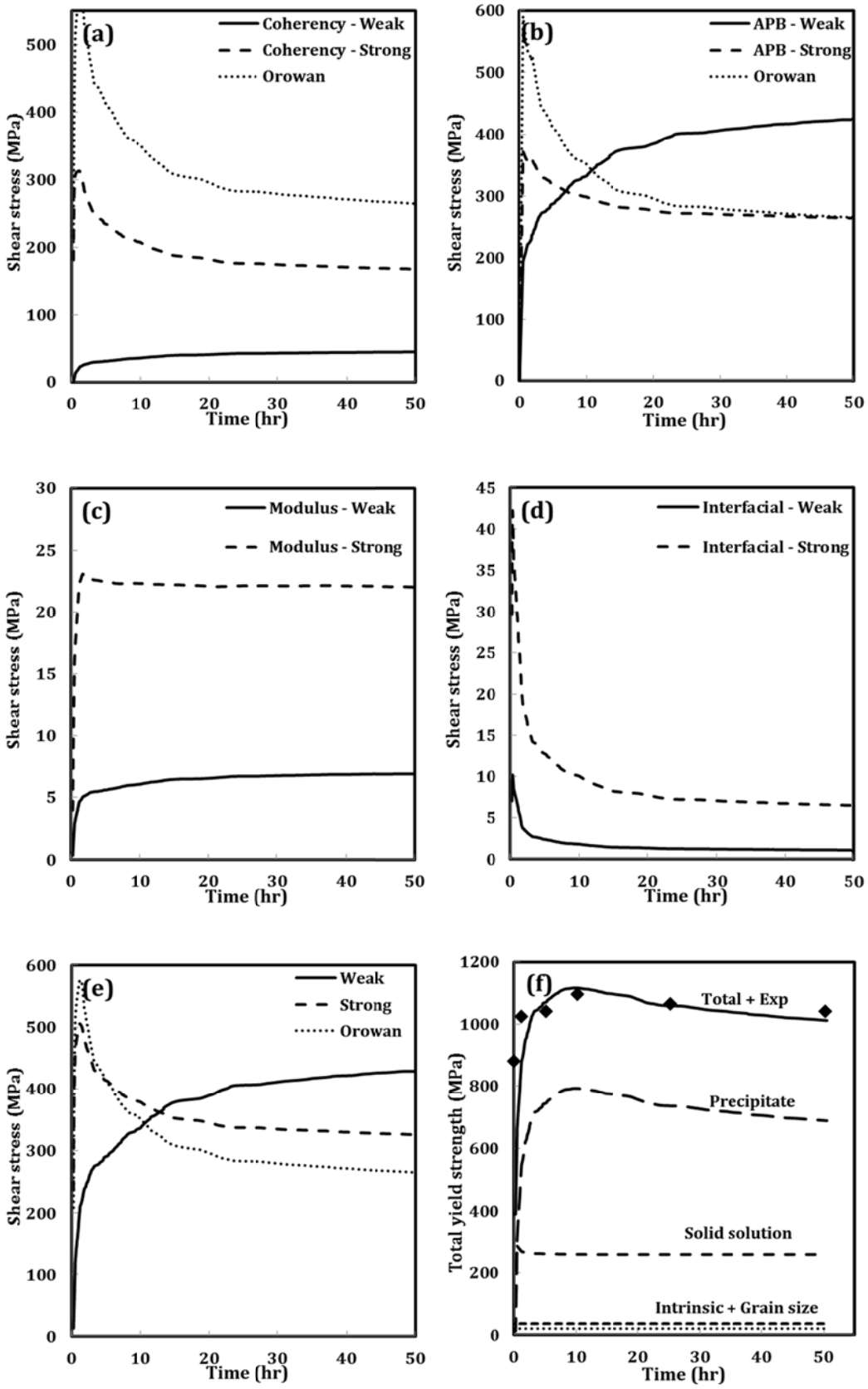

Fig. 9. Simulation result of strengthening in Ni-base superalloy 718plusqaq; (a) coherency effect, (b) APB effect, (c) modulus effect, (d) interfacial effect, (e) combination of all weak and strong

shearing mechanisms and (f) contribution of all strengthening components to σ_y. Results of compression tests are included (symbols) [61].

Table 3: Strengthening parameters used in the precipitation hardening simulation

parameters	values	Comments
***M* (Taylor factor)**	2.6	Ref. [63]
***G* (GPa)**	80.1	Ref. [64]
G_P (GPa)	77.8	Ref. [65]
γ_{APB} (Jm^{-2})	0.111	Ref. [31]
γ_{IF} (Jm^{-2})	0.135-0.16*	MatCalc thermodynamic database
δ	0.004	Measured [61, 62]
***b* (nm)**	0.254	
ν	0.33	
r_i	2b	

*The interfacial energy is composition- and temperature-dependent

Fig. 9 (b) analyzes the computed individual yield strength increment due to the APB effect. This effect is stronger than the coherency effect. Somewhere in the middle of the present heat treatment, the strong mechanism for anti-phase boundary strengthening replaces the weak mechanism. Fig. 9 (c) shows the yield strength increase due to the modulus strengthening effect. Since the shear modulus of γ' precipitates is close to the values of the 718Plus matrix (see table 3), this effect makes up for a value of less than 10 MPa. The chemical effect is even more insignificant than the modulus effect; less than 5 MPa strengthening for the weak mechanism is computed (see Fig. 9 (d)).

Fig. 9 (e) illustrates the simulated contributions of weak and strong regimes obtained from the coherency, APB, modulus and interfacial effects. From the plot, it is evident that the operative strengthening mechanism in 718Plus aged at 788°C is weak and shearable at the early aging hours (before 10 hours aging) and non-shearable at prolonged aging.

The experimental total yield strength values, σ_y, illustrated in Fig. 9 (f) show a maximum at σ_y=1095 MPa after 10 hours. From the simulation results, it can be concluded that, before 10 hours, nucleation and growth of γ' precipitates prevails and, thus, the effect of

radius increment dominates over the effect of number density decrement during coarsening. This is also visible by a rapid increase in the volume fraction evolution, Fig. 8 (c), in the first 10 hours. The approximately constant volume fraction of γ' is located inside the region of coarsening, where a yield strength reduction is observed [61, 62].

Fig. 7 gives a clear indication of the relation between solid solution strengthening and precipitate evolution from nucleation and growth to coarsening. The yield strength due to constitutional alloying elements of γ', such as Nb, Ti and Al decreases at early aging time up to 10 hours. Afterwards, the concentration of each alloying element in the matrix becomes almost constant and, thus, also the solid solution strengthening effect.

Fig. 9 (f) summarizes our computed total yield strength evolution, σ_y, in 718Plus compared with results from compression tests, as well as the simulated contribution of individual strengthening contributions from intrinsic strength and grain size effect, solid solution strengthening and precipitation strengthening during isothermal aging at 788°C. The grain size and intrinsic effects are practically constant because the grain size is unchanged during aging. The predicted decreased solid solution strengthening during aging is by far compensated by the amount of precipitation strengthening, which provides more than 65% of the total yield strength at peak strength [61, 62].

5 Summary

In this thesis, the classical strengthening models for both, shearing and non-shearing, mechanisms are reviewed, discussed and further developed. Where possible, these approaches are modified on basis of recent progress in modeling of essential input parameters for precipitation strengthening with the goal of making the strength predictions more quantitative and accurate.

The proposed equations are established on basis of physical input parameters. These are, among others, dislocation character, precipitate radius, outer cut-off radius and mean free distance between precipitates. Phenomenological parameters are widely avoided, thus increasing accuracy and predictability of the equations.

The free distance between two precipitates decreases when the precipitate shape deviates from spherical. This effect generally increases the yield strength of the material. The increase of the equivalent radius of oblate precipitates in both, shearing and non-shearing mechanisms, increases the final yield strength. In contrast, the decrease of the equivalent radius of prolate

precipitates decreases the final yield strength. This negative effect is partially compensated by the decreasing mean distance between prolate precipitates such that the final yield strength is close to the one of spherical precipitates.

Different methods are discussed for combination of different strengthening mechanisms in complex systems to obtain the final yield strength of multi-phase, multi-particle materials.

Finally, it is demonstrated that the yield strength of the Ni-base superalloy Allvac 718Plus can be accurately predicted over the entire heat treatment cycle. The coupling of yield strength simulation with thermo-kinetic computation of the precipitate evolution shows that precipitation strengthening increases significantly with the volume fraction increase of γ' precipitates. At peak strength, the phase fraction of γ' becomes almost constant. Precipitate coarsening during prolonged aging at 788°C has a negative effect on the final yield strength. The yield strength simulation, which is based on physical modeling and thermo-kinetic precipitation simulation, suggests that, before 10 hours aging, the operative strengthening mechanism in 718Plus is shearing. Afterwards, the strengthening is provided by the non-shearing mechanism.

List of symbols:

a (a_p) Lattice parameter of the matrix (precipitate)

Δa | a - a_p|

b (b_p) Magnitude of Burgers vector in matrix (precipitate)

d_{SF} The length of partial dislocation 2 inside precipitate when P.1 is still in circumference of precipitate

E or $E(\theta)$ Energy of dislocation per unit length in matrix

E_p Energy per unit length of a dislocation in infinite media of precipitate

f phase fraction of precipitate

F Precipitate resistance force

F_m Maximum resistance force of precipitate in different mechanisms

G (G_p) Shear modulus of matrix (precipitate)

h aspect ratio of precipitate

J Correction constant for random arrangement of particles instead of ordered, periodic arrangement (=0.8 or 1)

$K(\theta)$ is elastic energy per unit length between two partial dislocations

L Distance between two particles along dislocation (General definition)

$L_{c,c}$ center to center distance between two particles

L_{eff} Distance between two precipitates along a dislocation at critical configuration of weak and shearable particles

L_s Surface to surface distance between two particles

$L_{s,c}$ Surface to surface distance between two particles in square arrangement of precipitates

$L_{s,s}$ Surface to surface distance between two particles in Sonderegger model [10]

$L_{s,t}$ Surface to surface distance between two particles in a close-packed triangular array

$n_{v,c}$ Number density of particles in each class of precipitates

N_s Number of particles intersecting unit area of slip plane

N_v Number of particles per unit volume of the matrix

P Constant (=0.5)

P_1 The fraction of the edge dislocation

P_2 The fraction of the screw dislocation

q Variable between one and two

r_c Specific radius of precipitates in each class

r_o Outer cut-off distance

r_i Inner cut-off distance

$\bar{r}$ Mean radius of precipitates

r_s Equivalent radius of precipitate in different models.

$r_{s,a}$ Average planar radius in the model of Ardell [9]

$r_{s,b}$ Mean radius of circular section in slip plane in the model of Brown & Ham [8]

$\bar{R}_{eq}(h)$ Equivalent outer cut-off radii in front of moving dislocation in non-shearing mechanism

R The radius of curvature of the dislocation at critical breaking stress

s Number of pair dislocations in the group

T or $T(\theta)$ Dislocation line tension

U_1 Dislocation energy inside the precipitate

U_2 Dislocation energy inside the matrix

V Parameter introduced for remaining dislocation segments and some other uncertainties

W_{eff} is distance between P.1 and P.2 when P.1 is located at precipitate circumference

W_{m} (W_{p}) width of stacking fault in matrix (precipitate)

X Direction of dislocation movement

Y Dislocation line direction

Z Perpendicular direction to the slip plane

z position of the dislocation in the slip plane with respect to the precipitate center

α_1 The angle between dislocation and the normal of the interface in spherical precipitates inside the precipitate

α_2 The angle between dislocation and the normal of the interface in spherical precipitates outside the precipitate

β Constant between 0.0 and 1.0

γ_{APB} Anti-phase boundary energy of precipitate

γ_{IFE} Energy of a matrix-precipitate interface created by dislocation slip

γ_{SFM} (γ_{SFP}) Stacking fault energy of the matrix (precipitate)

Φ Angle through dislocation bending behind two precipitate

δ Fractional lattice misfit between an in situ coherent precipitate and matrix

ε Constrained strain

θ Angle between the dislocation line and its Burgers vector

τ Critical resolve shear stress (external shear stress)

υ (υ_{p}) Poisson's ratio of matrix (precipitate)

Ψ Dislocation bending angle (outer cut-off angle)

Ψ_{c} Critical outer cut-off angle

ω_1 Constant between 0.0175 to 0.0722

ω_2 Constant equal to (=0.81±0.09)

$\overline{\omega}_{\text{eq}}(h)$ Effective equivalent radii in front of moving dislocation in shearing mechanism

References:

[1] A. Wilm, Metallurgie, 8 (1911) 225-227.

[2] P. D. Merica, R. G. Waltenberg, H. Scott, Bull. Am. Inst. Min. Metall. Eng., 150 (1919) 271-316.

[3] P. D. Merica, R. G. Waltenberg, J. R. Freeman, Jr. Trans. Am. Inst. Min. Metall. Eng., LXIV (1921) 3-25.

[4] J. W. Cahn, Alloy Phase Diagr. 4 (1983) 349-351.

[5] N. F. Mott, F. R. N. Nabarro, Proc. Phys. Soc. 52 (1940) 86-89.

[6] E. Orowan, Symposium on Internal Stresses in Metals and Alloys, Session III Discussion, Institute of Metals, London, England, 1948, pp. 451–453.

[7] M.F. Ashby, in: G.S. Ansell, T.D. Cooper, F.V. Lenel (Eds.), Metallurgical Society Conference, vol. 47, Gordon and Breach, New York, 1968, pp. 143–205.

[8] L.M. Brown, R.K. Ham, in: A. Kelly, R.B. Nicholson (Eds.), Elsevier, Amesterdam, The Netherlands, 1971, pp. 9–135.

[9] A.J. Ardell, Metall. Trans. 16A (1985) 2131–2165.

[10] B. Sonderegger, I. Holzer, E. Kozeschnik, Ch. Sommitsch, Comp. Methods Mater. Sci. 11 (2011) 148–153.

[11] M.R. Ahmadi, B. Sonderegger, E. Povoden-Karadeniz, A. Falahati, E. Kozeschnik, Mater. Sci. Eng. A 590 (2014) 262–266.

[12] A. H. Cottrell, prog. Met. Phys. 4 (1953) 205-208.

[13] A. J. E. Foreman, Acta Metall. 3 (1955) 322-330.

[14] J. Friedel, Gauthier-Villars Paris Fr (1956) 205.

[15] V. Gerold, H. Haberkorn. Phys. Stat. Sol. (b) 16 (1966) 675-684.

[16] J. D. Eshelby, Proc. Roy. Soc. A241 (1957) 376.

[17] M.R. Ahmadi, E. Povoden-Karadeniz, K. I. Öksüz, A. Falahati, E. Kozeschnik, Comp. mater. Sci., 91 (2014) 173-186.

[18] M.R. Ahmadi, E. Povoden-Karadeniz, B. Sonderegger, K. I. Öksüz, A. Falahati, E. Kozeschnik, Scr. Mater., 84–85, (2014), 47-50.

[19] R. Siems, P. Delavignette, S. Amelinckx. Phys Status Solidi (b), 2 (1962) 636-660.

[20] G. Knowles, P. M. Kelly. BSC/ISI Conf. Scarb. 1971.

[21] K. C. Russell, L. M. Brown. Acta Metall. 20 (1972) 969-974.

[22] E. Nembach, Phys. Stat. Sol. (a) 78 (1983) 571-581.

[23] E. Nembach, Prog. Mater. Sci. 45 (2000) 275-338.

[24] W. Huther, B. Reppich, Z. Metallkde. 69 (1978) 628-634.

[25] J. S. Hou, J. T. Guo, J. Mater. Eng. Perform. 15 (2006) 67-75.

[26] P. B. Hirsch, A. Kelly, Phil. Mag., 12 (1965) 881-900.

[27] H. Gleiter, E. Hornbogen, Phys. Stat. Sol. (b) 12 (1965) 251-264.

[28] H. Gleiter, E. Hornbogen. Phys. Stat. Sol. (b) 12 (1965) 235-250.

[29] B. Sonderegger, E. Kozeschnik, Scr. Mater. 66 (2012) 52-55.

[30] A. J. Ardell, J.C. Huang, Phil. Mag. Lett. 58 (1988) 189-197.

[31] J. Douin, P. Veyssiere, P. Beauchamp, Phil. Mag. A 41 (1986) 21.

[32] O. R. Myhr, Ø. Grong, S. J. Anderson, Acta mater. 49 (2001) 65–75.

[33] J. F. Nie, B. C. Muddle, Acta Mater. 56 (2008) 3490–3501.

[34] J. F. Nie, B. C. Muddle, J. Phase Equilib. 19 (1998) 543–551.

[35] J. F. Nie, Scr. Mater. 48 (2003) 1009–1015.

[36] A. W. Zhu, E. A. Starke Jr. , Acta Mater. 47 (1999) 3263–3269.

[37] I. N. Khan, M. J. Starink, J. L. Yan, Mater. Sci. Eng. A 472 (2008) 66–74.

[38] G. Liu, G. J. Zhang, X. D. Ding, J. Sun, K. H. Chen, Mater. Sci. Eng. A 344 (2003) 113–124.

[39] M. Song, Mater. Sci. Eng. A 443 (2007) 172–177.

[40] G.E. Dieter, Mechanical Metallurgy, third ed. MaGraw-Hill Book Co, 1986.

[41] A. J. E. Foreman, M. J. Makin, Phil. Mag. 14 (1966) 911-924.

[42] P. M. Kelly, Int. Met. Rev. 18 (1973) 31-36.

[43] R. L. Fullman, Trans. AIME 197 (1953) 1267-1268.

[44] J. C. Huang, A. J. Ardell, Acta Metall. 36 (1988) 2995-3006.

[45] C. Schlieser, E. Nembach, Acta Metall. Mater. 43 (1995) 3983.

[46] T. J. Koppenaal, Appl. Phys. Lett. 4 (1964) 56.

[47] A. J. E. Foreman, M. J. Makin, Can. J. Phys. 45 (1967) 511-517.

[48] O.A. Idowu, O.A. Ojo, M.C. Chaturvedi, Mater. Sci. Eng. A 454–455 (2007) 389–397.

[49] J. Svoboda, F.D. Fischer, P. Fratzl, E. Kozeschnik, Mater. Sci. Eng. A 385 (2004) 166-174.

[50] E. Kozeschnik, J. Svoboda, P. Fratzl, F.D. Fischer, Mater. Sci. Eng. A 385 (2004) 157-165.

[51] E. Kozeschnik, J. Svoboda, F. D. Fischer , CALPHAD, 28 (2005) 379-382.

[52] R. Schnitzer, S. Zinner, H. Leitner, Scr. Mater. 62 (2010) 286–289.

[53]E. O. Hall, Proc. Phys. Soc. lond. B 64 (1951) 747-753.

[54] N. J. Petch, J. Iron Steel Inst. 174 (1953), 25-28.

[55] Anthony A.W. Thompson, Acta Metall. 23 (1975) 1337–1342.

[56] M. Z. Butt, J. Mater. Sci. 28 (1993) 2557-2576.

[57] T. Suzuki, Jpn. J. Appl. Phys. 20 (1981) 449-462.

[58] P. Feltham, Br. J. Appl. Phys. 1 (1968) 303-308.

[59] L.A. Gypen, A. Deruyttere, J. Mater. Sci. 12 (1977) 1028-1038.

[60] Y. Mishima, S. Ochiai, N. Hamao, M. Yodogawa, T. Suzuki, Trans. Jpn. Inst. Met. 27 (1986) 656-664.

[61] M.R. Ahmadi, E. Povoden-Karadeniz, L. Whitmore, M. Stockinger, A. Falahati, E. Kozeschnik, Mater. Sci. Eng. A, 608, (2014) 114-122.

[62] M.R. Ahmadi, L. Whitmore, E. Povoden-Karadeniz, M. Stockinger, A. Falahati, E. Kozeschnik, Adv. Mater. Res. 922 (2014) 7-12.

[63] B. Clausen, T. Lorentzen, T. Leffers, Acta mater. 46 (1998) 3087-3098.

[64] F. J. Garcia-Revillo Sanz, "Optimum design methodology for a test rig turbine disc", School of Engineering (ICAI) Mechanical Engineering, Comillas Pontifical University, Final Thesis, May 2013.

[65] Wang Yun-Jiang, Wang Chong-Yu, Chinese Phys. B 18 (2009) 4339-4348.

List of publications and presentation

Publications

1. **M.R. Ahmadi**, E. Povoden-Karadeniz, K. I. Öksüz, A. Falahati, E. Kozeschnik, *A model for precipitation strengthening in multi-particle systems*, Computational materials Science, Vol. 91, August 2014, Pages 173-186.

2. **M.R. Ahmadi**, B. Sonderegger, E. Povoden-Karadeniz, A. Falahati, E. Kozeschnik, *Precipitate strengthening of non-spherical precipitates extended in ⟨100⟩ or {100} direction in fcc crystals*, Materials Science & Engineering A, Vol. 590 (2014) 262–266.

3. **M.R. Ahmadi**, E. Povoden-Karadeniz, B. Sonderegger, K. I. Öksüz, A. Falahati, E. Kozeschnik, *A model for coherency strengthening of large precipitates*, Scripta Materialia, Vol. 84–85, August (2014) 47-50.

4. **M.R. Ahmadi**, L. Whitmore, E. Povoden-Karadeniz, M. Stockinger, A. Falahati, E. Kozeschnik, *Simulation of yield strength in Allvac® 718Plus™*, Advanced Materials Research Vol. 922 (2014) 7-12.

5. **M.R. Ahmadi**, E. Povoden-Karadeniz, L. Whitmore, M. Stockinger, A. Falahati, E. Kozeschnik, *Yield strength prediction in Ni-base alloy 718Plus based on thermo-kinetic precipitation simulation*, Materials Science & Engineering A, Vol. 608, 1 July 2014, Pages 114-122.

6. Lawrence Whitmore, **Mohammad Reza Ahmadi**, Laure Guetaz, Harald Leitner, Erwin Povoden-Karadeniz, Martin Stockinger, Ernst Kozeschnik, *The microstructure of heat-treated nickel-based superalloy 718Plus*, Materials Science and Engineering A, Vol. 610, (2014), 39-45

7. Lawrence Whitmore, **Mohammad Reza Ahmadi**, Martin Stockinger, Erwin Povoden-Karadeniz, Ernst Kozeschnik, Harald Leitnera, *Microstructural investigation of thermally aged nickel-based superalloy 718Plus*, Materials Science and Engineering A, Vol. 594, 31 January 2014, Pages 253–259.

8. P. Lang, T. Weisz, **M.R. Ahmadi**, E. Povoden-Karadeniz, A. Falahati, E. Kozeschnik: *Thermo-kinetic simulation of the yield strength evolution of AA7075 during natural agin,* Advanced Materials Research Vol. 922 (2014) 406-411.

Publications in Conference Proceedings

1. Ahmad Falahati; **Mohammad Ahmadi**; Peter Lang; Erwin Povoden-Karadeniz; Piotr Warczok; Ernst Kozeschnik; *Thermo-Kinetic Computer Simulation of Precipitation and Age-Hardening Effect in Al-Mg-Si Alloys with Arbitrary Heat Treatment*, Materials Science & Technology, proceeding conference, 2011, Pages 292-299.

2. Peter Lang; Ahmad Falahati, Rene Radis, Erwin Povoden-Karadeniz, **Mohammad Ahmadi**, Piotr Warczok, Ernst Kozeschnik, *Modeling the Influence of Cooling Rate on the Precipitate Evolution in Al-Mg-Si (Cu) Alloys*, Materials Science & Technology, proceeding conference, 2011, Pages 284 – 291.

3. P. Lang, A. Falahati, E. Povoden-Karadeniz, O. Nodin, P. Warczok, **M.R. Ahmadi**, E. Kozeschnik: *Simulation of precipitation sequences of metastable and stable phases in Al-MgSi alloys*: Junior Science Conference (JSC) 2010; P.111-112.

4. P. Lang, A. Falahati, E. Povoden-Karadeniz, **M.R. Ahmadi**, P. Warczok, E. Kozeschnik: *Modeling of the Yield Strength Evolution in Al-Mg-Si Alloys*: 12th International Conference on Aluminium Alloys (ICAA12) 2010; P. 1443-1448.

Conference presentations:

1. **Mohammad Reza Ahmadi**, Erwin Povoden–Karadeniz, Ahmad Falahati, Ernst Kozeschnik, *Precipitation strengthening in multi–phase system*, Institute of Materials Science and Technology, Austria, THERMEC' 2013,December 2-6, 2013, Las Vegas, USA

2. Bernhard Sonderegger, **Mohammad Ahmadi**, Ernst Kozeschnik, Centre for Materials Engineering, *Precipitate strengthening of non–spherical precipitates with arbitrary growth directions* , Department of Mechanical Engineering, University of Cape Town, South Africa, THERMEC' 2013, December 2-6, 2013, Las Vegas, USA

3. Peter Lang, Thomas Weisz, **Mohammad Reza Ahmadi**, Erwin Povoden-Karadeniz, Ahmad Falahati, Ernst Kozeschnik, *Thermo–kinetic simulation of the yield strength evolution of AA7075 during natural aging*, Vienna University of Technology, Austria, THERMEC' 2013, December 2-6, 2013, Las Vegas, USA

4. **M.R. Ahmadi**, A. Falahati, E. Kozeschnik, *Modified equations for precipitation strengthening in Al- Cu alloys taking into account precipitate shape*, Euro LightMAT Conference 2013, 3 - 5 Sept 2013 in Bremen, Germany

Selected original manuscripts

List of selected manuscript

Paper 1

M.R. Ahmadi, E. Povoden-Karadeniz, K. I. Öksüz, A. Falahati, E. Kozeschnik,

A model for precipitation strengthening in multi-particle systems,

Computational Materials Science, Vol. 91, August (2014), 173-186.

Paper 2

M.R. Ahmadi, B. Sonderegger, E. Povoden-Karadeniz, A. Falahati, E. Kozeschnik,

Precipitate strengthening of non-spherical precipitates extended in ⟨100⟩ or {100} direction in fcc crystals,

Materials Science & Engineering A, Vol. 590, 10 January (2014), 262-266.

Paper 3

M.R. Ahmadi, E. Povoden-Karadeniz, B. Sonderegger, K. I. Öksüz, A. Falahati, E. Kozeschnik,

A model for coherency strengthening of large precipitates,

Scripta Materialia, Vol. 84–85, August (2014) 47-50.

Paper 4

M.R. Ahmadi, L. Whitmore, E. Povoden-Karadeniz, M. Stockinger, A. Falahati, E. Kozeschnik,

Simulation of yield strength in Allvac® 718Plus™,

Advanced Materials Research, Vol. 922 (2014) 7-12.

Paper 5

M.R. Ahmadi, E. Povoden-Karadeniz, L. Whitmore, M. Stockinger, A. Falahati, E. Kozeschnik,

Yield strength prediction in Ni-base alloy 718Plus based on thermo-kinetic precipitation simulation,

Materials Science & Engineering A, Vol. 608, 1 July (2014), 114-122.

Paper 1

Computational Materials Science 91 (2014) 173–186

Contents lists available at ScienceDirect

Computational Materials Science

journal homepage: www.elsevier.com/locate/commatsci

A model for precipitation strengthening in multi-particle systems

M.R. Ahmadi [a,b,c,*], E. Povoden-Karadeniz [a], K.I. Öksüz [c], A. Falahati [c], E. Kozeschnik [a,b,c]

[a] Christian Doppler Laboratory for Early Stages of Precipitation, Institute of Materials Science and Technology, Vienna University of Technology, Favoritenstr. 9-11/E308, A-1040 Vienna, Austria
[b] Christian Doppler Laboratory for Early Stages of Precipitation, Department of Physical Metallurgy and Materials Testing, Montanuniversität Leoben, Franz-Josef Straße 18, 8700 Leoben, Austria
[c] Institute of Materials Science and Technology, Vienna University of Technology, Favoritenstr. 9-11/E308, A-1040 Vienna, Austria

ARTICLE INFO

Article history:
Received 20 December 2013
Received in revised form 5 April 2014
Accepted 9 April 2014

Keywords:
Precipitation strengthening
Shearing mechanism
Precipitate resistance force

ABSTRACT

In this work, we present a consistent model describing the increase of yield strength caused by precipitation of second phase particles. Shearing and non-shearing mechanisms are accounted for, depending on the coherency between precipitates and matrix.

The physical key parameters entering the model are critically evaluated on basis of the dislocation line tension, free distance between two particles and precipitate radius. A set of equations is derived, which describes the yield strength increase due to the interaction between dislocations and precipitates. Based on coupling equations for the individual strengthening mechanisms, the model allows for a predictive simulation of the final yield strength caused by precipitation in multi-particle, multi-phase systems. With the aid of contemporary computational power, the enhanced strengthening equations deliver more accurate results compared to the conventional equations.

1. Introduction

Precipitation strengthening (or precipitation hardening) has been discovered more than hundred years ago by Wilm in Al-alloys containing Cu and Mg (Duralumin) [1]. During 1903–1911, Duralumin became one of the most demanded alloys by industry. The first fundamental investigations on the mechanism of precipitation and aging of Duralumin were carried out by Merica et al. [2,3]. By 1932, more than hundred precipitation hardening systems with fourteen base metals were explored by these researchers and reviewed comprehensively by Cahn [4].

The present concept of precipitation hardening is based on the work of Mott and Nabarro [5] proposed in 1940. In their model, Mott and Nabarro investigated the interaction between a single dislocation and the internal stress surrounding a particle, which causes strengthening. In a consistent and comprehensive theory, Orowan [6] first formulated an equation, which describes the interaction between dislocations and non-shearing particles. Later, Ashby [7] modified the Orowan equation to the form, which is currently used most often in calculation of yield strength increase due to precipitation. In 1971, Brown and Ham [8] published a comprehensive critical review, in which they outline some improvement of models for different strengthening mechanisms. Their work was followed up by Ardell in 1985 [9]. This author proposed simplifications of previous physical models, in order to use the strengthening equations more conveniently. For this purpose, phenomenological components in the treatment of phase fractions and assumptions such as, for instance, distribution of particles with the same size, were introduced. Some uncertainty in determination of input parameters remained, however, such as dislocation type (edge or screw) or chemical energies and shear modulus of precipitates.

In the present paper, focus is put on a deeper understanding of the interplay of *physical parameters* in the original models. Additionally, new developments of physical parameters, such as, a recent description of the 2D distance between randomly arranged particles by Sonderegger et al. [10], are incorporated in the yield strength expressions. Finally, a comprehensive set of equations is presented and investigated in a virtual matrix-precipitate strengthening system, which accounts for all studied precipitation strengthening mechanisms simultaneously. In contrast to phenomenological strengthening equations, our approach allows for the prediction of strengthening for non-spherical precipitates, too [11].

* Corresponding author at: Christian Doppler Laboratory for Early Stages of Precipitation, Institute of Materials Science and Technology, Vienna University of Technology, Favoritenstr. 9-11/E308, A-1040 Vienna, Austria. Tel.: +43 1 58801 30885; fax: +43 1 58801 30895.
E-mail address: mohammad.ahmadi@tuwien.ac.at (M.R. Ahmadi).

http://dx.doi.org/10.1016/j.commatsci.2014.04.025
0927-0256/

Nomenclature

List of symbols

a (a_p)	lattice parameter of the matrix (precipitate)
Δa	$\lvert a - a_p \rvert$
b (b_p)	magnitude of Burgers vector in matrix (precipitate)
d_{SF}	the length of partial dislocation 2 (P.2) inside precipitate when P.1 is still in circumference of precipitate
E or $E(\theta)$	energy of dislocation per unit length in matrix
E_p	energy per unit length of a dislocation in infinite media of precipitate
f	phase fraction of precipitate
F	precipitate resistance force
F_m	maximum resistance force of precipitate in different mechanisms
G (G_p)	shear modulus of matrix (precipitate)
J	correction constant for random arrangement of particles instead of ordered, periodic arrangement (=0.8 or 1)
$K(\Theta)$	is elastic energy per unit length between two partial dislocations
L	distance between two particles along dislocation (General definition)
$L_{c,c}$	center to center distance between two particles
L_{eff}	distance between two precipitates along a dislocation at critical configuration of weak and shearable particles
L_s	surface to surface distance between two particles
$L_{s,c}$	surface to surface distance between two particles in square arrangement of precipitates
$L_{s,s}$	surface to surface distance between two particles in Sonderegger model [10]
$L_{s,t}$	surface to surface distance between two particles in a close-packed triangular array
$n_{v,c}$	number density of particles in each class of precipitates
N_s	number of particles intersecting unit area of slip plane
N_v	number of particles per unit volume of the matrix
q	variable between one and two
r_c	specific radius of precipitates in each class
r_o	outer cut-off distance
r_i	inner cut-off distance
$\bar{r}$	mean radius of precipitates
r_s	equivalent radius of precipitate in different models.
$r_{s,a}$	average planar radius in the model of Ardell [9]
$r_{s,b}$	mean radius of circular section in slip plane in the model of Brown and Ham [8]
$\bar{r}_{e,crit,weak}$	the critical radius of precipitate in front of edge dislocation where the shear strength mechanism changes from weak to strong
$\bar{r}_{s,crit,weak}$	the critical radius of precipitate in front of screw dislocation where the shear strength mechanism changes from weak to strong
$\bar{r}_{e,crit,strong}$	the critical radius of precipitate in front of edge dislocation where the shear and strong mechanism changes to Orowan mechanism
$\bar{r}_{s,crit,strong}$	the critical radius of precipitate in front of screw dislocation where the strong shear mechanism changes to Orowan mechanism
R	the radius of curvature of the dislocation at critical breaking stress
R_{APB}	elastic interaction force between two strongly paired dislocations
s	number of pair dislocations in the group
T or $T(\theta)$	dislocation line tension
U_1	dislocation energy inside the precipitate
U_2	dislocation energy inside the matrix
V	parameter introduced for remaining dislocation segments and some other uncertainties
W_{eff}	is distance between P.1 and P.2 when P.1 is located at precipitate circumference
W_m (W_p)	width of stacking fault in matrix (precipitate)
X	direction of dislocation movement
Y	dislocation line direction
Z	distance between slip plane to precipitate center
α_1	the angle between dislocation and the normal of the interface in spherical precipitates inside the precipitate
α_2	the angle between dislocation and the normal of the interface in spherical precipitates outside the precipitate
β	constant between 0.0 and 1.0
γ_{APB}	anti-phase boundary energy of precipitate
γ_{IFE}	energy of a matrix-precipitate interface created by dislocation slip
γ_{SFM} (γ_{SFP})	stacking fault energy of the matrix (precipitate)
Φ	angle through dislocation bending behind two precipitate
δ	fractional lattice misfit between an in situ coherent precipitate and matrix
ε	constrained strain
θ	angle between the dislocation line and its Burgers vector
τ	critical resolve shear stress (external shear stress)
$\upsilon(\upsilon_p)$	Poisson's ratio of matrix (precipitate)
Ψ	dislocation bending angle (outer cut-off angle)
Ψ_c	critical outer cut-off angle
ω_1	constant between 0.0175 and 0.0722
ω_2	constant equal to (=0.81 ± 0.09)

2. The precipitation strengthening model

In this section, the basic concepts behind our strengthening model are formulated in terms of the dislocation line tension and resistance force caused by precipitates. For a quantitative description of the dislocation – particle interaction, energy changes along the dislocation, inside and around the precipitate are the key input quantities.

2.1. Dislocation line tension T

For the evaluation of the dislocation line tension, first, the energy content of a linear dislocation in an isotropic elastic crystal far from the surface and other dislocations is formulated. In this case, the dislocation energy depends on the orientation of the dislocation in the crystal. The dislocation line tension, counted per unit length of dislocation, has been calculated by Cottrell [12] and Foreman [13] as

$$E(\theta) = \frac{Gb^2}{4\pi}\left(\frac{1-\upsilon(\cos\theta)^2}{1-\upsilon}\right)\ln\left(\frac{r_o}{r_i}\right), \quad (1)$$

where G is the shear modulus, θ is the angle between the dislocation line and its Burgers vector, b is the magnitude of the Burgers vector, υ is Poisson's ratio, and r_o is the outer cut-off distance. r_o is the distance to the closest parallel dislocation of opposite sign, which is the distance between two particles along the dislocation line for shearable precipitates [8,9] and the average planar particle diameter for non-shearable precipitates [7,9]. r_i is the inner cut-off

distance, which is the dislocation core radius with values between b and $4b$ [9]. The energy of the dislocation, $E(\theta)$, is a function of the angle θ between the Burgers vector and the tangent to the dislocation line. Since $\theta = 0$ for screw dislocations and $\theta = \pi/2$ for edge dislocations, the character of a dislocation determines its energy. Eq. (1) shows that an edge dislocation stores more energy compared to a screw dislocation.

When an anisotropic strain field exists around a dislocation, we must consider also the dislocation core energy and modify Eq. (1) depending on the dislocation character and the matrix [14,15]. Clouet et al. [16] determined the dislocation core energy of screw dislocations in bcc iron with an amount of 14% of the total dislocation energy. In the present development of strengthening equations, we consider the dislocation line energy in an isotropic elastic crystal and neglect the dislocation core energy.

We distinguish between the dislocation energy and the line tension, $T(\theta)$, which also depends on θ, according to the relation given by Brown and Ham [8] as

$$T(\theta) = E(\theta) + \frac{d^2E(\theta)}{d\theta^2}, \tag{2}$$

and, finally,

$$T(\theta) = \frac{Gb^2}{4\pi}\left(\frac{1+\upsilon-3\upsilon(\sin\theta)^2}{1-\upsilon}\right)\ln\left(\frac{r_o}{r_i}\right). \tag{3}$$

In the following treatment, we use the symbol T for $T(\theta)$ and omit explicitly writing the angle dependence for the sake of brevity.

2.2. Interaction between dislocations and precipitates

The process of bowing out of a dislocation between spherical precipitates as a consequence of an external shear force is described by the equilibrium between the line tension T of the dislocation, the dislocation bending angle (outer cut-off angle) Ψ and the critical resolved shear stress τ with the precipitate resistance force F. According to [8], this equilibrium, which is shown in Fig. 1, is expressed as

$$\tau bL = 2T\cos\frac{\Psi}{2} = F. \tag{4}$$

In this equation, τ is the external shear stress and L is the distance between two particles along the dislocation.

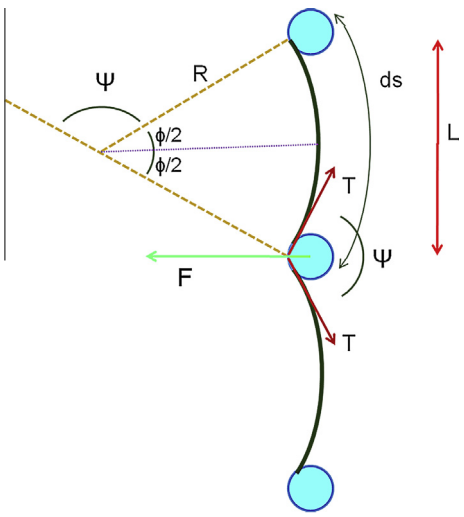

Fig. 1. Balance force between a precipitate and a dislocation.

2.3. Shearing mechanisms

When dislocations enter and shear (cut) a spherical precipitate, the maximum resistance force exerted by the precipitate is proportional to the projection of the dislocation line tension in the direction of movemen $F_m = 2T\cos(\Psi_c/2)$, as depicted in Fig. 1. If the critical outer cut-off angle is between $120° \leqslant \Psi_c \leqslant 180°$, a particle is denoted as *weak* and shearable. Between $0° \leqslant \Psi_c \leqslant 120°$, the particle is considered as *strong* and shearable. The angle Ψ_c strongly depends on the size of the particle and dislocation character.

For weak and shearable particles, it is assumed that $\phi_c = \sin\phi_c = ds/R$ where R is the radius of the dislocation curvature at the critical breaking stress. Accordingly, Eq. (4) is simplified (see Fig. 1) as

$$\tau = \frac{2T}{bL_{eff}}\cos\frac{\Psi_c}{2}. \tag{5}$$

In this equation, L_{eff} is the distance between two precipitates along the dislocation in the critical configuration for weak and shearable particles. L_{eff} is different from the surface to surface distance between two particles L_s, because, for weak and shearable precipitates, dislocations cut the precipitates when the outer cut-off angle is between $120° \leqslant \Psi_c \leqslant 180°$ and are released from the particle sooner. Consequently, the distance between two precipitates is increased along the dislocation, and $L_{eff} > L_s$. This effect is shown schematically in Fig. 2.

The relation between L_s and L_{eff} has been evaluated by Friedel [17] between too small particles with

$$L_s = L_{eff}\left[\cos\frac{\Psi_c}{2}\right]^{\frac{1}{2}}. \tag{6}$$

Using Eqs. (4)–(6), one obtains

$$\tau = \frac{2T}{bL_s}\left[\frac{F_m}{2T}\right]^{\frac{3}{2}}. \tag{7}$$

Eq. (7) represents a general relation, which is used to express the shear stress according to different strengthening mechanisms for weak and shearable precipitates. Eq. (4) is applicable for strong and shearable precipitates if we assume $L = L_s$ at the critical value when $\Psi = \Psi_c$ (see Fig. 2(A)) as

$$\tau = J\frac{2T[\cos(\Psi_c/2)]}{bL_s} = J\frac{F_m}{bL_s}. \tag{8}$$

F_m corresponds to the maximum resistance force of precipitates that can be achieved and it is formulated for different strengthening mechanisms contributing to shearing, subsequently.

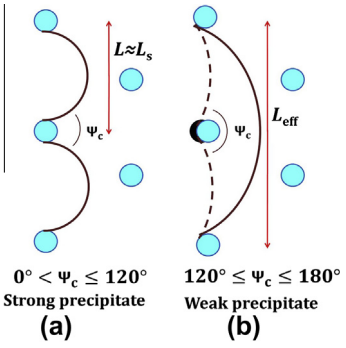

Fig. 2. Free distance between two precipitates along dislocation line in a random array. (A) The precipitates are shearable and strong and (B) the precipitates are shearable and weak.

In this equation, the parameter J is a correction coefficient, which depends on the mean free distance between particles. A value of $J = 0.8$ is used, based on the Ashby model [7] for random arrangement of particles instead of particles in an ordered, periodic arrangement. Using the Sonderegger model [10], the free distance L_s between two particles can alternatively be calculated from Eqs. (49) and (50), later. A constant value of $J = 1$ is then used.

2.3.1. Coherency effect

If a precipitate is embedded coherently in some given matrix phase, the difference between lattice parameters of matrix and precipitate produces a strain field, which potentially interacts with a moving dislocation. Depending on the magnitude of misfit, this mechanism often provides the most important strengthening contribution for coherent particles.

2.3.1.1. Weak and shearable precipitates. Gerold and Haberkorn [18] proposed a strengthening model for weak and shearable precipitates based on isotropic elasticity theory. Accordingly, the force F between a straight dislocation and a spherical coherent precipitate on a slip plane is

$$F\left(\frac{z}{\bar{r}}\right) = 4Gb\varepsilon\bar{r}\chi\left(\frac{z}{\bar{r}}\right), \tag{9}$$

With

$$\varepsilon = \frac{1}{3}\left(\frac{1+\upsilon}{1-\upsilon}\right)\frac{\Delta a}{a} \approx \frac{2}{3}|\delta|. \tag{10}$$

Here, ε is the constrained strain produced by the stress free strain of lattice misfit δ [19], a is the lattice parameter of the matrix, $\bar{r}$ is the mean radius of precipitates and Δa is the difference between lattice parameters of matrix and precipitate. $\chi(z/\bar{r})$ is a function depending on the interaction between the dislocation in the slip plane and the precipitate. z denotes the distance between the slip plane and the precipitate center. If the slip plane is located in the center of the precipitate, $z = 0$ and the strain field produced by the upper side of the slip plane is compensated by the lower part. Consequently, the stress force is balanced on the dislocation from two sides ($F = 0$). If the slip plane cuts the precipitate away from its center, the $\chi(z/\bar{r})$ function increases and reaches a maximum at $\chi\left(\sqrt{2}/2\right) = 1$, for edge and at $\chi(1) = 1/2$ for screw dislocations. The values of the $\chi(z/\bar{r})$ function can be expressed by the following functions for an edge dislocation,

$$\chi\left(\frac{z}{\bar{r}}\right) = 2\left(\frac{z}{\bar{r}}\right)\sqrt{1-\left(\frac{z}{\bar{r}}\right)^2} \quad \text{if} \quad \left(\frac{z}{\bar{r}}\right)^2 \le \frac{3}{4}, \tag{11}$$

$$\chi\left(\frac{z}{\bar{r}}\right) = \frac{3\sqrt{3}}{8\left(\frac{z}{\bar{r}}\right)^2} \quad \text{if} \quad \left(\frac{z}{\bar{r}}\right)^2 \ge \frac{3}{4}, \tag{12}$$

and for a screw dislocation,

$$\chi\left(\frac{z}{\bar{r}}\right) = \frac{1}{2}\left(\frac{z}{\bar{r}}\right) \quad \text{if} \quad \left(\frac{z}{\bar{r}}\right) \le 1, \tag{13}$$

$$\chi\left(\frac{z}{\bar{r}}\right) = \frac{1}{2\left(\frac{z}{\bar{r}}\right)^2} \quad \text{if} \quad \left(\frac{z}{\bar{r}}\right) \ge 1. \tag{14}$$

In consideration of the coherency mechanism, the resistance force in front of the moving dislocation increases when the dislocation stays out of the precipitate center defined in Eqs. (11) and (13). The resistance force decreases smoothly at $(z/\bar{r}) > 1$ although there is no interaction between precipitate and dislocation in the slip plane as explained by Eqs. (12) and (14).

By applying the Pythagorean mixture law as proposed by Brown and Ham [8], and combining Eqs. (7) and (9), strengthening due to the coherency misfit mechanism for weak and shearable precipitates from center of the precipitate up to infinity can finally be expressed as

$$\tau_{Coh,weak}^2 = \frac{1}{b^2 L_s^2 2T}\int_0^\infty F^3\left(\frac{z}{\bar{r}}\right)\frac{dz}{\bar{r}}. \tag{15}$$

For an edge dislocation,

$$\tau_{Coh,weak} = \left(\frac{592}{35}\frac{G^3 b\varepsilon^3(\bar{r})^3}{L_s^2 T(\pi/2)}\right)^{\frac{1}{2}}, \tag{16}$$

and for a screw dislocation,

$$\tau_{Coh,weak} = \left(\frac{9}{5}\frac{G^3 b\varepsilon^3(\bar{r})^3}{L_s^2 T(0)}\right)^{\frac{1}{2}}. \tag{17}$$

2.3.1.2. Strong and shearable precipitates. Eq. (15) is used to describe the effect of coherency strain when the size of the precipitates is small or the outer cut-off angle is higher than 120°. In the case of large precipitates, which can bend dislocations to angles below 120°, the Friedel relation, Eq. (6), is no longer valid for Eqs. (15)–(17). The concept of strong precipitates is also dependent on the position of the dislocation in the slip plane with respect to the precipitate (Z value). For example, at $Z = 0$, a large precipitate acts as weak and shearable. When the Z parameter is confined between $(T/(4G\varepsilon b)) \le Z \le \left(3^{1.5}G\varepsilon b(\bar{r})^3/(4T)\right)^{0.5}$ for edge dislocations, and $(T/(G\varepsilon b)) \le Z \le \left(G\varepsilon b(\bar{r})^3/(T)\right)^{0.5}$ for screw dislocations, precipitates have the capability of producing the bending condition corresponding to a strong precipitate. Precipitation strengthening can then be expressed by the following equation for an edge dislocation when it is assumed that the free distance between two particles is close to the non-shearable condition ($L \approx L_s$) [8,20] with

$$\tau_{Coh,strong} = 2^{\frac{1}{2}}3^{\frac{3}{8}}\frac{J}{L_s}\left(\frac{T^3(\pi/2)G\varepsilon\bar{r}}{b^3}\right)^{\frac{1}{4}}, \tag{18}$$

and for a screw dislocation,

$$\tau_{Coh,strong} = 2\frac{J}{L_s}\left(\frac{T^3(0)G\varepsilon\bar{r}}{b^3}\right)^{\frac{1}{4}}. \tag{19}$$

2.3.2. Modulus effect

When a dislocation passes through a precipitate, the dislocation energies inside and outside the precipitate are different due to different chemical composition and/or crystal structure of precipitate and matrix. In 1962, Siems et al. [21] used Snell's Law to explain this mechanism based on the condition

$$U_1 \sin\alpha_1 = U_2 \sin\alpha_2. \tag{20}$$

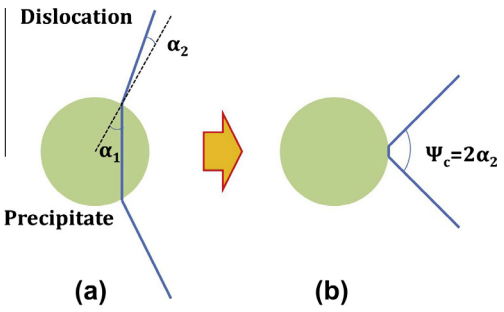

Fig. 3. Dislocation treatment inside precipitate, when the Young's modulus of the precipitate is lower than the Young's modulus of the matrix.

In this equation, U_1 and U_2 are the dislocation energy inside the precipitate and the matrix, respectively. α_1 and α_2 represent the angles between the dislocation and the normal of the precipitate/matrix interface. This is shown schematically in Fig. 3.

In the Siems et al. model [21], the dislocation energy inside the precipitate is assumed to be lower than that in the matrix ($U_1 < U_2$). In this case, at the final stage of shearing, when the dislocation wants to escape the precipitate, the breaking angle $2\alpha_2$ is equal to Ψ_c and $\alpha_1 = 90°$ (compare with Fig. 3(B)). Then,

$$\Psi_c = 2\alpha_2 = 2\sin^{-1}\left(\frac{U_1}{U_2}\right). \tag{21}$$

Similar to the case of coherency strengthening, the outer cut-off angle Ψ_c can be in the range of the weak and shearable or strong and shearable condition, which is discussed in Section 2.3. Substituting Eq. (21) into Eqs. (5) and (6) for the weak and shearable conditions, one arrives at [20]

$$\tau_{Mod,weak} = \frac{2T}{bL_s}\left[1 - \left(\frac{U_1^2}{U_2^2}\right)\right]^{\frac{3}{4}}. \tag{22}$$

Replacing Ψ_c in Eq. (8) by Eq. (21) for strong and shearable precipitates, under the assumption that the free distance between two particles is close to non-shearable condition ($L \approx L_s$) [20], delivers

$$\tau_{Mod,strong} = J\frac{2T}{bL_s}\left[1 - \left(\frac{U_1^2}{U_2^2}\right)\right]^{\frac{1}{2}}. \tag{23}$$

In order to specify the values of U_1 and U_2 in Eqs. (22) and (23), the dislocation energy inside the precipitate must be related to the precipitate radius and energy per unit length of a dislocation in infinite media of precipitate and matrix. This was done on a numerical basis by Knowles and Kelly [22], leading to

$$\frac{U_1}{U_2} = \frac{E_p \log\frac{r_s}{r_i}}{E\log\frac{r_o}{r_i}} + \frac{\log\frac{r_o}{r_s}}{\log\frac{r_o}{r_i}}. \tag{24}$$

In this equation, r_o is the outer cut-off distance, r_i is the inner cut-off distance [23] and r_s is the equivalent precipitate radius defined in different models. This will be further discussed later. E_p is the energy of a dislocation per unit length in infinite media of precipitate. For a screw dislocation, E_p/E is equal to G_p/G (shear modulus of precipitate and matrix) and for an edge dislocation, the ratio reads

$$\frac{E_p}{E} = \frac{G_p(1-\upsilon)}{G(1-\upsilon_p)}, \tag{25}$$

where υ_p is the Poisson's ratio of the precipitate.

In 1983, Nembach [24] considered modulus strengthening numerically by evaluating the interaction force between a dislocation and a spherical precipitate with different shear modulus from the matrix. In this model, the maximum interaction force becomes

$$F_m = \omega_1|G_p - G|b^2\left(\frac{r_s}{b}\right)^{\omega_2}. \tag{26}$$

where ω_1 and ω_2 are constants representing the dislocation core energy inside and outside the precipitate. Depending on the models used in [24], ω_1 varies between 0.0175 and 0.0722. ω_2 adopts a value of 0.81 ± 0.09. By replacing the force in Eq. (7) with F_m in Eq. (26), the shear stress according to the weak modulus mechanism becomes

$$\tau_{Mod,weak} = \frac{2T}{bL_s}\left[\frac{\omega_1|G_p - G|b^2(r_s/b)^{\omega_2}}{2T}\right]^{\frac{3}{2}}, \tag{27}$$

and replacing F_m in Eq. (8) by Eq. (26) delivers the equivalent expression for the strong mechanism as

$$\tau_{Mod,strong} = J\frac{\omega_1|G_p - G|b^2(r_s/b)^{\omega_2}}{bL_s}. \tag{28}$$

In these formulations, the absolute value of the difference in shear modules between precipitate and matrix enters the equation. Consequently, this model applies to both situations where the modulus of the precipitate is larger or smaller as well.

2.3.3. Anti-phase boundary effect

Dislocations entering a particle lead to breaking of chemical bonds. The rearrangement of chemical bonds into different local chemical environment leads to strengthening. Generally, this effect is denoted as *chemical strengthening*. It is commonly distinguished between anti-phase boundary, stacking fault and interfacial effects.

If particles in a matrix show chemical ordering, the anti-phase boundary effect often represents the major strengthening mechanism. When a dislocation passes through an ordered precipitate, it destroys the periodic atomic arrangement in its slip plane. The disordered plane, which is left behind, is called anti-phase boundary (APB).

In ordered crystal structures, the shearing dislocations travel in groups, where the number of dislocations in a group depends on the type of order structure (e.g. face-centered cubic $L1_2$, tetragonal $D0_{22}$). This observation is important for the interpretation of the ability of precipitates to restore to the perfect order structure after the precipitate-dislocation interaction. The first dislocation, which is denoted as leading dislocation, creates an anti-phase boundary in the precipitate. The second one, which is called trailing dislocation, compensates the effect of the first one and restores the ordered structure again. Depending on the size of the precipitate, we again distinguish two regimes.

2.3.3.1. Weak and shearable precipitates. This regime is operative if the precipitates are small, i.e. the outer cut-off angle is $\Psi_c > 120°$. The disordered precipitates stimulate the trailing dislocations towards the leading dislocation. This compensates, partly, the APB strengthening effect of the leading dislocation (see Fig. 4(A)). The strengthening equation for the APB effect can be expressed by using Eq. (7) with $F_m = 2\gamma_{APB}\, r_s$ as

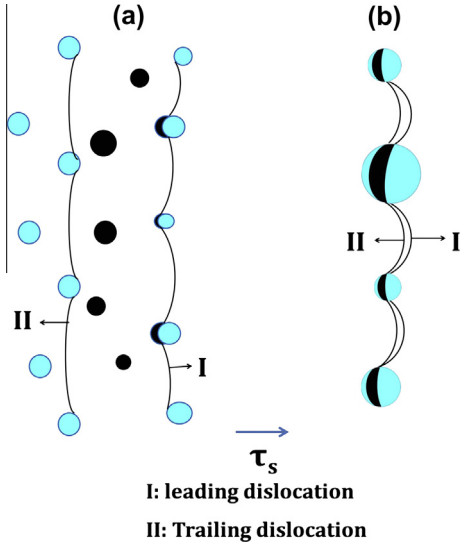

Fig. 4. Schematic illustration of ordered coherent precipitates affected by a pair of dislocations. Precipitate regions, which are affected by dislocation and suffer the APB effect, are shown in black. (A) Coherent and weak precipitates and (B) coherent and strong precipitates.

$$\tau_{APB,weak} = \frac{2}{s}\left\{\frac{2T}{bL_s}\left[\frac{2\gamma_{APB}r_s}{2T}\right]^{\frac{3}{2}} - \beta\zeta\left(\frac{r_s}{L_s}\right)\right\}. \quad (29)$$

where γ_{APB} is the anti-phase boundary energy of the precipitate and β is a constant between 0.0 and 1.0. β is close to 1.0 when the trailing dislocation is straight. s is the number of pair dislocations in the group and the function $\zeta(r_s/L_s)$ corresponds to the pulling tension of precipitates on the trailing dislocation. It is given as [25]

$$\zeta\left(\frac{r_s}{L_s}\right) = \frac{16}{3\pi}\frac{\gamma_{APB}r_s^2}{bL_s^2}. \quad (30)$$

2.3.3.2. Strong and shearable precipitates. When the precipitates are large, application of Eq. (29) becomes critical because the precipitates produce a high APB force (see Fig. 4(B)). In this situation, when the leading dislocation travels through the precipitate, the resistance force of the precipitate, F_1, increases with the distance x in the direction of dislocation movement (see Fig. 5). Consequently, the dislocation tries to increase its line tension force by decreasing the outer cut-off angle. For small precipitates, this mechanism could be energetically favorable for the dislocation, and it can pass through the precipitate. But for larger precipitates, the line tension force of the dislocation cannot compensate the high APB force of the precipitate and the dislocation becomes stuck inside the precipitate in position $x_1 = x_m$ and F_1 arrives to the maximum $F_m = F_1 = -\gamma_{APB}\, d(x_1)$.

Analogous to the weak and shearable treatment of structural reordering, the trailing dislocation is attracted by the precipitate. This has two effects on the leading dislocation. Firstly, it reconstructs the ordered structure of the precipitate, which produces a force with opposite sign of F_1 on the leading dislocation, which is $F_2 = +\gamma_{APB}\, d(x_2)$. This stimulates the leading dislocation to go forward. Secondly, it generates a repulsive force due to the elastic interaction between dislocations. Gleiter and Hornbogen [26] have described the elastic interaction force between two strongly paired dislocations as

$$R_{APB} = V\frac{Gb^2}{2\pi}\frac{d(x_m)}{x_m}, \quad (31)$$

where R_{APB} is the elastic interaction force between two strongly paired dislocations. V is a parameter introduced for remaining dislocation segments incorporating also some other uncertainties. Its value is assumed to be 2.8 in Ref. [27]. F_2 and R_{APB} drive the leading dislocation to move and shear the precipitate. In this regime, the maximum shear stress occurs when $F_m = F_1$ and $F_2 = 0$.

Finally, Hüther and Reppich [28] obtained a general expression for strong and shearable ordered particles as

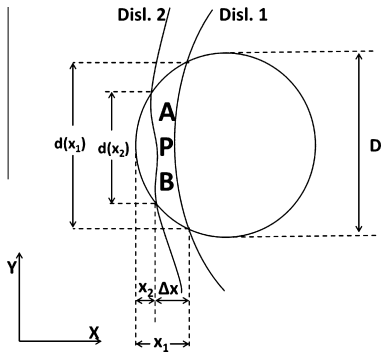

Fig. 5. Interaction between leading and trailing dislocations with a precipitate where the area between dislocations is a disordered region (APB).

$$\tau_{APB,strong} = \left(\frac{2VT}{\pi bL_s}\right)\left(\frac{\pi\gamma_{APB}r_s}{VT} - 1\right)^{\frac{1}{2}}. \quad (32)$$

2.3.4. Stacking fault effect

In some crystalline materials, the dislocation energy of a single dislocation can be reduced by dissociation into two partial dislocations. This process leads to a stacking fault (SF) in the slip plane between the partial dislocations 1 (P.1) and 2 (P.2). When the stacking fault energy (SFE) of the precipitate is lower than that of the matrix, the width of the ribbon band between two partials inside and outside of the precipitate differs. This difference produces a retarding force in front of the dislocation movement, which depends on the precipitate size and the width of the stacking fault in the matrix W_m and inside the precipitate W_p. In Fig. 6, W_m and W_p are displayed for the cases where the dislocation is free from external tension (left side) and where the dislocation is under external tension (right side). In Fig. 6a, the precipitate is located between P.1 and P.2 in tension-free condition, where W_m and W_p are wider than the equivalent precipitate diameter ($2r_s$). In

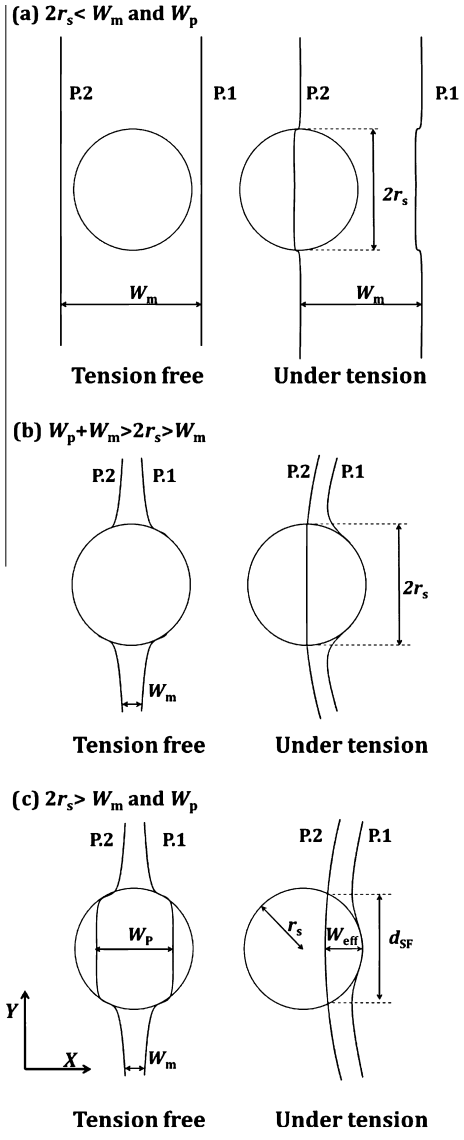

Fig. 6. Distance between two partial dislocation inside and outside a precipitate for the cases where the dislocation is free or under external tension. (a) Equivalent precipitate diameter ($2r_s$) is smaller than the width of the stacking fault in matrix W_m and in precipitate W_p, (b) $W_p + W_m > 2r_s > W_m$ and (c) $2r_s > W_m$ and W_p.

tension-free condition of Fig. 6b, P.1 and P.2 touch two sides of precipitate where $2r_s$ is smaller than $W_p + W_m$ and larger than W_m.

By applying external tension on dislocations, in both cases defined in Fig. 6a and b, the precipitate resistance force increases due to the P.2 displacement and reaches its maximum at the precipitate center (right side of Fig. 6a and b). The maximum resistance force for these two conditions is,

$$F_m = 2r_s(\gamma_{SFM} - \gamma_{SFP}), \tag{33}$$

where $(\gamma_{SFM} - \gamma_{SFP})$ is the difference between the stacking fault energies of the matrix and the precipitate. Replacing Eqs. (7) and (8) by Eq. (33) delivers the stacking fault strengthening for weak and strong precipitates with

$$\tau_{SF,weak} = \frac{2T}{bL_s}\left[\frac{r_s(\gamma_{SFM} - \gamma_{SFP})}{T}\right]^{\frac{3}{2}}, \tag{34}$$

and,

$$\tau_{SF,strong} = J\frac{2r_s(\gamma_{SFM} - \gamma_{SFP})}{bL_s}. \tag{35}$$

Fig. 6c depicts the interaction between precipitate and partial dislocations, when $2r_s$ is larger than W_p and W_m. The length of partial dislocation 2 inside the precipitate (d_{SF}) defines the maximum precipitate resistance force when P.1 is still located along the circumference of the precipitate. Hirsch and Kelley [29] derived the maximum force as

$$F_m = 2(\gamma_{SFM} - \gamma_{SFP})\left(W_{eff}r_s - \frac{W_{eff}^2}{4}\right)^{\frac{1}{2}}, \tag{36}$$

$$W_{eff} = \frac{2K(\theta)}{(\gamma_{SFM} + \gamma_{SFP})}, \tag{37}$$

$$K(\theta) = \frac{Gb_p^2(2-\upsilon)}{8\pi(1-\upsilon)}\left(1 - \frac{2\upsilon\cos(2\theta)}{(2-\upsilon)}\right), \tag{38}$$

W_{eff} is the distance between P.1 and P.2, when P.1 is located at the precipitate circumference, $K(\Theta)$ is the elastic energy per unit length between two partial dislocations and b_p is the magnitude of the Burgers vector in the precipitate. If we replace F_m in Eq. (7) by Eq. (36), we finally obtain the yield stress increment for the weak mechanism as

$$\tau_{SF,weak} = \frac{2T}{bL_s}\left[\frac{(\gamma_{SFM} - \gamma_{SFP})\left(W_{eff}r_s - W_{eff}^2/4\right)^{\frac{1}{2}}}{T}\right]^{\frac{3}{2}}. \tag{39}$$

Replacing Eq. (8) by Eq. (36), the expression for the strong regime is found as

$$\tau_{SF,strong} = J\frac{2(\gamma_{SFM} - \gamma_{SFP})\left(W_{eff}r_s - W_{eff}^2/4\right)^{\frac{1}{2}}}{bL_s}. \tag{40}$$

2.3.5. Interfacial effect

When a dislocation cuts a coherent precipitate, two new ledges forms. One is created after entering the precipitate, the other one after leaving it. These ledges cause an increment in the interfacial area in these regions. The maximum force related to this mechanism is expressed by $F_m = 2\ \gamma_{IFE}\ b$ [9], where γ_{IFE} is the energy of the precipitate-matrix interface created by dislocation slip. Replacing F_m in Eq. (7) delivers

$$\tau_{Chem,weak} = \frac{2T}{bL_s}\left[\frac{\gamma_{IFE}b}{T}\right]^{\frac{3}{2}}. \tag{41}$$

for the weak and shearable mechanism and if the operative strengthening regime is strong and shearable, we replace F_m in Eq. (8) and arrive at

$$\tau_{Chem,strong} = J\frac{2\gamma_{IFE}b}{bL_s}. \tag{42}$$

2.4. Non-shearing mechanism

Ashby [7] suggested a widely used expression for the ultimate shear stress related to non-shearable precipitates. He introduced simplifying assumptions for the outer cut-off distance of the precipitate into the original Orowan equation and, furthermore, made assumptions on the dislocation character. Ashby considered the exact shape of the dislocation when a dislocation approaches a Frank-Read configuration between two precipitates. In this situation, which is shown in Fig. 1, the dislocation escapes the precipitate as soon as the outer cut-off angle reaches an angle of $\Psi = 0$. Then,

$$\tau_{Orowan} = J\frac{2E(\pi/2 - \theta)}{bL_s}. \tag{43}$$

Fig. 7 illustrates the interaction between an edge dislocation ($\theta = \pi/2$) with an array of strong precipitates in the dislocation slip plane. In step 1, the external tension is assumed to be zero and the dislocation is located straight behind a line of precipitates. By increasing the external tension in step 2, the dislocation bends between the precipitates to circular or elliptical shape. In this process, the dislocation character changes from edge to screw in point n because the dislocation line becomes parallel to the Burgers vector in this point. In Eq. (43), $E(\pi/2 - \theta)$ is used instead of $E(\theta)$ because the original dislocation has opposite character at point n compared to point m. Analogously, if the original dislocation has screw character at point m ($\theta = 0$), the dislocation character at the adjacent precipitate is edge ($\theta = \pi/2$). In step 3, the dislocation escapes the first array of precipitates when the external tension is further increased and the initial dislocation character is restored. This condition represents the physical basis of the final shear stress expression in the Ashby model. Brown and Ham [8] approximated the condition of randomly distributed obstacles and reformulated Eq. (43) as,

$$\tau_{Orowan} = J\frac{2[E(0).E(\pi/2)]^{0.5}}{bL_s}. \tag{44}$$

Insertion of Eq. (1) with $\theta = 0$ and $\theta = \pi/2$ in Eq. (44) restores the well-known Orowan equation, which is,

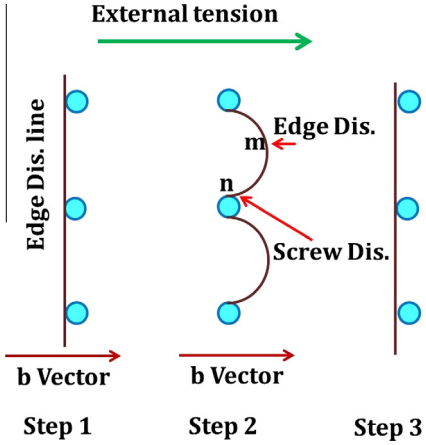

Fig. 7. Interaction between an edge dislocation with an array of non-shearable precipitates.

$$\tau_{Orowan} = \frac{JGb}{2\pi\sqrt{1-\upsilon}L_s} \ln\left(\frac{2r_s}{r_i}\right). \quad (45)$$

3. Discussion

The present set of strengthening equations shows that the maximum shear stress before yielding depends on the dislocation line tension T, the mean distance between two particles, the precipitate resistance force F, which is a function of precipitate radius or outer cut-off distance, and the particular strengthening mechanism. In contrast, conventional strengthening equations are often functions of the mean radius, phase fraction as well as physical and some coefficients [6–9,18,20,24–26,30]. When substituting the actual precipitate distribution by only the mean radius and phase fraction of precipitates, the calculated yield strength increments can become substantially different from experimental results. The differences usually arise from simplifications in the development of the strengthening equations. The most prominent are listed in Fig. 8.

For a predictive simulation of the total shear stress, we propose to refine the values of input variables instead of changing and adapting phenomenological coefficients in order to close the gap between experimental and simulation results. In a survey for evaluation of final yield strength in binary Ni–Al system, Ardell and Huang [32] have listed eight different values between 0.129 J/m^{-2} and 0.188 J/m^{-2} for the anti-phase boundary energy (γ_{APB}) of γ' from different references, while Douin et al. [33] measured γ_{APB} = 0.111 J/m^{-2} by using weak-beam electron microscopy.

In the present model, we have connected strengthening equations to the incipient physical parameters, which are varying during aging and we have avoided unnecessary simplifications commonly used in conventional models. This is discussed in detail subsequently.

3.1. Non-spherical precipitates

In some precipitation strengthening systems, for instance, Al–Mg–Si, Al–Cu, Al–Cu–Mg, Al–Zn–Mg and some nickel-base superalloys (Inconel 718, Rene 62, Udimet 630), precipitates are non-spherical. For these cases, the conventional strengthening equations are not applicable and it is difficult to advance these equations while being based on phenomenological parameters. Three different approaches are reported in literatures to simulate the yield strength for non-spherical precipitates:

(i) Myhr et al. [34] assumed that prolate precipitates are spherical in Al–Mg–Si system and applied conventional strengthening equations, thus simply ignoring the shape effect.
(ii) Nie and Muddle [35] modified the Orowan equation, Eqs. (44) and (45), for cylindrical disc shape precipitate in Al–Cu–Sn system by using a stereological method. They assumed that the aspect ratio is higher that 40 (diameter/thickness) and simulated the yield strength increment based on this assumption. In their model, they assumed that the precipitates are not shearable at all and ignored all shearing mechanisms. This model can be developed for rod shape precipitates in aluminum and magnesium alloys, too [36,37].
(iii) Computer simulations of moving dislocations in their slip plane were used in the method of Zhu and Starke [38], where the moving dislocations are crossing rod-shape particles elongated in ⟨100⟩ direction or circular platelet particles extended in the {100} planes [39–41]. Similar to Nie and Muddle [35], this method does not account for the case of coherent and shearable precipitates.

In our approach, as outlined in Section 2, the strengthening equations are functions of physical parameters only, which can straightforwardly be advanced for prolate and oblate precipitates considering all shearing and non-shearing strengthening mechanisms [11,31]. This task is performed in another work by the present authors.

3.2. Dislocation line tension

The dislocation line tension varies in the course of particle aging processes due to changes in the mean free distance between two particles along the dislocation line and the angle between the

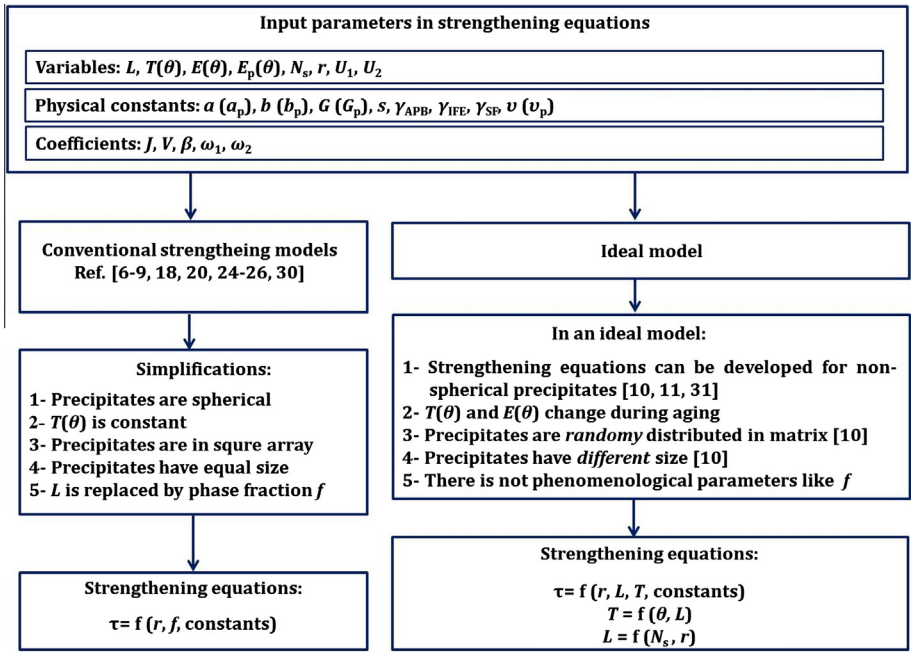

Fig. 8. Evolution of yield strength equations in conventional and ideal model.

dislocation line with the Burgers vector θ due to the dislocation bending behind a particle [42].

In the early stages of aging, precipitates are weak and the dislocation character remains unaffected when the dislocation is nearly straight. Once the precipitates grow, the dislocation character changes during bending behind the strong precipitates. Dieter [42] measured the dislocation energy per unit length based on Eq. (1) in annealed crystals. He assumed that $r_o = 10^{-7}$ m and $r_i = 2 \cdot 10^{-10}$ m; then $\ln(r_o/r_i) \approx 2\pi$. After replacing the parameters for outer and inner cut-off distance and using $\upsilon = 1/3$, the resulting dislocation energies for screw and edge dislocations become $E(0) = (1/2)Gb^2$ and $E(\pi/2) = (3/4)Gb^2$, respectively. In the same way, using Eq. (3), the dislocation line tension for screw and edge dislocations are $T(0) = Gb^2$ and $T(\pi/2) = (1/4)Gb^2$, respectively. In contrast, Ardell [9] proposed $\ln(r_o/r_i) \approx 4$ at peak strength. These different assumptions in conventional models produce rather large differences in the absolute value of the strengthening effect, thus indicating that the dislocation line tension is a critical parameter for precipitation strengthening. For simulation of the yield strength, the dislocation line tension is proposed to be $T = (1/2)Gb^2$ in Refs. [8,9,18,20,23,28,29,41].

In practical simulation, accurate result can only be obtained after performing a thorough characterization of the dislocation character, which is a mixture of edge or screw, and by accurately determining the free distance between two particles. Both these parameters are dynamic in nature and vary during aging.

3.3. Free distance between two precipitates

The free distance between two particles is a crucial input quantity in precipitation strengthening theory. In his early model, Ashby [7] assumed that all precipitates have the same size and that they are distributed on a square array without preferential point for nucleation. Based on these assumptions, the free distance between two precipitates, $L_{s,c}$, is represented in the following manner [7],

$$L_{s,c} = \left[\frac{1}{\sqrt{N_s}} - 2r_s\right], \tag{46}$$

where $L_{s,c}$ is the surface to surface distance between two particles located in the square arrangement and N_s is the number of particles, which intersect unit area of slip plane. The relation between N_s and the number of particles per unit volume of the matrix, N_v, is

$$N_s = 2\ r\ N_v. \tag{47}$$

Whereas the square array is a reasonable approximation of the real situation for many alloy systems, in other precipitation hardening materials, such as aluminum alloys AA2xxx and AA6xxx or γ"-hardened superalloys, precipitates nucleate in a close-packed triangular array [43]. In this case, $L_{s,c}$ should be modified to the following form, where the surface to surface distance between two particles located in triangular arrangement, $L_{s,t}$, is

$$L_{s,t} = \left[\frac{\sqrt{2/\sqrt{3}}}{\sqrt{2rN_v}} - 2r_s\right]. \tag{48}$$

In general, strengthening models based on Eqs. (46) and (48) (see the work of Russel and Brown [20], Kelly [44] and Fullman [45]) are physically correct. However, their accuracy decreases for small particles with $r < 0.04\ \bar{r}$, where $\bar{r}$ is the mean radius of precipitates. Moreover, when being applicable for $r < 0.04$, the results are not satisfying at $\bar{r}$. The phase fraction of precipitates has a similar effect on the free distance of two particles. In a numerical analysis, Sonderegger et al. [10] simulated the shearing of particles in the dislocation slip plane for 10^5 randomly distributed precipitates in 100 size classes in volume. They calculated the free distance distribution between two particles by varying radius at constant phase fraction and vice versa. Their simulation result showed that the deviation from numerical simulation could be 70% and more for the classical models.

These authors presented an alternative model for arbitrary precipitate size and randomly distributed particles in a matrix. In this model, precipitates are divided into discrete size classes. Each class contains precipitates from within a specific radius interval, r_c, and a number density of particles, $n_{v,c}$. A general formulation for the free distance between two particles in the slip plane is derived as

$$L_s = \sqrt{\frac{\ln 3}{2\pi\sum_c n_{v,c} r_c} + (2r_{ss})^2} - 2r_{ss}, \tag{49}$$

And

$$r_{ss} = \sqrt{\frac{2}{3}}\frac{\sum_c n_{v,c} r_c^2}{\sum_c n_{v,c} r_c}. \tag{50}$$

where r_{ss} is the mean projected radius. The Sonderegger et al. model delivers more accurate results for various size distributions and different phase fractions. The difference in free distance between two particles obtained from Eq. (49) and a numerical analysis of 10^5 randomly distributed precipitates in 100 size classes described in Ref. [10] is in all cases less than 30%.

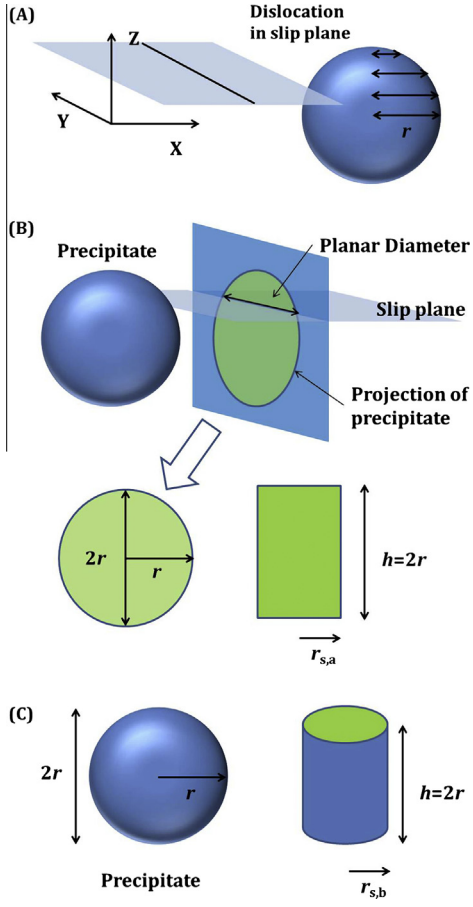

Fig. 9. (A) The interfering region between a precipitate and the dislocation slip plane, (B) planar radius in model of Ardell [9] and (C) radius of circular section in slip plane in model of Brown and Ham [8].

3.4. Equivalent radius

The spatial extension of the interfering part between a dislocation and a precipitate, the so-called equivalent radius, varies between 0 and the radius of the precipitate (Fig. 9A). There are two approaches to measure the equivalent radius, one by Ardell [9] and the second by Brown and Ham [8]. Ardell considered the projection of the precipitate onto a plane perpendicular to the slip plane of the dislocations. The resulting geometric figure is a circle with radius r and area πr^2 (Fig. 9B). Ardell then replaced this circle by a rectangle with the same area and same height in z direction. The average planar radius in this model is then

$$r_{s,a} = \frac{\pi}{4}\bar{r}. \tag{51}$$

In the Brown and Ham approach, illustrated in Fig. 9C, the volume effect is taken into account. Brown and Ham replaced the spherical precipitate by a cylindrical precipitate with the same volume ($4/3\ \pi r^3$) and same height in z direction. The mean radius of the circular section in the dislocation slip plane in this model is [8,30]

$$r_{s,b} = \sqrt{\frac{2}{3}}\,\bar{r}. \tag{52}$$

The difference between the equivalent radii of precipitates $r_{s,a}$ and $r_{s,b}$ in these two models is about 3.9%.

3.5. Strengthening mechanisms

During aging of a supersaturated alloy, nuclei of small particles initially grow until they finally coarsen by the mechanisms of Ostwald ripening and/or particle coalescence. As particle radii, phase fractions, precipitate free distances and number densities change in the course of precipitate evolution, so do their contributions to different strengthening mechanisms.

3.5.1. Phase fraction, free distance between precipitates and dislocation line tension

Fig. 10 illustrates changes in phase fraction (f), free distance between two precipitates along dislocation line (L_s, L_{eff}) and line tension (T) of an edge dislocation for cases where the number density of precipitates is held constant and the precipitate radius increases with aging time. The utilized values in this evaluation are summarized in Table 1.

Fig. 10a shows the phase fraction of precipitates in this system, which increases with aging time. In Ref. [9], Ardell defines a critical value for the validity of the shearing equations when the phase fraction of precipitate is lower than 40%. In this example, the phase fraction reaches 40% when the precipitate radius is approximately 70 nm.

The solid line in Fig. 10b shows changes in the surface-to-surface distance between two strong particles, L_s, as a function of precipitate size. L_s is equal to $L_{c,c}$ (center-to-center distance between two precipitates) when the equivalent radius is almost zero. In this example, L_s decreases linearly from 0.3 μm to 0.1 μm by increasing precipitate size from 0 to 100 nm during precipitate coarsening. L_s is independent of the type of strengthening mechanism, whereas L_{eff} depends on the maximum resistance force F_m and dislocation line tension in different strengthening mechanisms. The dash line in Fig. 10b shows virtual values for L_{eff} based on Eq. (6) in the coherency mechanism. In the same way, virtual values for L_{eff} can be calculated for other strengthening mechanisms. We can calculate a real L_{eff} value if we define the total force of different mechanism as explained in Section 2.3.

Replacing r_o in Eq. (3) by L_s delivers the dislocation line tension, T, which is illustrated by the solid line in Fig. 10c. The dash line in Fig. 10c represents the virtual line tension of dislocations when the operative mechanism is coherency strengthening.

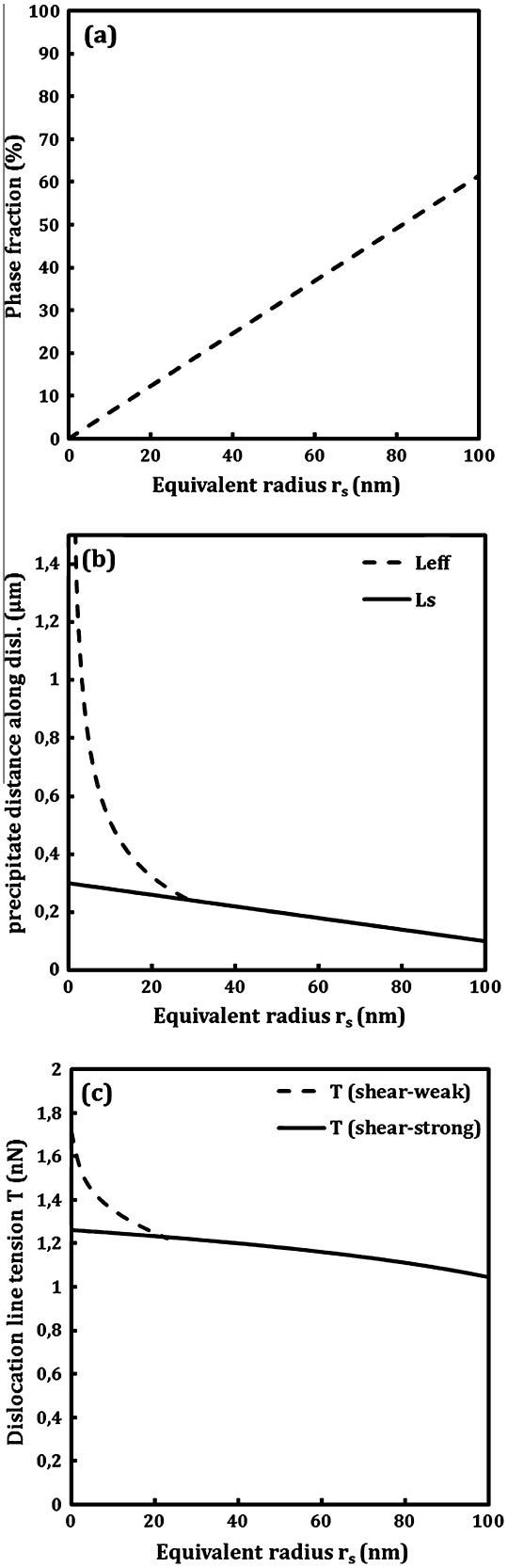

Fig. 10. Simulation of (a) phase fraction of precipitate, (b) surface-to-surface distance between two particles in weak and shearable mechanism L_{eff} and in strong mechanism L_s and (c) dislocation line tension force in weak and strong mechanisms.

Table 1
Physical and chemical parameters of the virtual matrix and precipitate, which are used for the strengthening simulations in Figs. 10 and 11.

Parameters	Values
$b = b_p$ (nm)	0.25
J	1
G (GPa)	79.3
G_p (GPa)	70.0
$L_{c,c}$ (nm)	300
r_i (nm)	2 b
S	2
ε	0.001
γ_{APB} (J m^{-2})	0.04
γ_{IFE} (J m^{-2})	0.5
γ_{SFM} (J m^{-2})	0.1
γ_{SFP} (J m^{-2})	0.05
υ	1/3

In all weak strengthening equations, except for the chemical effect, the precipitate resistance force increases with precipitate size. This causes a decrease in L_{eff} and T. In Eq. (6), L_{eff} is a function of T/F_m and, in Eq. (3), T is a function of L_{eff}. Eqs. (3) and (6), therefore, express the observation that L_{eff} and T are interdependent functions that change gradually with precipitate size.

Based on the present parameterization, we next analyze the role of changing precipitate radii for the simulated shear stress in different strengthening mechanisms.

3.5.2. Coherency effect

In the analysis of the coherency effect, which represents the interaction of the moving dislocation with the stress field generated by the lattice misfit between precipitate and matrix, we observe an increase of precipitation strengthening with increasing radius. In the model of Gerold and Haberkorn [18], the yield strength increment is caused by the strain field in z direction, which is the distance between the slip plane and the precipitate center. The strain fields along the dislocation line direction y and the direction of dislocation movement x does not influence the maximum resistance force in Eq. (7) (see Fig. 9A).

The weak and shearing regime of coherency strengthening is valid when the outer cut-off angle is $120° \leqslant \Psi_c \leqslant 180°$. With increasing precipitate radius, the maximum resistance force of the precipitate on the dislocation increases and the outer cut-off angle decreases. Then, the strengthening mechanism shifts from the weak and shearing regime (Eqs. (16) and (17)) to the strong and shearing regime (Eqs. (18) and (19)). In the weak and shearing regime, the strengthening effect strongly depends on the precipitate radius. When the strong and shearing mechanism is operative, an increase of the particle radius has a weaker effect. The critical particle size for transition, $\bar{r}$, from Eq. (16) to Eq. (18) for an edge dislocation is [8],

$$\bar{r}_{e,crit,weak} = \frac{J^{0.8}}{4\pi}\frac{35^{0.4}3^{0.3}}{296^{0.4}}\left(\frac{1-2\upsilon}{1-\upsilon}\right)\ln\left(\frac{L_{eff}}{r_i}\right)\frac{b}{\varepsilon}, \tag{53}$$

and for a screw dislocation,

$$\bar{r}_{s,crit,weak} = \frac{J^{0.8}}{4\pi}\frac{20^{0.4}}{9^{0.4}}\left(\frac{1+\upsilon}{1-\upsilon}\right)\ln\left(\frac{L_{eff}}{r_i}\right)\frac{b}{\varepsilon}. \tag{54}$$

Interestingly, the critical radius for transition from the weak to the strong mechanism of a screw dislocation is approximately 10 times higher than that of an edge dislocation when $\upsilon = 1/3$. This is obvious from comparison of Eqs. (53) and (54).

The regime defined by the strong and shearable mechanism is an intermediate mechanism between the weak and shearing mechanism and the Orowan mechanism. In some alloy systems, where the lattice misfit of precipitate and matrix is high, this regime becomes a virtual mechanism because the strengthening value obtained from Eqs. (18) and (19) is above the value given by the Orowan Eq. (43).

When the precipitate size increases during aging, the precipitates either lose coherency and become incoherent or they become so strong that they cannot be sheared any longer. The point, where the strengthening mechanism is converted from shearing to Orowan is reached when the outer cut-off angle Ψ_c reaches almost to zero and $F_m = 2T$. The transition criterion from shearing mechanism to Orowan mechanism for an edge dislocation is given by [8],

$$\bar{r}_{e,crit,strong} = \frac{1}{8\pi}\left(\frac{1-2\upsilon}{1-\upsilon}\right)\ln\left(\frac{L_s}{r_i}\right)\frac{b}{\varepsilon}, \tag{55}$$

and for a screw dislocation,

$$\bar{r}_{s,crit,strong} = \frac{1}{4\pi}\left(\frac{1+\upsilon}{1-\upsilon}\right)\ln\left(\frac{L_s}{r_i}\right)\frac{b}{\varepsilon}. \tag{56}$$

Eqs. (55) and (56) define a criterion for the transition radius from shearing to non-shearing, which is applicable for shear and strong equations in all the strengthening mechanisms. For the coherency mechanism, the maximum resistance force in front of the dislocation occurs outside the precipitate and the other strengthening effects such as APB, chemical and stacking fault effects, will be activated during the interaction between dislocation and precipitate. For the precipitates, which are larger than the critical radius mentioned in Eqs. (55) and (56), the strengthening mechanism is Orowan, although other strengthening mechanisms indicate that shearing mechanisms should be operative.

In Fig. 11(a–e), the weak and shearing regime and the strong and shearing regime in all strengthening mechanisms are displayed for interaction between precipitate and edge dislocation. The values utilized in the evaluation of different strengthening mechanisms are mentioned in Table 1.

3.5.3. Modulus effect

In the Siems et al. model [21], the shear stress generated by the modulus effect increases strongly up to a precipitate radius of $10{\cdot}r_i$. For larger radii, however, the modulus effect becomes almost independent of radius [24] (see Fig. 11b). In this model, which is valid for precipitates with lower shear modulus than the matrix, the strengthening weak Eq. (22) does not intersect the strong Eq. (23) and there is no transition radius from weak to strong mechanisms and Orowan mechanism. This result is in conflict with other strengthening mechanisms and models, which show a gradual change from weak to strong regimes.

In the Nembach model [24], the total shear stress increases monotonously. As shown in Fig. 11b, the weak mechanism is replaced by the strong mechanism as soon as the precipitate radius is approximately 40 nm. In many precipitation strengthening systems, the modulus effect is a weak strengthening mechanism compared to the coherency and APB effects [24]. But, in the Fe–Cu system, for instance, it is assumed to be the dominant mechanism [46].

For the calculation of the overall yield strength, we considered Eq. (27) for the weak and shearable effect and Eq. (28) for the strong and shearable effect.

3.5.4. Anti-phase boundary effect

An APB is a planar defect occurring in chemically ordered precipitates. Fig. 11c shows the effect of APB strengthening for an edge dislocation based on Eqs. (29)–(32). At the early aging stage, the weak and shearing equation is controlling the strengthening regime. The weak and shearing regime is smoothly replaced by the strong and shearing during aging. In contrast to the coherency

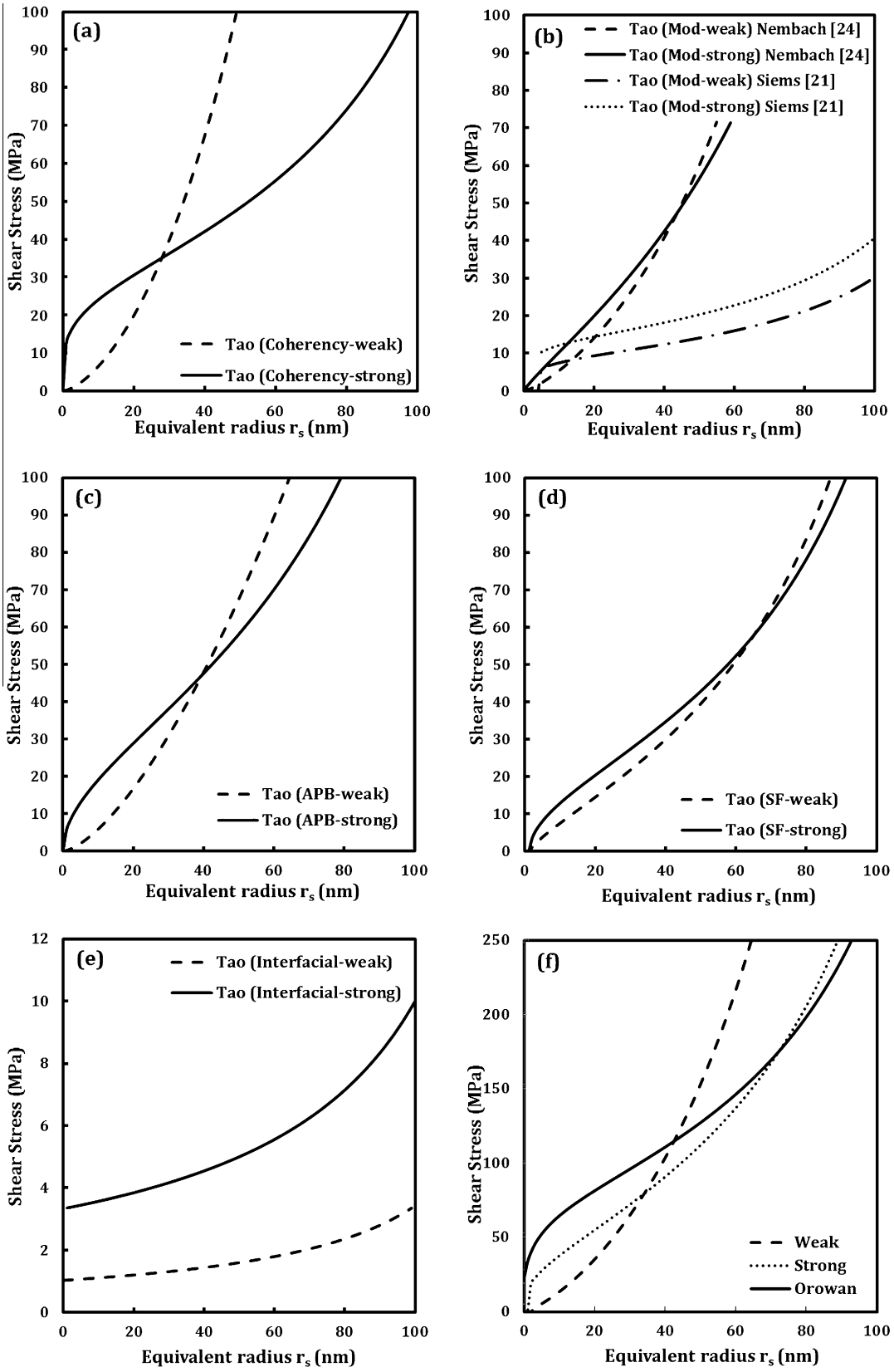

Fig. 11. Analysis of different weak and strong strengthening regimes for edge dislocations based on physical and chemical parameters defined in Table 1. The plots define (a) coherency effect, (b) modulus effect, (c) APB effect, (d) stacking fault effect and (e) interfacial effect. Plot (f) shows the combination of all the weak and strong strengthening mechanisms in plots (a–e) with the Orowan mechanism.

effect, where the maximum force between dislocation and precipitate depends on the position of the slip plane relative to the precipitate center. Here, the maximum force depends on the interplay between the energy of the swept area (see Fig. 5) and

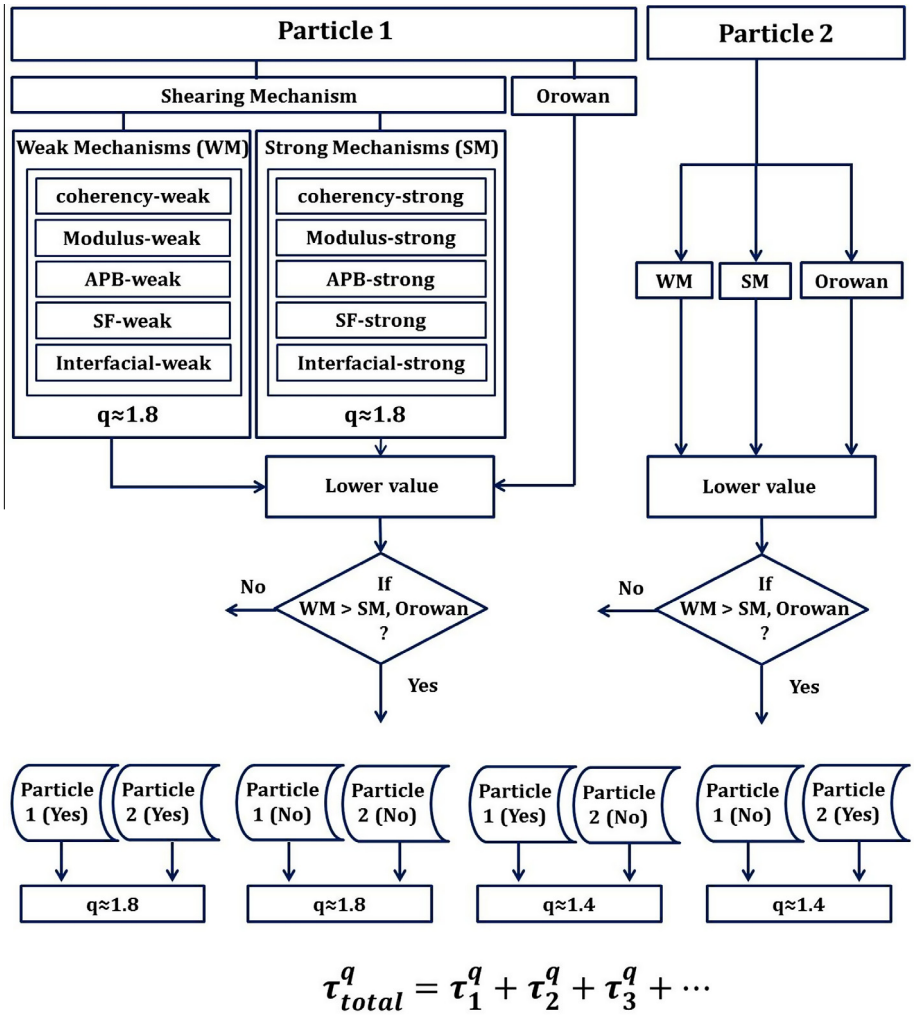

$$\tau_{total}^{q} = \tau_{1}^{q} + \tau_{2}^{q} + \tau_{3}^{q} + \cdots$$

Fig. 12. Combination of different strengthening weak mechanisms (WM) and strong mechanisms (SM) in a single or multi-particle system.

the distance between the leading and trailing dislocations. In ordered precipitates, the APB effect is often as strong as the coherency effect.

3.5.5. Stacking fault effect

When the stacking fault energy of precipitate and matrix are low, Eqs. (34) and (35) are the operative strengthening equations because the ribbon band between the two partial dislocations (P.1 and P.2) is wider than the precipitate diameter. During aging, the precipitate size increases and becomes larger than the ribbon band. Then, Eqs. (39) and (40) deliver more accurate results, particularly at the peak of the yield strength. Fig. 11d displays the shear stress increment due to the stacking fault effect as proposed in Eqs. (39) and (40). Similar to the other strengthening mechanisms, the weak regime is replaced by the strong regime above a specific precipitate size. This mechanism has often a minor effect on the final yield strength compared to the other mechanisms.

3.5.6. Interfacial effect

The interfacial effect has generally the weakest effect in precipitation hardening of shearable precipitates. Fig. 11e illustrates the magnitude of chemical strengthening in weak and strong regimes based on Eqs. (41) and (42). Unlike other strengthening mechanisms, chemical strengthening is the independent of precipitate size and increases by L_{eff} and L_s decrement, only.

3.6. Superposition of strengthening mechanisms

In precipitation-strengthened multi-component and/or multi-phase materials, the different nature and size of particles will lead to a situation where the total strengthening effect is given by a mixture of different strengthening mechanisms. Even with just one kind of precipitate, a distribution of particle sizes in different slip planes of dislocations must be expected, thus also representing a situation where each precipitate has different strengthening potential and the total strength contribution must in some way be superposed.

For a prediction of the combined effect of all individual strengthening contributions, several investigations have been performed and various approaches exist [8,9,47–49]. The basic result of these studies can be lumped up in the superposition expression

$$\tau_{total}^{q} = \sum_{i=1}^{n} \Delta\tau_{i}^{q}, \tag{57}$$

where q is an exponent, which commonly lies between 1 and 2. Eq. (57) delivers the shear stress of a precipitation-strengthened material with a mixture of operative strengthening mechanisms.

Numerical studies of Forman and Makin [50] for two types of obstacles with the same strength provide good agreement to the overall strength with a value of $q = 2$ (Pythagorean superposition). The same result is also proposed by Koppenaal [49]. In another

investigation, Ardell [9] applied computer simulations to determine the value of q for a mixture of two randomly distributed precipitate populations with distinct strength. He proposed that, for a combination of just weak mechanisms (WM) or just strong mechanisms (SM), q should be chosen close to 1.8. Otherwise, when two different mechanisms of weak and strong type are acting together, q should be given a value close to 1.4. Merging of weak and strong mechanisms in a multi-particle system (1,2,...) is demonstrated in Fig. 12 for the simple case of two particles.

In this figure, the q value for weak and shearable mechanism and strong and shearable mechanism is approximately 1.8. The operative strengthening mechanism for a specific precipitate is the one with lower strength among weak mechanism (WM), strong mechanism (SM) and Orowan mechanism. When there are different particles in the matrix, we can use the mixture law of Ardell [9]. As shown in the flowchart, q is 1.8 when the operative strengthening mechanism in different particles is WM. In the same way q is 1.8 when the operative strengthening mechanism in different particles is SM or Orowan mechanism. For the combination of WM with SM or Orowan mechanism q is 1.4. In the present study this procedure is utilized for superposition of all shearable and non-shearable effects including coherency, modulus, APB, stacking fault and interfacial effects. Fig. 11f displays the total yield strength in a material containing virtual precipitates defined in Table 1. This plot, which combines the contribution of different strengthening mechanisms as demonstrated in plots Fig. 11(a–e), describes weak mechanism as an operative mechanism for precipitate smaller than $r_s = 30$ nm. For coarser precipitate up to $r_s = 75$ nm, the operative mechanism is strong and shearable. The Orowan mechanism controls the final yield strength when the precipitate is larger than 75 nm.

4. Summary

In this paper, we review and discuss classical strengthening models for both, shearing and non-shearing, mechanisms. Where possible, these approaches are modified on basis of recent progress in modeling of essential input parameters for precipitation strengthening with the goal of making the strength predictions more quantitative and accurate.

The proposed equations are established on basis of physical input parameters. These are, among others, dislocation character, precipitate radius, outer cut-off distance and mean free distance between precipitates. Phenomenological parameters are widely avoided, thus increasing accuracy and predictability of the equations. The various strengthening equations are consistent among each other, since they are developed on basis of the same set of fundamental governing equations.

A procedure is proposed to identify the operative strengthening mechanism(s) for each individual precipitate from the analysis of strength contributions of the different individual shearing and non-shearing mechanisms. Finally, we suggest how to combine different strengthening mechanisms in complex systems to obtain the final yield strength of multi-phase, multi-particle materials.

Acknowledgements

The authors acknowledge the provision of samples by AMAG/Austria. Financial support by the Austrian Federal Government (in particular from the Bundesministerium für Verkehr, Innovation und Technologie and the Bundesministerium für Wirtschaft, Familie und Jugend) and the Styrian Provincial Government, represented by Österreichische Forschungsförderungs gesellschaft mbH and by Steirische Wirtschaftsförderungsgesellschaft mbH, within the research activities of the K2 Competence Centre on "Integrated Research in Materials, Processing and Product Engineering", operated by the Materials Center Leoben Forschung GmbH in the framework of the Austrian COMET Competence Centre Programme, is gratefully acknowledged.

References

[1] A. Wilm, Metallurgie 8 (1911) 225–227.
[2] P.D. Merica, R.G. Waltenberg, H. Scott, Bull. Am. Inst. Min. Metall. Eng. 150 (1919) 271–316.
[3] P.D. Merica, R.G. Waltenberg, J.R. Freeman Jr., Trans. Am. Inst. Min. Metall. Eng. LXIV (1921) 3–25.
[4] J.W. Cahn, Alloy Phase Diagr. 4 (1983) 349–351.
[5] N.F. Mott, F.R.N. Nabarro, Proc. Phys. Soc. 52 (1940) 86–89.
[6] E. Orowan, Symposium on Internal Stresses in Metals and Alloys, Session III Discussion, Institute of Metals, London, England, 1948, pp. 451–453.
[7] M.F. Ashby, in: G.S. Ansell, T.D. Cooper, F.V. Lenel (Eds.), Metallurgical Society Conference, vol. 47, Gordon and Breach, New York, 1968, pp. 143–205.
[8] L.M. Brown, R.K. Ham, in: A. Kelly, R.B. Nicholson (Eds.), Elsevier, Amesterdam, The Netherlands, 1971, pp. 9–135.
[9] A.J. Ardell, Metall. Trans. 16A (1985) 2131–2165.
[10] B. Sonderegger, I. Holzer, E. Kozeschnik, Ch. Sommitsch, Comput. Methods Mater. Sci. 11 (2011) 148–153.
[11] M.R. Ahmadi, B. Sonderegger, E. Povoden-Karadeniz, A. Falahati, E. Kozeschnik, Mater. Sci. Eng. A 590 (2014) 262–266.
[12] A.H. Cottrell, Prog. Met. Phys. 4 (1953) 205–208.
[13] A.J.E. Foreman, Acta Metall. 3 (1955) 322–330.
[14] C.H. Henager Jr., R.G. Hoagland, Scripta Mater. 50 (2004) 1091–1095.
[15] E. Clouet, Phys. Rev. B 84 (2011) 224111.
[16] E. Clouet, L. Ventelon, F. Willaime, Phys. Rev. B 84 (2011) 224107.
[17] J. Friedel, Gauthier-Villars Paris Fr, 1956, p. 205.
[18] V. Gerold, H. Haberkorn, Phys. Status Solidi (b) 16 (1966) 675–684.
[19] J.D. Eshelby, Proc. Roy. Soc. A241 (1957) 376.
[20] K.C. Russell, L.M. Brown, Acta Metall. 20 (1972) 969–974.
[21] R. Siems, P. Delavignette, S. Amelinckx, Phys Status Solidi (b) 2 (1962) 636–660.
[22] G. Knowles, P.M. Kelly, BSC/ISI Conf. Scarb., 1971.
[23] A. Deschamps, M. Militzer, W.J. Poole, ISIJ Int. 41 (2001) 196–205.
[24] E. Nembach, Phys. Stat. Sol. (a) 78 (1983) 571–581.
[25] E. Nembach, Prog. Mater. Sci. 45 (2000) 275–338.
[26] H. Gleiter, E. Hornbogen, Phys Status Solidi (b) 12 (1965) 251–264.
[27] J.S. Hou, J.T. Guo, J. Mater. Eng. Perform. 15 (2006) 67–75.
[28] W. Huther, B. Reppich, Z. Metallkde. 69 (1978) 628–634.
[29] P.B. Hirsch, A. Kelly, Phil. Mag. 12 (1965) 881–900.
[30] H. Gleiter, E. Hornbogen, Phys. Stat. Sol. (b) 12 (1965) 235–250.
[31] B. Sonderegger, E. Kozeschnik, Scripta Mater. 66 (2012) 52–55.
[32] A.J. Ardell, J.C. Huang, Phil. Mag. Lett. 58 (1988) 189–197.
[33] J. Douin, P. Veyssiere, P. Beauchamp, Phil. Mag. A 41 (1986) 21.
[34] O.R. Myhr, Ø. Grong, S.J. Anderson, Acta Mater. 49 (2001) 65–75.
[35] J.F. Nie, B.C. Muddle, Acta Mater. 56 (2008) 3490–3501.
[36] J.F. Nie, B.C. Muddle, J. Phase Equilib. 19 (1998) 543–551.
[37] J.F. Nie, Scripta Mater. 48 (2003) 1009–1015.
[38] A.W. Zhu, E.A. Starke Jr., Acta Mater. 47 (1999) 3263–3269.
[39] I.N. Khan, M.J. Starink, J.L. Yan, Mater. Sci. Eng. A 472 (2008) 66–74.
[40] G. Liu, G.J. Zhang, X.D. Ding, J. Sun, K.H. Chen, Mater. Sci. Eng. A 344 (2003) 113–124.
[41] M. Song, Mater. Sci. Eng. A 443 (2007) 172–177.
[42] G.E. Dieter, Mechanical Metallurgy, third ed., MaGraw-Hill Book Co, 1986.
[43] A.J.E. Foreman, M.J. Makin, Phil. Mag. 14 (1966) 911–924.
[44] P.M. Kelly, Int. Met. Rev. 18 (1973) 31–36.
[45] R.L. Fullman, Trans. AIME 197 (1953) 1267–1268.
[46] I. Holzer, E. Kozeschnik, Mater. Sci. Eng. A 527 (2010) 3546–3551.
[47] J.C. Huang, A.J. Ardell, Acta Metall. 36 (1988) 2995–3006.
[48] C. Schlieser, E. Nembach, Acta Metall. Mater. 43 (1995) 3983.
[49] T.J. Koppenaal, Appl. Phys. Lett. 4 (1964) 56.
[50] A.J.E. Foreman, M.J. Makin, Can. J. Phys. 45 (1967) 511–517.

Paper 2

Materials Science & Engineering A 590 (2014) 262–266

Contents lists available at ScienceDirect

Materials Science & Engineering A

journal homepage: www.elsevier.com/locate/msea

Precipitate strengthening of non-spherical precipitates extended in ⟨100⟩ or {100} direction in fcc crystals

M.R. Ahmadi [a,b,c,*], B. Sonderegger [d,e], E. Povoden-Karadeniz [a], A. Falahati [c], E. Kozeschnik [a,b,c]

[a] Christian Doppler Laboratory "Early Stages of Precipitation", Institute of Materials Science and Technology, Vienna University of Technology, Vienna, Austria
[b] Materials Center Leoben Forschungsgesellschaft mbH, Leoben, Austria
[c] Institute of Materials Science and Technology, Vienna University of Technology, Vienna, Austria
[d] Institute for Materials Science and Welding, Graz University of Technology, Graz, Austria
[e] Centre for Materials Engineering, Department of Mechanical Engineering, University of Cape Town, Cape Town, South Africa

ARTICLE INFO

Article history:
Received 9 September 2013
Received in revised form
13 October 2013
Accepted 15 October 2013
Available online 24 October 2013

Keywords:
Modeling
Precipitate strengthening
Ellipsoidal precipitates

ABSTRACT

In precipitation strengthening of non-spherical precipitates, the effective radius is depending on the relative orientation between particle and the direction of dislocation movement. Expressions for the equivalent precipitate radius applicable to particle shearing and non-shearing mechanism are derived for ellipsoidal particles taking into account their growth direction and the dislocation character (edge and screw). The results are compared to spherical particles and presented in the form of closed analytical correction factors.

1. Introduction

In precipitation hardening, the yield strength of materials increases because dispersed precipitates impede dislocation movement. A mathematical formulation has been introduced by Orowan in 1944 [1], and discussed by Ashby [2] and Brown and Ham [3] in more depth. The following expression holds,

$$\tau_{\mathrm{Orowan}} = \frac{Gb}{2\pi\sqrt{1-\upsilon}}\frac{1}{\lambda_{\mathrm{ss}}}\ln\left(\frac{R_{\mathrm{eq}}}{r_{\mathrm{i}}}\right), \tag{1}$$

where G is the shear modulus, υ is Poisson's ratio, r_{i} is the inner cut-off radius, R_{eq} is the outer cut-off radius, which is the average planar particle diameter for non-shearable particles, and λ_{ss} is the surface to surface distance between two particles. Orowan, Ashby, and Brown and Ham assume an equal number of edge and screw dislocations in their work.

Eq. (1) is applicable for hard, spherical and non-coherent particles without lattice continuity between precipitates and matrix. In this case, dislocations by-pass the precipitates and produce a dislocation loop around them.

In the case of non-spherical and non-shearable precipitates, Zhu and Starke [4] proposed strengthening equations for rod-shaped precipitates oriented in ⟨100⟩ direction and circular platelets extended in {100} planes. This model is based on computer simulations of moving dislocations in the precipitate crossing slip plane. Later, this method was widely used for simulation of precipitation strengthening of non-spherical precipitates in aluminum alloys [5–7]. Nie and Muddle [8] modified Eq. (1) by applying stereological method for triangular precipitate arrangement. In that model, precipitates are treated as cylindrical discs in the slip plane of fcc when the precipitate aspect ratio (thickness/diameter) is lower than 1/40. The stereological method is also applied for different precipitate orientations in fcc aluminum alloys [9] and for rod-shaped precipitates in hcp magnesium [10].

When dislocations interact with a coherent and shearable precipitate, they can pass through it, because atomic lattice continuity remains intact at the precipitate–matrix interface. During different shearing stages, a number of effects due to the dislocation-particle interaction can occur, which are (i) coherency strengthening due to lattice misfit, (ii) modulus strengthening (iii) anti-phase boundary strengthening, (iv) stacking fault strengthening and (v) interfacial strengthening. These effects lead to a resistance force F in front of the dislocation movement, which leads to dislocation bending. When the bending angle between two sides of the dislocation line behind a precipitate is between 180° and 120°, this precipitate is denoted as "weak". Brown and

* Corresponding author at: Institute of Materials Science and Technology, Vienna University of Technology, Vienna, Austria. Tel.: +43 1588 0130 885; fax: +43 1588 0130 895.
E-mail address: mohammad.ahmadi@tuwien.ac.at (M.R. Ahmadi).

0921-5093/$ - see front matter © 2013 Elsevier B.V. All rights reserved.
http://dx.doi.org/10.1016/j.msea.2013.10.043

Ham [3] and Ardell [11] analyzed the shear stress increment of weak precipitates for point obstacles as defined by Friedel [12], which are randomly distributed in the matrix. The strengthening equation for weak and shearable precipitates reads [11]

$$\tau_{\text{shear}} = \frac{2T}{b\lambda_{\text{ss}}}\left[\frac{F(r_{\text{eq}})}{2T}\right]^{\frac{3}{2}}, \tag{2}$$

$$F(r_{\text{eq}}) = k r_{\text{eq}}^{\text{m}}, \tag{3}$$

where T is the dislocation line tension, $F(r_{\text{eq}})$ is the resistance force in different shearing mechanisms in front of dislocation movement, r_{eq} is the equivalent radius of the particle in the slip plane and m is a constant in the range of 0–1. m is equal to one for anti-phase boundary and stacking fault effects [11]. It is equal to zero for the interfacial effect, which shows that this mechanism is independent of precipitate radius. For modulus strengthening, an intermediate m value is proposed between 0.72 and 0.90 [13], k is a constant depending on physical and chemical properties of the precipitate. This parameter is $k_{\text{int}} = 2\,\gamma_{\text{int}} b$ for the interfacial effect, where γ_{int} is the interfacial energy of the precipitate, $k_{\text{sf}} = 2|\gamma_{\text{sfm}} - \gamma_{\text{sfp}}|$ for the stacking fault effect, where γ_{sfm} and γ_{sfp} are the stacking fault energy of matrix and precipitates, respectively, $k_{\text{mo}} = 0.05|G - G_{\text{p}}|b^{2-m}$ for the modulus effect, where G_{p} is the shear modulus of the precipitate and $k_{\text{apb}} = 2\gamma_{\text{apb}}$ for the anti-phase boundary effect, where γ_{apb} is the anti-phase boundary energy of the precipitate [11]. In spherical homogeneous precipitates, the physical and chemical properties are identical in all main crystallographic directions. This means that the interaction between precipitate and dislocation is independent of slipping direction and dislocation edge or screw character. In inhomogeneous precipitates, different length of lattice parameters promotes preferential growth in different directions, which leads to the formation of non-spherical precipitates. Even though, in this case, k depends on the orientation of the precipitate with respect to the slipping direction of edge or screw dislocations. In the present work, we consider k as a constant for each strengthening mechanism. This model excludes coherency strengthening, because in this effect, the maximum resistance force in front of the dislocation movement occurs outside the precipitate and it is independent of the length of the dislocation inside the precipitate. The yield strength increment due to the coherency effect depends on the position of the slip plane with respect to the precipitate center and we will discuss on this effect in a separate paper.

In the point obstacle model of Friedel [12], λ_{ss} is equal to the center to center distance between two particles λ_{cc}. For the realistic case of a precipitate with finite size, the final shear stress evaluated by Eq. (2) is higher than that for a point obstacle precipitate. This means that Eq. (2) requires a correction for precipitates with finite size. Ardell [11] modified Eq. (2) by subtracting the maximum length of a dislocation inside the precipitate from the center to center distance between two particles, which is $\lambda_{\text{ss}} = \lambda_{\text{cc}} - 2r_{\text{s}}$.

Eqs. (1)–(3) show that the final shear stress is a function of the free distance λ_{ss} between two precipitates and r_{eq} or R_{eq}, if one assumes that the resistance force of the precipitate does not influence the dislocation character during interaction, i.e., T remains constant. In this study, we apply Eqs. (1)–(3) for non-spherical precipitates and analyze the interaction between non-spherical precipitates with screw or edge dislocations similar to the Ardell's assumptions [11] for spherical precipitates.

1.1. Free distance between precipitates

Sonderegger and et al. [14] proposed a model for the free distance between precipitates with arbitrary size and random distribution. In this model, precipitates are divided in different classes. Each class i contains particles with specific mean radius $r_{\text{v},i}$ and a number density $n_{\text{v},i}$. A general formulation for the free distance between two particles in the slip plane is derived as

$$\lambda_{\text{ss}} = \sqrt{\frac{\ln 3}{2\pi\sum_i n_{\text{v},i} r_{\text{v},i} + (2r_{\text{s}})^2}} - 2r_{\text{s}}, \tag{4}$$

with

$$r_{\text{s}} = \sqrt{\frac{2}{3}\frac{\sum_i n_{\text{v},i} r_{\text{v},i}^2}{\sum_i n_{\text{v},i} r_{\text{v},i}}} \tag{5}$$

Eqs. (4) and (5) are established for spherical particles. For ellipsoid precipitates in fcc structure, Sonderegger and Kozeschnik [15] introduced a correction factor for λ_{ss}, depending on a shape factor h, as

$$\lambda_{\text{ss,ell}} = h^{\frac{1}{6}}\left(\frac{2+h^2}{3}\right)^{\frac{-1}{4}}\lambda_{\text{ss}}, \tag{6}$$

$$h = \frac{c}{a}, \tag{7}$$

where $\lambda_{\text{ss,ell}}$ is the free distance between two ellipsoidal precipitates and replaces λ_{ss} for spherical particles. c is the half axes of the particle parallel to its rotational axes and a is the according half length perpendicular to the rotational axes. In this model, precipitates can be rotational needle-shaped ellipsoids (prolate), which are elongated in ⟨100⟩ directions, or rotational lens-shaped ellipsoids (oblate) elongated in {100} planes. In case of ellipsoids, r denotes the radius of a sphere with identical volume.

In the same way we develop a model for the equivalent precipitate radius of rotational needle-shaped or rotational lens-shaped ellipsoids elongated in the mentioned in ⟨100⟩ directions or in {100} planes.

2. Model development

The equivalent precipitate radius of spherical precipitates is defined by Ardell [11] for the shearing mechanism with

$$r_{\text{eq}} = \frac{\pi}{4} r, \tag{8}$$

and for Orowan mechanism as

$$R_{\text{eq}} = 2r_{\text{eq}} \tag{9}$$

Eqs. (8) and (9) are established for spherical particles, but in fact, precipitates often have different shapes and orientations. Examples for fcc-structured non-spherical precipitates are β″ needles oriented in ⟨100⟩ directions in aluminum 6xxx series, and θ'' and γ'' precipitates extended in {100} planes in aluminum 2xxx series and Inconel 718, respectively. In the present modeling, gradual evolution from spherical to needle-shaped particles in fcc-structure is described by the prolate-type precipitate in ⟨100⟩ directions ($h > c/a$). The oblate-type represents precipitates extending in {100} planes ($h < c/a$).

In ellipsoidal precipitates, the shape and growth direction of precipitates associated with the slip plane is shown schematically in Fig. 1. In this figure, the distance between two parallel slip planes, which surround the precipitate, is

$$2n = 2rh^{\frac{-1}{3}}\sqrt{(\sin\alpha)^2 + h^2(\cos\alpha)^2}, \tag{10}$$

where α is the angle between the rotational axes of the precipitate (assumed to be [100] here) relative to the normal direction of slip plane [111]; $\alpha = 54°73'$. With these assumptions, Eq. (10) can be

simplified to

$$2n = 2rh^{\frac{-1}{3}}\sqrt{\frac{2}{3}+\frac{h^2}{3}} \tag{11}$$

The outer cut-off radius in the Orowan mechanism and the diameter of precipitates in the shearing mechanism are equal for spherical precipitates because the cross section of precipitates with the slip plane is circular. Thus, the movement of screw or edge dislocations in different directions has the same "trace" on the precipitates. In contrast, the cross section of ellipsoidal precipitates with the slip plane is an ellipse. As a consequence, both, the outer cut-off radius and the precipitate radius, depend on the length of this ellipse and its orientation relative to the movement of the dislocation. In the following, the half axes of the cross section ellipse are referred to as r_a and r_c, where r_c is parallel to the projection of the particle rotation axes into the slip plane. The mean values of these parameters are found using the normal distance n as

$$2n \times 2r_c = \pi ac, \tag{12}$$

$$r_c = \frac{\pi}{4} r h^{\frac{2}{3}}\sqrt{\frac{3}{2+h^2}}, \tag{13}$$

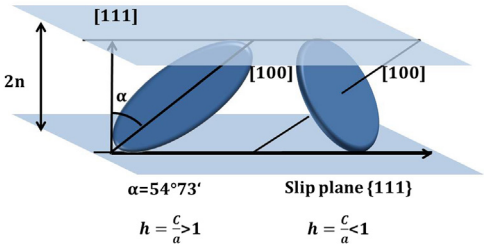

Fig. 1. Prolate and oblate precipitates elongated in ⟨100⟩ and {100} directions, which are confined between two parallel slip planes {111}.

$$r_a = \frac{\pi}{4}a = \frac{\pi}{4\frac{r_c}{h^{\frac{1}{3}}}} \tag{14}$$

The shape and orientation of these cross sections relative to the dislocation movements are illustrated in Fig. 2.

Since the rotation axes of the particles are assumed to be [100], [010] or [001], the according projections in the slip plane (r_c) are parallel to $\left[\,\bar{1}\;2\;\bar{1}\,\right]$, $\left[\,\bar{1}\;\bar{1}\;2\,\right]$ or $\left[\,2\;\bar{1}\;\bar{1}\,\right]$, respectively. We introduce the angle φ, indicating the angle between r_c and the moving direction of the dislocations. This angle is $\varphi_1=0$, $\varphi_2=2\pi/3$ and $\varphi_3=-2\pi/3$ for edge dislocations and $\varphi_4=\pi/2$, $\varphi_5=\pi/6$ and $\varphi_6=-\pi/6$ for screw dislocations.

Interaction mechanisms between a dislocation and shearable and non-shearable precipitates are different. Here, we distinguish between equivalent precipitate radius for shearable precipitates and equivalent outer cut-off radius for non-shearable precipitates.

2.1. Equivalent precipitate radius in shearing mechanism

Since dislocations are assumed to be straight for the shearing mechanism, the dislocation length inside a precipitate during shearing is maximal when the dislocations are located at the center of the precipitate for spherical and ellipsoidal precipitates. This leads to an expression for the maximum length of the dislocation line in the particle, ω_{eq}, which is therefore referred to as "effective equivalent radius", with

$$\omega_{eq}(\varphi,h) = \frac{\pi}{4} r h^{\frac{2}{3}}\sqrt{\frac{3(1+(\tan\varphi)^2)}{2+h^2(1+3(\tan\varphi)^2)}} \tag{15}$$

Table 1 summarizes $\omega_{eq}(\varphi,h)$ values for the different angles φ of interest.

In the case where an edge or screw dislocation experiences each precipitate orientation with the same probability, the average

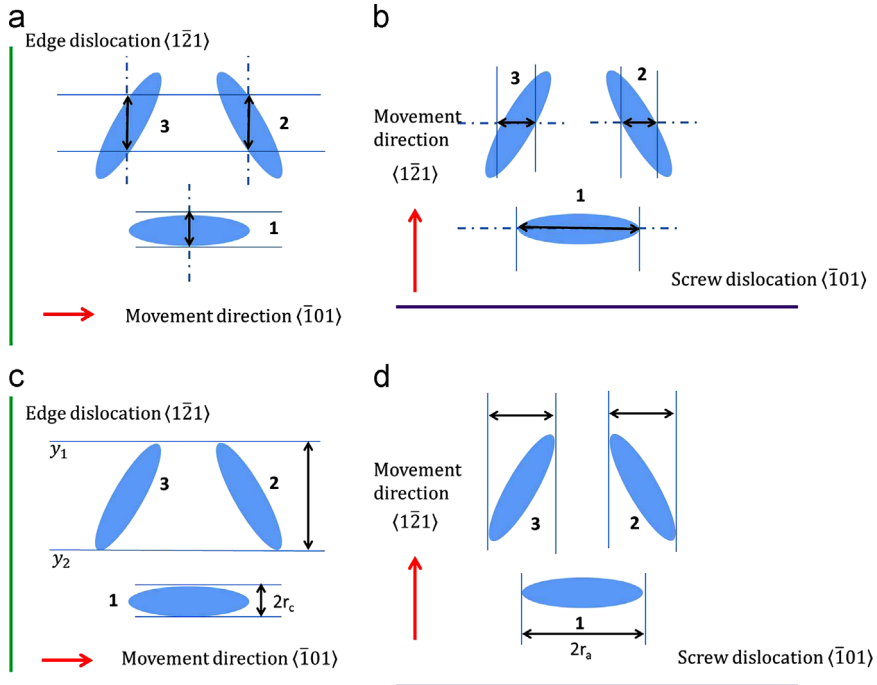

Fig. 2. (a and b) Length of edge and screw dislocations in oblate precipitates for the shearing mechanism, (c and d) projections of precipitates on edge and screw dislocations for the non-shearing mechanism.

Table 1
Equivalent radius $\omega_{eq}(\varphi, h)$ of precipitates in different positions of matrix and equivalent outer cut-off radius $R_{eq}(\varphi, h)$ inside the precipitates for different angle φ.

Disl. type	Angle φ	$\omega_{eq}(\varphi, h)$	$R_{eq}(\varphi, h)$
Edge	$\varphi_1 = 0$	$\frac{\pi}{4} h^{\frac{2}{3}} \sqrt{\frac{3}{2+h^2}}\, r$	$\frac{\pi}{2} h^{\frac{2}{3}} \sqrt{\frac{3}{2+h^2}}\, r$
	$\varphi_{2,3} = \frac{\pm 2\pi}{3}$	$\frac{\pi}{4} h^{\frac{2}{3}} \sqrt{\frac{6}{1+5h^2}}\, r$	$\frac{\pi}{2} h^{\frac{2}{3}} \sqrt{\frac{3}{4h^2} + \frac{3}{4(2+h^2)}}\, r$
Screw	$\varphi_4 = \frac{\pi}{2}$	$\frac{\pi}{4} h^{\frac{2}{3}} \sqrt{\frac{1}{h^2}}\, r$	$\frac{\pi}{2} h^{\frac{2}{3}} \sqrt{\frac{1}{h^2}}\, r$
	$\varphi_{5,6} = \frac{\pm \pi}{6}$	$\frac{\pi}{4} h^{\frac{2}{3}} \sqrt{\frac{2}{1+h^2}}\, r$	$\frac{\pi}{2} h^{\frac{2}{3}} \sqrt{\frac{1}{4h^2} + \frac{9}{4(2+h^2)}}\, r$

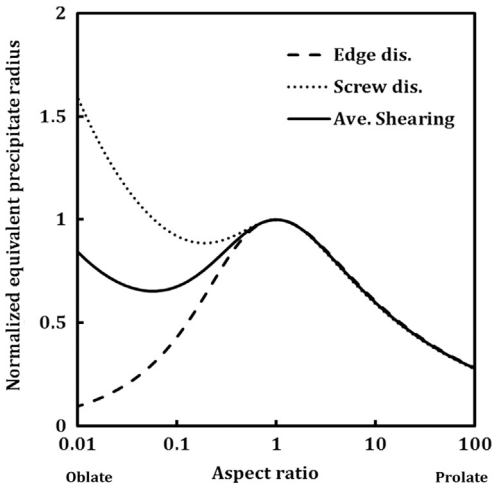

Fig. 3. Normalized equivalent precipitate radius for edge and screw dislocations in the shearing mechanism.

mean values $\overline{\omega}_{eq}$ are found as

$$\overline{\omega}_{eq,edge}(h) = \left\{ \frac{1}{3} \left[\sqrt{\frac{3}{2+h^2}} + 2\sqrt{\frac{6}{1+5h^2}} \right] h^{\frac{2}{3}} \right\} r_{eq}, \tag{16}$$

$$\overline{\omega}_{eq,screw}(h) = \left\{ \frac{1}{3} \left[\frac{1}{h} + 2\sqrt{\frac{2}{1+h^2}} \right] h^{\frac{2}{3}} \right\} r_{eq}, \tag{17}$$

$$\overline{\omega}_{eq}(h) = P_1 \overline{\omega}_{eq,edge}(h) + P_2 \overline{\omega}_{eq,screw}(h), \tag{18}$$

where P_1 and P_2 are the fraction of edge and screw dislocations in the matrix, respectively.

Eq. (18) defines a coefficient for ellipsoidal precipitates for the shearing mechanism. Replacing r_{eq} by $\overline{\omega}_{eq}(h)$ in Eqs. (2) and (3) introduces a more general equation, which is applicable for spherical precipitates, too.

Fig. 3 shows the normalized equivalent precipitate radius as function of the aspect ratio for a system including pure edge or screw dislocations. Accordingly, edge and screw dislocations face the same equivalent precipitate radius for shearing of needle-shape particles. For plates, the situations differ. The normalized equivalent radius generally decreases for edge dislocations with lower aspect ratios, whereas, for screw dislocations, a minimum is found at an aspect ratio of approximately 0.2. This means that the dislocation character can change from screw to edge, which results in a lower force to shear oblate precipitate.

2.2. Equivalent outer cut-off radius in non-shearing mechanism

In the non-shearing mechanism (Orowan mechanism), dislocations are blocked in front of the precipitates and do not shear them. Consequently, the precipitate-dislocation interaction is independent of the intrinsic precipitate properties. The outer cut-off radius, R_{eq}, is the full width of the particles cross-section normal to the direction of dislocation movement and, thus, also depending on r_a, r_c and φ, see Fig. 2.

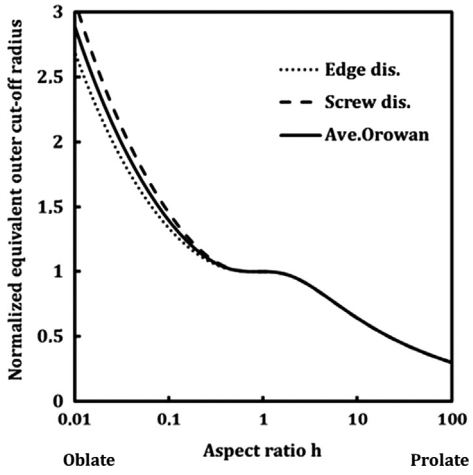

Fig. 4. Normalized equivalent outer cut-off radius for edge and screw dislocations for the non-shearing mechanism.

This geometric configuration, finally, leads to an expression for the outer cut-off radius R_{eq} as

$$R_{eq}(\varphi, h) = \frac{|h_1 - h_2|}{\sqrt{1 + (1/(\tan\ \varphi)^2)}} = 2\sqrt{r_c^2(\cos\ \varphi)^2 + r_a^2(\sin\ \varphi)^2} \tag{19}$$

The geometry of the particles relative to the moving dislocations for the Orowan mechanism is the same as for the shearing mechanism, which leads to mean outer cut-off radii of

$$\overline{R}_{eq,edge}(h) = \left\{ \frac{1}{3} \left[\sqrt{\frac{3}{2+h^2}} + \sqrt{\frac{3}{h^2} + \frac{3}{2+h^2}} \right] h^{\frac{2}{3}} \right\} 2r_{eq}, \tag{20}$$

$$\overline{R}_{eq,screw}(h) = \left\{ \frac{1}{3} \left[\sqrt{\frac{1}{h^2} + \frac{9}{2+h^2}} + \frac{1}{h} \right] h^{\frac{2}{3}} \right\} 2r_{eq} \tag{21}$$

$$\overline{R}_{eq}(h) = P_1 \overline{R}_{eq,edge}(h) + P_2 \overline{R}_{eq,screw}(h) \tag{22}$$

Eq. (22) defines a coefficient for ellipsoidal precipitates in the Orowan mechanism. Replacing R_{eq} by $\overline{R}_{eq}(h)$ in Eq. (1) provides a general equation, which is applicable for spherical and ellipsoidal precipitates.

Fig. 4 shows the normalized equivalent outer cut-off radius $\overline{R}^*_{eq}(h) = \overline{R}_{eq}(h)/(2r_{eq})$ for a system including pure edge or screw dislocations. The value of $\overline{R}^*_{eq}(h)$ decreases for prolate particles and increases for oblate particles. There is no remarkable difference between edge and screw dislocations for the Orowan mechanism. It means, the correction factor is independent of the dislocation character.

3. Conclusion

In the present model, we take into account that the free distance between two precipitates decreases when the precipitate shape deviates from spherical. This effect generally increases the yield strength of the material, which has been demonstrated in previous work. In our present treatment we show that the increase of the equivalent radius of oblate precipitates in both, shearing and non-shearing mechanisms, additionally increases the final yield strength.

In contrast, the decrease of the equivalent radius of prolate precipitates decreases the final yield strength. This negative effect is partially compensated by the decreasing mean distance between prolate precipitates such that the final yield strength is close to the one of spherical precipitates.

Acknowledgments

The authors acknowledge financial support by the Austrian Federal Government (in particular from the Bundesministerium für Verkehr, Innovation und Technologie and the Bundesministerium für Wirtschaft, Familie und Jugend) and the Styrian Provincial Government, represented by Österreichische Forschungsförderungsgesellschaft mbH and by Steirische Wirtschaftsförderungsgesellschaft mbH, within the research activities of the K2 Competence Center on "Integrated Research in Materials, Processing and Product Engineering", operated by the Materials Center Leoben Forschung GmbH in the framework of the Austrian COMET Competence Center Programme, is gratefully acknowledged.

References

[1] E. Orowan, Symposium on Internal Stresses in Metals and Alloys, Session III Discussion, Institute of Metals, London, England, 1948, pp. 451–453.
[2] M.F. Ashby, in: G.S. Ansell, T.D. Cooper, F.V. Lenel (Eds.), Metallurgical Society Conference, vol. 47, Gordon and Breach, New York, 1968, pp. 143–205.
[3] L.M. Brown, R.K. Ham, in: A. Kelly, R.B. Nicholson (Eds.), Elsevier, Amesterdam, The Netherlands, 1971, pp. 9–135.
[4] A.W. Zhu, E.A. Starke Jr., Acta Mater. 47 (1999) 3263–3269.
[5] I.N. Khan, M.J. Starink, J.L. Yan, Mater. Sci. Eng. A 472 (2008) 66–74.
[6] G. Liu, G.J. Zhang, X.D. Ding, J. Sun, K.H. Chen, Mater. Sci. Eng. A 344 (2003) 113–124.
[7] M. Song, Mater. Sci. Eng. A 443 (2007) 172–177.
[8] J.F. Nie, B.C. Muddle, Acta Mater. 56 (2008) 3490–3501.
[9] J.F. Nie, B.C. Muddle, J. Phase Equilib. 19 (1998) 543–551.
[10] J.F. Nie, Scr. Mater. 48 (2003) 1009–1015.
[11] A.J. Ardell, Metall. Trans. 16A (1985) 2131–2165.
[12] J. Friedel, Gauthier-Villars Paris Fr (1956) 205.
[13] E. Nembach, Phys. Stat. Sol. (a) 78 (1983) 571–581.
[14] B. Sonderegger, I. Holzer, E. Kozeschnik, Ch. Sommitsch, Comp. Methods Mater. Sci. 11 (2011) 148–153.
[15] B. Sonderegger, E. Kozeschnik, Scr. Mater. 66 (2012) 52–55.

Paper 3

Available online at www.sciencedirect.com

ScienceDirect

Scripta Materialia 84–85 (2014) 47–50

Scripta MATERIALIA

www.elsevier.com/locate/scriptamat

A model for coherency strengthening of large precipitates

M.R. Ahmadi,[a,b,c,*] E. Povoden-Karadeniz,[a] B. Sonderegger,[d] K.I. Öksüz,[c] A. Falahati[c] and E. Kozeschnik[a,b,c]

[a] *Christian Doppler Laboratory for Early Stages of Precipitation, Institute of Materials Science and Technology, Vienna University of Technology, Favoritenstr. 9-11/E308, A-1040 Vienna, Austria*

[b] *Christian Doppler Laboratory for Early Stages of Precipitation, Department of Physical Metallurgy and Materials Testing, Montanuniversität Leoben, Franz-Josef Straße 18, 8700 Leoben, Austria*

[c] *Institute of Materials Science and Technology, Vienna University of Technology, Favoritenstr. 9-11/E308, A-1040 Vienna, Austria*

[d] *Centre for Materials Engineering, Department of Mechanical Engineering, University of Cape Town, Cape Town, South Africa*

Received 14 February 2014; revised 17 April 2014; accepted 22 April 2014
Available online 28 April 2014

In precipitation strengthening, the lattice misfit between precipitate and matrix produces a strain field around precipitates, which impedes dislocation movement. In this paper, a strengthening model is presented, which delivers the stress increment associated with the strain field around large homogeneous spherical precipitates. In contrast to previous work, this study takes into account that the effective resistance force on the dislocation depends strongly on the relative position of the slip plane to the precipitate center. On ignoring this effect, the maximum shear stress due to the strong and shearing mechanism is generally underestimated. The results are presented in the form of discrete equations based on the evaluation of the resistance force in front of a moving edge or screw dislocation and, alternatively, with a correction factor for conventional strong and shearing equations.

Keywords: Coherency strengthening; Large precipitate; Shear stress

The coherency effect describes a common strengthening mechanism, which exists in most precipitation strengthening systems. The lattice misfit between a coherent precipitate and the surrounding matrix produces a strain field around the precipitate, which hinders dislocation movement and which leads to dislocation bending. A precipitate is called "small", when the operative strengthening mechanism is weak, because the maximum angle between two arms of a dislocation behind a precipitate, the "outer cut-off angle" Ψ, is between 180° and 100°. They are denoted as "large" precipitates, when the resistance force is high enough to be in the region of the strong mechanism by decreasing Ψ between ~100° and 0° [1].

The only operative strengthening mechanism for small precipitates is the coherency weak and shearing mechanism [1,2]. In contrast, the operative strengthening mechanisms related to large precipitates are the weak and strong mechanisms simultaneously, depending on the position of the slip plane with respect to the precipitate center. This paper analyzes the shear stress increment of large precipitates by calculating the precipitate resistance force F in front of the moving dislocation in different slip planes, where the coherency strengthening problem involving large precipitates is treated as a superposition of particles where the weak mechanism is operative, and particles which act as strong precipitates. Considering both, the weak (c-w) and strong mechanism (c-s) for large precipitates, a gap in previous model descriptions is closed.

Gerold and Haberkorn [3] formulated the resistance force F in front of a moving edge or screw dislocation in a homogeneously strained matrix, depending on the precipitate radius r and precipitate lattice misfit ($\Delta a/a$) as

$$F\left(\frac{z}{r}\right) = 4Gb|\varepsilon|r\varphi\left(\frac{z}{r}\right) \quad (1)$$

* Corresponding author at: Christian Doppler Laboratory for Early Stages of Precipitation, Institute of Materials Science and Technology, Vienna University of Technology, Favoritenstr. 9-11/E308, A-1040 Vienna, Austria. Tel.: +43 1 58801 30885; fax: +43 1 58801 30895; e-mail: mohammad.ahmadi@tuwien.ac.at

http://dx.doi.org/10.1016/j.scriptamat.2014.04.019
1359-6462/

$$\varepsilon = \frac{1}{3}\left(\frac{1+\upsilon}{1-\upsilon}\right)\frac{\Delta a}{a} \tag{2}$$

where b is the magnitude of the Burgers vector, G is the shear modulus, ε is the constrained strain produced by the stress-free strain of linear lattice misfit, υ is Poisson's ratio, Δa is the difference between lattice constants of matrix and precipitate, a is the lattice constant of the matrix, and $\varphi(z/r)$ is a function that relates the maximum force to the dislocation position in the slip plane, with z being the distance (always taken positive) of the slip plane from the precipitate center. For a screw dislocation

$$\varphi\left(\frac{z}{r}\right) = \frac{1}{2}\left(\frac{z}{r}\right) \text{ if } \left(\frac{z}{r}\right) \leqslant 1 \tag{3}$$

$$\varphi\left(\frac{z}{r}\right) = \frac{1}{2\left(\frac{z}{r}\right)^2} \text{ if } \left(\frac{z}{r}\right) \geqslant 1 \tag{4}$$

and for an edge dislocation

$$\varphi\left(\frac{z}{r}\right) = 2\left(\frac{z}{r}\right)\sqrt{1-\left(\frac{z}{r}\right)^2} \text{ if } \left(\frac{z}{r}\right) \leqslant \frac{\sqrt{3}}{2} \tag{5}$$

$$\varphi\left(\frac{z}{r}\right) = \frac{3\sqrt{3}}{8\left(\frac{z}{r}\right)^2} \text{ if } \left(\frac{z}{r}\right) \geqslant \frac{\sqrt{3}}{2} \tag{6}$$

Figure 1 shows the dependence of the normalized precipitate resistance force in front of edge and screw dislocations with respect to their positions in the slip plane evaluated by Eq. (1) for varying z/r ratio.

The resistance force F has a maximum in front of screw and edge dislocations when $z/r = 1$ and $z/r = \sqrt{2}/2$, respectively. The maximum resistance force F_{max} in front of an edge dislocation is two times higher than that in front of a screw dislocation. At $z/r > 1$, no physical contact between precipitate and dislocation occurs, but F is nevertheless non-zero, because the strain field part lying outside the precipitate still contributes to the impedance of dislocation movement.

Figure 2 exemplarily compares the resistance forces in front of a screw dislocation for the cases of small (F_{small}) and large (F_{large}) precipitates. The argumentation for edge dislocations is analogous. The maximum shearing force produced by a bent screw dislocation behind a precipitate at $\Psi \approx 0°$ is $F = 2T$, indicated by the vertical line in Figure 2.

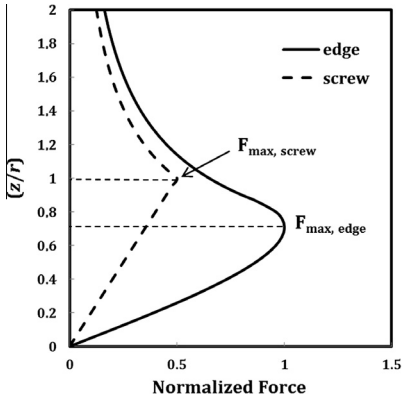

Figure 1. Normalized resistance force in front of edge and screw dislocations due to the strain field around a precipitate.

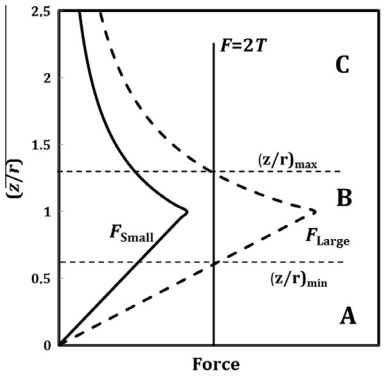

Figure 2. Resistance force of small and large precipitates, shown schematically. The interaction between large precipitates and a dislocation produces two "weak" regions (A and C) and one "strong" region (B).

T is the dislocation line tension, which is given as [1,2].

$$T(\theta) = \frac{Gb^2}{4\pi}\left(\frac{1+\upsilon-3\upsilon(\sin\theta)^2}{1-\upsilon}\right)\ln\left(\frac{r_o}{r_i}\right) \tag{7}$$

where θ is the angle between the dislocation line and its Burgers vector, and r_o and r_i are the outer cut-off and inner cut-off distances, respectively. The logarithmic part was approximated by Ardell [2] with $\ln(r_o/r_i) \approx 4$. In the present context, this value is irrelevant, because it cancels out on comparison of Eqs. (23) and (24) with Eq. (8).

Consider the case where the resistance force for small precipitates F_{small} at its maximum at $(z/r) = 1$ is lower than $2T$. Consequently, the dislocation can shear the weak precipitate when Ψ is between 180° and 100°. In contrast, for a large precipitate and for the present example, F_{large} can reach up to $2T$ when Ψ is between 100° and 0° in region B. Consequently, the critical precipitate radius for transition from small to large is $r_{crit,edge} = T/(2Gb\varepsilon)$ and $r_{crit,screw} = T/(Gb\varepsilon)$ for edge and screw dislocations, respectively, where Ψ reaches a value close to 0°. In Figure 2, three different regions, A, B and C, are distinguished to describe the interaction between a screw dislocation and a large precipitate, where region B is strong and shearable, and regions A and C are weak and shearable.

Possible regions of interaction between a dislocation and small precipitates are shown schematically in Figure 3a. In this case, the precipitate resistance force is lower than $2T$ in all planes intersecting the precipitate region, and the precipitate acts as c-w in all the interactions. The final shear stress is then simply given by the superposition of all distinct shear stress contributions based on the sum of square method, as suggested in Refs. [1,2,4]. Figure 3b depicts the situation where a dislocation interacts with large precipitates. If the interaction between two sides of a dislocation is c-w (regions A and C) or c-s on both sides of a dislocation, the sum of square method is also applicable for evaluation of the shear stress [1,2,4]. Otherwise, when a precipitate is c-w on one side of a dislocation and c-s on the other side, Ardell's method is used, described below [2].

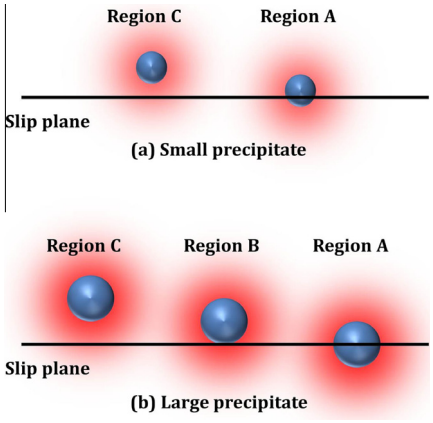

Figure 3. Interaction between a dislocation in its slip plane with the strain field around (a) small coherent precipitates, where the operative strengthening regime is weak and (b) large coherent precipitates in different regions: (A) where $(z/r)<(z/r)_{\min}$; (B) where $(z/r)_{\min}<(z/r)<(z/r)_{\max}$; (C) where $(z/r)>(z/r)_{\max}$.

Ignoring the effect of the c-w mechanism in regions A and C, Brown and Ham [1] proposed an expression for the shear stress increment of strong precipitates, where Ψ is close to 0°, but the precipitate still acts as shearable, as

$$\tau_{strong,B\&H} = J\frac{M\,T}{b\,\lambda_{ss}}(\psi(r))^{\frac{1}{4}} = J\frac{M\,T}{br}\sqrt{\frac{3f}{2\pi}}(\psi(r))^{\frac{1}{4}} \tag{8}$$

with

$$\psi(r) = \frac{Gb\varepsilon r}{T} \tag{9}$$

and

$$f = \left(\frac{2\pi}{3}\right)\left(\frac{r}{\lambda_{ss}}\right)^2 \tag{10}$$

λ_{ss} is the free distance between two precipitates in slip plane, J is a correction factor (equal to 0.8) for the free distance between randomly distributed precipitates in a slip plane, and f is the precipitate phase fraction. M is a constant equal to 2 and $2^{1/2}\times 3^{3/8}$ for screw and edge dislocation, respectively [5]. Eq. (8) is widely used in the literature [6–9] for evaluation of the c-s mechanism. The strengthening effect arising from regions A and C (Fig. 2) is ignored, however, in Eq. (8) [1]. Whereas this simplification is not critical for region A (decreasing effect with increasing precipitate size), region C can have a considerable impact on the shear stress increment for strong precipitates.

For the c-w contribution in regions A and C (Fig. 2) and equal dislocation character in all regions, the shear stress increment due to the interaction between screw dislocations and a precipitate is [2]

$$\tau_{c-w} = \frac{1}{b\,\lambda_{ss}\sqrt{2\,T}}\sqrt{\int_0^{(z/r)_{\min}} F^3\left(\frac{z}{r}\right)\frac{dz}{r} + \int_{(z/r)_{\max}}^{\infty} F^3\left(\frac{z}{r}\right)\frac{dz}{r}} \tag{11}$$

The shear stress increment of the strong part B is

$$\tau_{c-s} = J\frac{2\,T}{b\,\lambda_{ss}}\sqrt{\int_{(z/r)_{\min}}^{(z/r)_{\max}}\frac{dz}{r}} \tag{12}$$

Following the aforementioned treatment to combine c-w and c-s regimes, Ardell's generalized law of mixture is used [2], based on the computer simulation experiments of Foreman and Makin [10], which is proposed for all obstacles in the matrix as a generalization of the sum of square method, with

$$\tau_{total}^{q} = \tau_{c-w}^{q} + \tau_{c-s}^{q} \tag{13}$$

where the exponent q is typically between one and two. For combinations of c-w and c-s, Ardell [2] proposed a value of $q = 1.4$.

The $(z/r)_{\min}$ and $(z/r)_{\max}$ values for interaction between screw dislocation and precipitate are $(T/(G\varepsilon br))$ and $(G\varepsilon br/(T))^{0.5}$, respectively, by replacing $F = 2T$ in Eqs. (1), (3), and (4). The shear stress of the weak and strong parts (Eqs. (11) and (12)) then becomes

$$\tau_{c-w,screw} = \frac{2T}{b\,\lambda_{ss}}\left\{\frac{1}{4\psi(r)} + \frac{1}{5}\sqrt{\psi(r)}\right\}^{\frac{1}{2}} \tag{14}$$

and

$$\tau_{c-s,screw} = J\frac{2\,T}{b\,\lambda_{ss}}\left\{\sqrt{\psi(r)} - \frac{1}{\psi(r)}\right\}^{\frac{1}{2}} \tag{15}$$

Replacing $\tau_{c\text{-}w}$ and $\tau_{c\text{-}s}$ in Eq. (13) by Eqs. (14) and (15) delivers

$$\tau_{total,screw} = \frac{2T}{b\,\lambda_{ss}}\left\{\left[\frac{1}{4\psi(r)} + \frac{1}{5}\sqrt{\psi(r)}\right]^{\frac{q}{2}} + J\left[\sqrt{\psi(r)} - \frac{1}{\psi(r)}\right]^{\frac{q}{2}}\right\}^{\frac{1}{q}} \tag{16}$$

Figure 4 shows the ratio of shear stress in region A divided by shear stress in region C ($=R_1$) for the total shear stress of a strong precipitate, assuming $T = (2/\pi)Gb^2$, $\upsilon = 1/3$, $b = 2.5\times10^{-10}$ and $\varepsilon = 0.1$.

When the precipitate radius is <1.5 nm, the operative strengthening mechanism is c-w. In this range, the share stress contribution of region A is higher than that of region C, where R_1 is >1. With increasing precipitate radius, R_1 decreases, and the impact of region C on the total shear stress overcomes region A. When the precipitate radius reaches ~9 nm, R_1 becomes <10%. The curve R_2 shows the shear stress ratio of the c-s mechanism divided by the c-w mechanism. The R_2 value

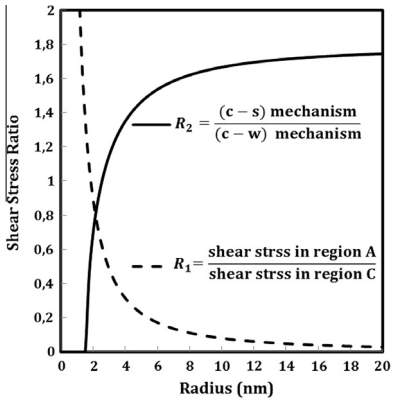

Figure 4. Ratio of shear stress in different region of coherent precipitate using $T = (2/\pi)Gb^2$, $\upsilon = 1/3$, $b = 2.5\times10^{-10}$ and $\varepsilon = 0.1$.

is zero in the early stage (radius $\leqslant$1.5 nm). It increases with increasing precipitate size until it reaches a plateau. For increasing precipitate size, regions B and C provide the main contributions to the total shear stress.

For evaluation of the interaction between edge dislocation and precipitates, the same constraints and calculation steps as used for the case of screw dislocations are applied. Consequently, replacing $F = 2T$ in Eqs. (1), (5), and (6), the value of $(z/r)_{\min}$ becomes

$$\left(\frac{z}{r}\right)_{\min} = \frac{\sqrt{2}}{2}\sqrt{1-\sqrt{1-\left(\frac{1}{2\psi(r)}\right)^2}} \tag{17}$$

and $(z/r)_{\max}$ delivers

$$\left(\frac{z}{r}\right)_{\max} = \frac{\sqrt{2}}{2}\sqrt{1+\sqrt{1-\left(\frac{1}{2\psi(r)}\right)^2}}, \quad \text{if} \quad \frac{T}{2Gb\varepsilon} \leqslant r \leqslant \frac{\sqrt{3}T}{3Gb\varepsilon} \tag{18}$$

$$\left(\frac{z}{r}\right)_{\max} = \frac{3^{\frac{3}{4}}}{2}\sqrt{\psi(r)}, \quad \text{if} \quad \frac{\sqrt{3}T}{3Gb\varepsilon} \leqslant r \leqslant \infty \tag{19}$$

Eq. (18) emphasizes that, in the early stages of precipitate evolution from small to large size, $(z/r)_{\max}$ differs from Eq. (19). For simplicity, this small step is ignored in Eq. (18), although this effect produces a minor error just in the mentioned precipitate size. Consequently, for the shear stress of the c-w and c-s regions in a large precipitate with an edge dislocation, one obtains

$$\tau_{c-w,edge} = \frac{2T}{b\lambda_{ss}}\left\{(2\psi(r))^3\left[\frac{16}{35}-\frac{\sqrt{2}}{70}\left(1+\sqrt{1-\left(\frac{1}{2\psi(r)}\right)^2}\right)^{\frac{5}{2}}\left(9-5\sqrt{1-\left(\frac{1}{2\psi(r)}\right)^2}\right)\right]+\frac{1}{5}\sqrt{\frac{3^{1.5}}{4}\psi(r)}\right\}^{\frac{1}{2}} \tag{20}$$

and

$$\tau_{c-s,edge} = J \times \frac{2T}{b\lambda_{ss}}\left\{\sqrt{\frac{3^{1.5}}{4}\psi(r)}-\sqrt{\frac{1}{2}-\frac{1}{2}\sqrt{1-\left(\frac{1}{2\psi(r)}\right)^2}}\right\}^{\frac{1}{2}} \tag{21}$$

Substituting Eqs. (20) and (21) into Eq. (13) delivers

$$\tau_{total,edge} = \frac{2T}{b\lambda_{ss}}\left\{\left\{(2\psi(r))^3\left[\frac{16}{35}-\frac{\sqrt{2}}{70}\left(1+\sqrt{1-\left(\frac{1}{2\psi(r)}\right)^2}\right)^{\frac{5}{2}}\left(9-5\sqrt{1-\left(\frac{1}{2\psi(r)}\right)^2}\right)\right]+\frac{1}{5}\sqrt{\frac{3^{1.5}}{4}\psi(r)}\right\}^{\frac{q}{2}} + J\left\{\sqrt{\frac{3^{1.5}}{4}\psi(r)}-\sqrt{\frac{1}{2}-\frac{1}{2}\sqrt{1-\left(\frac{1}{2\psi(r)}\right)^2}}\right\}^{\frac{q}{2}}\right\}^{\frac{1}{q}} \tag{22}$$

Accordingly, the relative contribution of region A decreases with increasing precipitate size, and Eqs. (16) and (22) can thus be simplified for large precipitates, i.e. negligible region A, as

$$\tau_{total,screw} = \frac{2T}{b\lambda_{ss}}\left\{\left[\frac{1}{5}\sqrt{\psi(r)}\right]^{\frac{q}{2}}+J\left[\sqrt{\psi(r)}\right]^{\frac{q}{2}}\right\}^{\frac{1}{q}} \tag{23}$$

and

$$\tau_{total,edge} = \frac{2T}{b\lambda_{ss}}\left\{\left\{\frac{1}{5}\sqrt{\frac{3^{1.5}}{4}\psi(r)}\right\}^{\frac{q}{2}}+J\left\{\sqrt{\frac{3^{1.5}}{4}\psi(r)}\right\}^{\frac{q}{2}}\right\}^{\frac{1}{q}} \tag{24}$$

Combination of Eqs. (23) and (24) with Eq. (8) delivers a correction factor for the shear stress of large precipitates for both, edge and screw dislocations, as

$$\tau_{total} = \left\{\left(\frac{1}{J\sqrt{5}}\right)^q+1\right\}^{\frac{1}{q}} \times \tau_{strong,B\&H} \tag{25}$$

Eq. (25) shows that identical correction terms of the simplified model description for τ_{c-s} [1] are required for both screw and edge dislocations.

Consequently, the Brown and Ham equation (Eq. (8)) needs a modification to reflect these contributions. If one assumes $J = 0.81$ as a correction factor for randomly distributed precipitates in a slip plane, and $q = 1.4$ for the mixture of contributions from c-w and c-s mechanisms [2], the strengthening equation for strong coherent precipitates from Brown and Ham [1] significantly underestimates the strengthening contribution by ~30%.

Financial support by the Austrian Federal Government (in particular from Bundesministerium für Verkehr, Innovation und Technologie and Bundesministerium für Wirtschaft, Familie und Jugend) represented by Österreichische Forschungsförderungsgesellschaft mbH and the Styrian and the Tyrolean Provincial Government, represented by Steirische Wirtschaftsförderungsgesellschaft mbH and Standortagentur Tirol, within the framework of the COMET Funding Programme is gratefully acknowledged.

[1] L.M. Brown, R.K. Ham, in: Kelly, R.B. Nicholson (Eds.), Strengthening Methods in Crystals Elsevier Publishing, Elsevier, Amsterdam, The Netherlands, 1971, pp. 9–135.
[2] A.J. Ardell, Metall. Trans. 16A (1985) 2131.
[3] V. Gerold, H. Haberkorn, Phys. Status Solidi (b) 16 (1966) 675.
[4] T.J. Koppenaal, Appl. Phys. Lett. 4 (1964) 59.
[5] M.R. Ahmadi, E. Povoden-Karadeniz, K.I. Öksüz, A. Falahati, E. Kozeschnik, Comp. Mater. Sci. COMMAT5823, doi: http://dx.doi.org/10.1016/j.commatsci.2014.04.025, in print.
[6] Zhanli Guo, N. Saunders, A.P. Miodownik, J-Ph. Schillé, Mater. Sci. Forum 546–549 (2007) 1319.
[7] T. Gladman, Mater. Sci. Technol. 15 (1999) 30.
[8] Zhanli Guo, W. Sha, Mater. Trans. 43 (2002) 1273.
[9] R.E. Smallman, Modern Physical Metallurgy, Butterworths, London, 1985.
[10] A.J.E. Foreman, M.J. Makin, Can. J. Phys. 45 (1967) 511.

Paper 4

Advanced Materials Research Vol. 922 (2014) pp 7-12
© (2014) Trans Tech Publications, Switzerland
doi:10.4028/www.scientific.net/AMR.922.7

Simulation of yield strength in Allvac® 718Plus™

M.R. Ahmadi[1,2,3,a], L. Whitmore[4,b], E. Povoden-Karadeniz[1,c],M. Stockinger[5.d], A. Falahati[3,e] and E. Kozeschnik[1,2,3,f]

[1] Christian Doppler Laboratory "Early Stages of Precipitation", Institute of Materials Science and Technology, Vienna University of Technology, Vienna, Austria.
[2] Materials Center Leoben Forschungsgesellschaft mbH, Leoben, Austria.
[3] Institute of Materials Science and Technology, Vienna University of Technology, Vienna, Austria.
[4] Christian Doppler Laboratory for Early Stages of Precipitation, Department of Physical Metallurgy and Materials Testing, Montanuniversität Leoben, Franz-Josef Straße 18, 8700 Leoben, Austria
[5] Böhler Schmiedetechnik GmbH & Co KG, Mariazellerstr. 25, A-8605 Kapfenberg, Austria

[a] mohammad.ahmadi@tuwien.ac.at, [b] lwhitmore@amberwebdesigns.net,
[c]erwin.povoden-karadeniz@tuwien.ac.at, [d] martin.stockinger@bohler-forging.com,
[e]ahmad.falahati@tuwien.ac.at, [f]ernst.kozeschnik@tuwien.ac.at

Keyword: precipitation strengthening, shearing mechanism, anti-phase boundary, coherency strengthening, nickel based superalloy

Abstract

In the present study, we describe a comprehensive and consistent physical model for the yield strength change in Allvac® 718Plus™ caused by precipitation strengthening. The model incorporates the effect of different shearing and non-shearing mechanisms with respect to atomic continuity between the lattices of precipitates and matrix. We demonstrate that coherency and anti-phase boundary effects are the major strengthening mechanisms in this alloy. The final yield strength of Allvac® 718Plus™ during aging is investigated using the thermo-kinetic software MatCalc. The calculated final yield strength evolution is consistent with experimental results.

1 Introduction

Engine performance in aerospace and power generation improves with increasing operation temperature, thus emphasizing the importance of understanding materials with good mechanical properties at high temperatures. Inconel 718 is a nickel based superalloy, which is widely used in aerospace and gas turbine engine applications because of superior high temperature mechanical properties [2] up to 650°C.
In 2004, Allvac® 718Plus™ (hereafter 718Plus) was introduced by ATI Allvac, giving 55K higher service temperature compared to Inconel 718 [3]. 718plus has a similar chemical composition to Inconel 718, however, with higher Ti+Al, Al/Ti ratio and approximately 1% Tungsten. In addition, approximately 50% of Fe is replaced by Co. With this chemical composition, γ' formation is strongly favored in place of γ'', thus eliminating the weakening effect in 718 due to γ'' transformation. The γ' phase is a stable fcc $(Ni,Co)_3(Al,Ti,Cr,Nb)$ precipitate with $L1_2$ structure, with a roughly spherical morphology at low phase fractions and remaining coherent even after over aging [2, 4].
The focus of this paper is the anti-phase boundary (APB) and coherency strengthening effects caused by γ' precipitation.

2 Experimental and computational procedures

MatCalc version 5.52 (rel 0.031) is used for simulation with the thermodynamic database *mc_ni_v2.000_015* and the diffusion database *mc_ni_v2.000_001* [1]. The composition of 718Plus is given in Table 1.

Table 1: Alloying composition of Inconel 718Plus in weight percent [Wt.%]

	Al	Co	Cr	Nb	C	Fe	Mo	Ti	W	Ni
[Wt.%]	1.46	9.13	17.42	5.48	0.028	9.66	2.72	0.71	1.04	bal.

The conventional heat treatment process applied in this work is solution annealing at 975°C for 60 minutes, followed by cold water quenching and aging at 788°C. Hardness and yield strength are measured subsequent to heat treatment and at room temperature. Vickers hardness is measured with a Vickers hardness tester FV 4E to identify precipitation hardening at five aging times (1, 5, 10, 25 and 50 hours). Yield strength is measured by compression testing carried out three times for each sample with Zwick Z250 testing devices. For transmission electron microscopy (TEM) analysis, the specimens are ground with silicon carbide papers down to 0.1mm and electropolished in a solution containing 5% perchloric acid and 95% ethanol at 32 V and -10 °C. The FEI Tecnai F20 microscope is operated with 200 kV acceleration voltage. All samples are pre-cleaned in a He plasma in order to remove surface oxides and impurities.

3 Strengthening model

The final yield strength in heat treatable materials is calculated as a superposition of the inherent stress of the base metal σ_i, grain boundary strengthening σ_g, solid solution strengthening σ_s , work hardening σ_w and precipitation strengthening σ_p, [6].

3.1 Precipitation strengthening. The shearing component of the precipitation strengthening process contains several different strengthening mechanisms: (i) interfacial strengthening, (ii) modulus strengthening, (iii) coherency strengthening and (iv) APB strengthening. Coherency and APB effects are the two predominant strengthening effects in the 718Plus superalloy.

3.1.1 Shearing mechanisms. In this section, we describe the coherency and APB effects for the cases when precipitates are small and shearable (weak mechanism) or large and shearable (strong mechanism).

Coherency effect. The difference in lattice parameter between the precipitate and matrix produces a strain field around the precipitate which hinders dislocation movement. Brown and Ham [7] proposed a strengthening equation for weak and shearable precipitates based on the Gerold and Haberkorn [8] coherency model as

$$\tau_{Coh,weak} = k\left(\frac{G^3 b \varepsilon^3 \bar{r}^3}{L_s^2 T(\theta)}\right)^{\frac{1}{2}}, \tag{1}$$

with,

$$\varepsilon \approx \frac{2}{3}|\delta| \quad \text{and} \quad T(\theta) = \frac{Gb^2}{4\pi}\left(\frac{1+\upsilon-3\sin^2\theta}{1-\upsilon}\right)\ln\left(\frac{r_o}{r_i}\right). \tag{2}$$

k is a constant equal to 4.11 and 1.38 for edge and screw dislocations, respectively. G is the shear modulus, assumed to be 78.0 GPa [4], b is the Burger's vector (0.254 nm), $\bar{r}$ is the precipitate mean radius and L_s the surface-to-surface distance between two precipitates. υ is Poisson's ratio (~0.33), ε is the constrained strain produced by the stress-free strain of lattice misfit δ [9]. δ is the strain measured with 0.004 in this study by TEM analysis. r_o is the outer cut-off distance, which is equal to the distance between two particles along the dislocation line for shearable precipitates [7, 10]. r_i is the inner cut-off distance (=2b [10]) and Θ is the angle between the dislocation line and its Burger's vector in Eq. 2.

The shear stress in Eq. 1 is valid for weak precipitates. For strong precipitates, Brown and Ham [7] proposed the following strengthening equation

$$\tau_{Coh,strong} = \frac{m}{L_s}\left(\frac{T^3(\theta) G \varepsilon \bar{r}}{b^3}\right)^{\frac{1}{4}}, \tag{3}$$

with m being equal to 2.1 and 2 for edge and screw dislocations, respectively.

Anti-phase boundary effect. The anti-phase boundary effect is a strengthening mechanism for ordered precipitates during shearing by dislocations. For weak precipitates

$$\tau_{APB,weak} = \left\{ \frac{2T}{b L_s} \left[\frac{\pi \gamma_{APB} \bar{r}}{4T} \right]^{\frac{3}{2}} - \frac{\pi}{3} \frac{\gamma_{APB} (\bar{r})^2}{b L_s^2} \right\}, \quad (4)$$

where γ_{APB} is the APB energy of γ' (=0.111 Jm^{-2} , Ref. [13]). For strong and shearable ordered precipitates, Hüther and Reppich [11] proposed

$$\tau_{APB,strong} = \left(\frac{2wT}{\pi b L_s} \right) \left(\frac{\pi^2 \gamma_{APB} \bar{r}}{4wT} - 1 \right)^{\frac{1}{2}} \quad (5)$$

where *w* is a parameter introduced for remaining dislocation segments incorporating also some other uncertainties. Its value is estimated to be 2.8.

3.1.2 Non-shearing mechanism. At the last stage of aging, the precipitate resistance force in front of the dislocation is sufficiently high to block dislocation movement. The yield strength increases even if the precipitates are still coherent with the matrix. In 1944, Orowan [12] proposed a strengthening equation for spherical and non-shearable precipitates. This equation is modified to the generally accepted form by Ashby [5] and Brown and Ham [7] as

$$\tau_{Orowan} = \frac{Gb}{2\pi\sqrt{1-\upsilon}} \frac{1}{L_s} \ln\left(\frac{\pi}{2} \frac{\bar{r}}{r_i} \right). \quad (6)$$

3.2 Mixture of shearing mechanisms. A general approximation for superposition of different weak or strong strengthening mechanisms *i* was proposed by Ardell [10] to calculate the yield strength increase due to the different strengthening mechanisms with

$$\sigma_{y.p} = M \left(\tau_{Coh,i}^{1.8} + \tau_{APB,i}^{1.8} \right)^{\frac{1}{1.8}}, \quad (7)$$

where *M* is the Taylor factor for converting shear stress to yield strength (*M* ~ 2.6) [14].

4 Results and discussion

The formation of γ' precipitates during aging produces the major effect on the final yield strength in 718Plus. The proposed strengthening equations in section 3.1 are functions of size and distribution of γ', which vary as a consequence of the applied heat treatment. Fig. 1 shows TEM dark field images of 718Plus after aging at 788°C for 1, 10 and 50 hours.

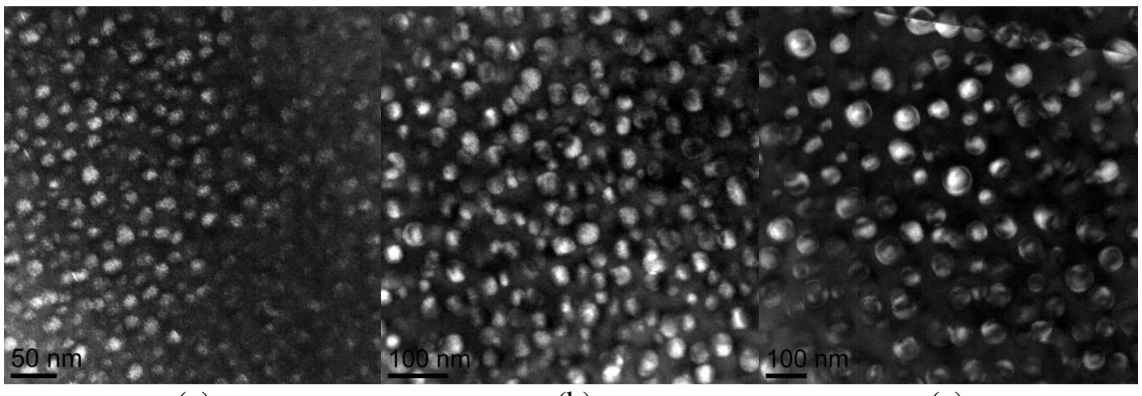

(a) (b) (c)

Fig. 1: Dark field images of 718Plus after aging at 788°C for (a) 1 hr (b) 10 hrs (c) 50 hrs.

From Fig. 1, it is clear that the size of the spherical γ' precipitates increases during aging, while their number density N_s decreases. Simulation of mean radius and number density of γ' is shown in Fig. 2 compared with the experimental results of measurements from the TEM investigation.

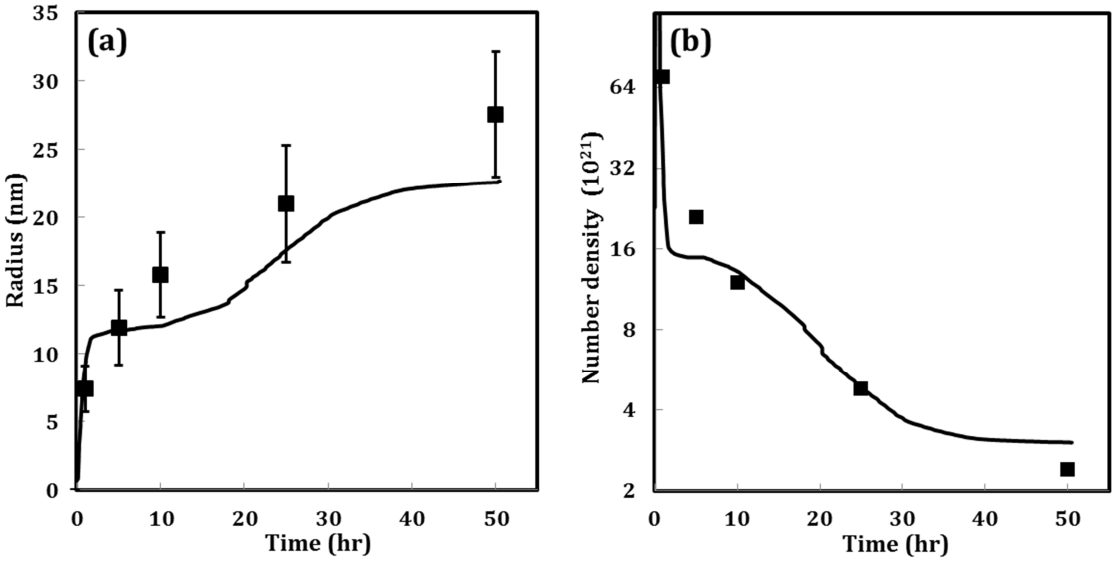

Fig. 2: Simulation result of (a) mean radius (b) number density for 718Plus as a function of aging time at 788°C compared with experimental TEM results

N_s appears in the strengthening equations indirectly as $L_s=1/\sqrt{N_s}$. The simulated and experimental results of aging shown in Fig. 2 demonstrate that precipitate mean radius increases during aging time (improves yield strength) whereas precipitate number density decreases (reduces yield strength).

The experimental results of final yield strength shown in Table 2 represent the maximum yield strength after 10 hours, which is 955 MPa. It means before 10 hours, the effect of mean radius increase dominates against the number density decrement and, as a result, the yield strength increases. After 10 hours, the effect of number density decrement overcomes the mean radius increase and yield strength reduces.

Table 2: Experimental results of yield strength of 718Plus as a function of aging time at 788 °C

	1 hr	5 hr	10 hr	25hr	50 hr
Yield Strength [MPa]	883	900	955	923	900

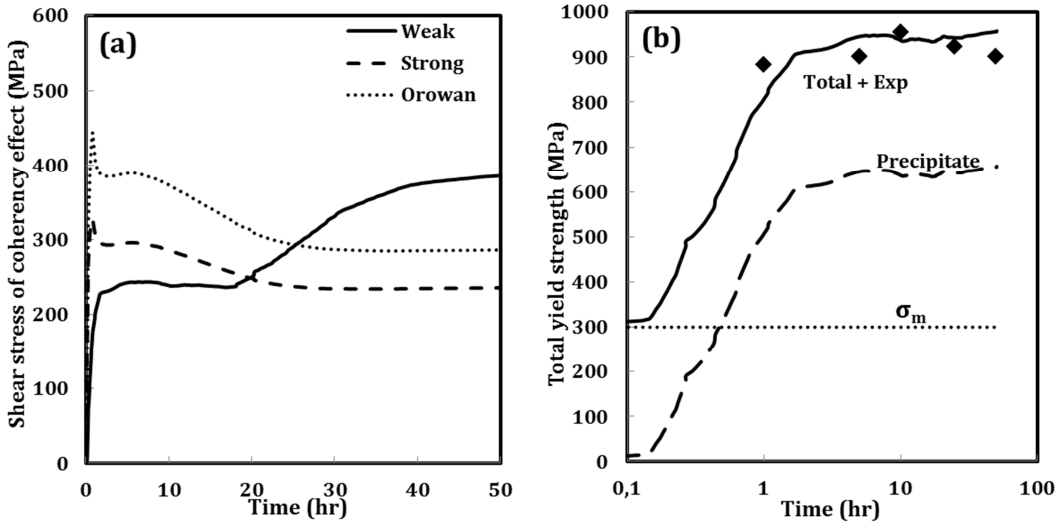

Fig. 3: Simulation of strengthening (a) coherency effect (b) contribution of all strengthening components in final yield strength.

Fig. 3(a) shows simulation results of weak and strong regimes in coherency strengthening independent of other mechanisms, as described in Eqs. 1-3, compared with the Orowan Eq. 6. It is apparent from Fig. 3 (a) that the weak strengthening mechanism defined in Eq. 1 strongly depends upon precipitate radius and has less dependency upon the precipitate free distance. Consequently, in the weak strengthening regime, the shear stress increases by precipitate coarsening during aging. The decrement in strong strengthening regime during aging is due to the weak dependency of strong strengthening equation on the precipitate radius, which results in strong dependency upon the precipitate free distance. Fig. 3 (a) indicates that the operative strengthening regime up to 20 hours is the weak regime, which is replaced by the strong strengthening regime later.
In the same way, the yield strength increase due to the APB effect based on Eqs. 4 and 5 can be simulated. The APB mechanism contributes to the final precipitation strengthening in addition to the coherency effect although this effect is not as significant as the coherency strengthening.
Eq. 7 defines the method used for calculation of total weak and strong precipitation strengthening considering coherency and APB effects. In this study, the γ' precipitate acts as a shearable precipitate even if it has an average diameter of 55 nm.
Fig. 3 (b) shows the magnitude of total yield strength in 718Plus where all the strengthening components except precipitation strengthening are held constant (≈300 MPa) during aging. As displayed in this plot, the main contribution to the total yield strength is the precipitation strengthening, which provides more that 65 % of the total yield strength at peak hardness.

5 Conclusion

- The final yield strength in 718Plus is a combination of contributions from grain boundary, solid solution strengthening, work hardening and precipitation strengthening, in which precipitation strengthening has the highest effect.
- Coherency and APB effects are the two significant strengthening components in the shearing mechanism, and simulation results show that coherency has stronger effect than APB.
- The lattice misfit between γ' precipitates and the matrix is small, consequently precipitates stay coherent even after a long aging time.
- Precipitation strengthening increases during aging when the phase fraction of γ' increases. At the peak of yield strength, the phase fraction of γ' is almost constant. Further aging leads to precipitate coarsening, which subsequently reduces the yield strength.

References:

[1] Information on http://www.matcalc.tuwien.ac.at/

[2] O.A. Idowu, O.A. Ojo, M.C. Chaturvedi, Effect of heat input on heat affected zone cracking in laser welded ATI Allvac 718Plus superalloy, Mater. Sci. and Eng. A 454–455 (2007) 389–397.

[3] W.D. Cao, US Patent No.: 6,730,264B2 (2004).

[4] L. Whitmore, H. Leitner, E. Povoden-Karadeniz, R. Radis, M. Stockinger, Transmission electron microscopy of single and double aged 718Plus superalloy, Mater. Sci. Eng. A 534 (2012) 413– 423.

[5] M.F. Ashby, 'The theory of the critical shear stress and work hardening of dispersion-hardened crystals', in: G.S. Ansell, T.D. Cooper, F.V. Lenel (Eds.), Metallurgical Society Conference, vol. 47, Gordon and Breach, New York, 1968, pp.143-205.

[6] R. Schnitzer, S. Zinner and H. Leitner, Modeling of the yield strength of a stainless maraging steel, Scripta Mater. 62 (2010) 286–289.

[7] LM. Brown, R.K. Ham, Strengthening Methods in Crystals Elsevier Publishing', ed. Kelly and R. B. Nicholson, Elsevier, Amesterdam, The Netherlands, 1971, pp. 9-135.

[8] V. Gerold, H. Haberkorn, On the critical resolved shear stress of solid solutions containing coherent precipitates, Phys Status Solidi (b) 16 (1966) 675-684.

[9] J. D. Eshelby, The determination of the elastic field of an ellipsoidal inclusion, and related problems, Proc. Roy. Soc. A241 (1957) 376-396.

[10] A. J. Ardell, Precipitation hardening, Metal. Trans. 16A (1985) 2131-2165.

[11] W. Huther, B. Reppich, Interaction of Dislocations with Coherent, Stress-Free, Ordered Particles, Z. Metallkunde, Bd. 69 (1978) 628-634.

[12] E. Orowan: Symposium on Internal Stresses in Metals and Alloys, Session III Discussion, Institute of Metals, London, England, (1948) 451-453.

[13] A. J. Ardell, J. C. Huang, Antiphase boundary energies and the transition from shearing to looping in alloys strengthened by ordered precipitates, Phil. Mag. Lett. 58 (1988) 189-197.

[14] B. Clausen, T. Lorentzen, T. Leffers, Self-consistent modelling of the plastic deformation of f.c.c. polycrystals and its implications for diffraction measurements of internal stresses, Acta mater. 46 (1998) 3087-3098.

Paper 5

Materials Science & Engineering A 608 (2014) 114–122

Contents lists available at ScienceDirect

Materials Science & Engineering A

journal homepage: www.elsevier.com/locate/msea

Yield strength prediction in Ni-base alloy 718Plus based on thermo-kinetic precipitation simulation

M.R. Ahmadi [a,b,*], E. Povoden-Karadeniz [b], L. Whitmore [c], M. Stockinger [d], A. Falahati [a], E. Kozeschnik [a,b]

[a] Institute of Materials Science and Technology, Vienna University of Technology, Favoritenstr. 9-11/E308, A-1040 Vienna, Austria
[b] Christian Doppler Laboratory "Early Stages of Precipitation", Institute of Materials Science and Technology, Vienna University of Technology, Favoritenstr. 9-11/E308, A-1040 Vienna, Austria
[c] Christian Doppler Laboratory "Early Stages of Precipitation", Department of Physical Metallurgy and Materials Testing, Montanuniversität Leoben, Franz-Josef Straße 18, 8700 Leoben, Austria
[d] Bohler Schmiedetechnik GmbH & Co KG, Mariazellerstr. 25, A-8605 Kapfenberg, Austria

ARTICLE INFO

Article history:
Received 14 February 2014
Received in revised form
10 April 2014
Accepted 16 April 2014
Available online 26 April 2014

Keywords:
Precipitation strengthening
Solid solution strengthening
Shearing mechanism
Precipitate radius
Precipitate resistance force

ABSTRACT

The yield strength of Allvac® 718Plus™ during aging is computed using integrated physical models that take into account intrinsic, grain boundary, solid solution and precipitate strengthening contributions. Precipitation strengthening of γ′ has the main effect on the final yield strength in this alloy during aging, with the coherency and anti-phase boundary effects providing the major strengthening contributions. We utilize transmission electron microscopy to obtain the unknown physical parameters entering the strengthening models and compare precipitate size and distribution with the simulation results.

1. Introduction

The performance of gas turbines and aero-engines can be improved by increasing the operating temperature of these devices. Whereas the Ni-base superalloy Inconel 718 shows superior mechanical properties up to 650 °C [1], the alloy Allvac® 718Plus™ (hereafter 718Plus) developed by ATI Allvac in 2004 can be operated at even 55 K higher service temperature. This advantage is accomplished by alloying with Co and W, and adjusting the Al/Ti ratio, altogether favoring the formation of ordered cubic $L1_2$-type $(Ni,Co)_3(Al,Ti,Cr,Nb,W)$ γ′ over tetragonal $D0_{22}$-type ordered metastable $(Ni)_3(Nb)$ γ″ [2]. To demonstrate the effect of alloying elements on the phase stabilities at high temperatures, in Fig. 1, the computed molar equilibrium phase fraction of γ′ and of metastable γ″ (the equilibrium phase δ suspended) with the thermodynamic database mc_ni_v2.003 [3] at 700 °C is presented as a function of the Al/Ti and Co/Fe ratios at constant weight fractions $w(Nb)=0.055$, $w(Mo)=0.03$, $w(Cr)=0.17$ and $w(Ti)+w(Al)=0.02$, $w(Co)+w(Fe)=0.18$, representing typical sums of γ′-forming alloying elements.

In contrast to the γ″ phase, which has a weakening effect on the material as it transforms to orthorhombic thermodynamic equilibrium Ni_3Nb (δ-phase) under long-term operation, γ′ remains stable and coherent even in over-aged conditions [1,4]. This should be beneficial in terms of precipitation strengthening, which is investigated in the present study by mechanical tensile testing combined with microstructural analysis using transmission electron microscopy (TEM). On comparison of the experimental results with our yield strength modeling and simulation, we were able to determine the prevailing physical strengthening mechanisms. For yield strength modeling, we used an integrated approach considering all types of contributions to the final yield strength (σ_y), which have been implemented in the solid-state transformation kinetics software MatCalc, version 5.60 (rel 0.005) [5–7] by the authors of this paper. In the description of strengthening mechanisms, the main focus is on the shearing of γ′ precipitates with anti-phase boundary (APB) and coherency effects. These are observed to be the dominating mechanisms over the modulus effect, since similar shear moduli of matrix and γ′ precipitates will not produce high resistance forces in front of a moving dislocation [8,9]. The interfacial effect is assumed to play only a minor role, too [9,10].

* Corresponding author at: Christian Doppler Laboratory for Early Stages of Precipitation, Institute of Materials Science and Technology, Vienna University of Technology, Favoritenstr. 9-11/E308, A-1040 Vienna, Austria. Tel.: +43 1 58801 30885; fax: +43 1 58801 30895.
E-mail address: mohammad.ahmadi@tuwien.ac.at (M.R. Ahmadi).

http://dx.doi.org/10.1016/j.msea.2014.04.054
0921-5093/

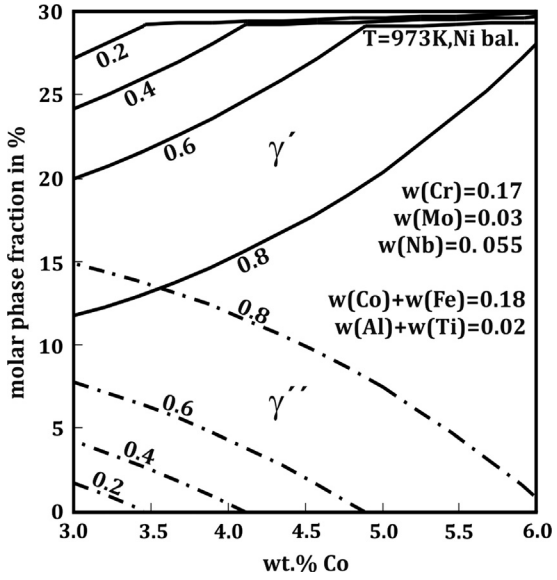

Fig. 1. Computed molar phase fractions of γ′ and γ″ (delta phase suspended in the calculation) at Al/Ti wt. ratios from 0.2 to 0.8 and varying Co-content.

Table 1
Chemical composition of 718Plus.

	Al	Co	Cr	Nb	C	Fe	Mo	Ti	W	Ni
wt. %	1.46	9.13	17.42	5.48	0.028	9.66	2.72	0.71	1.04	Balanced

2. Experimental

Hardness and compression tests of heat-treated 718Plus samples were used to analyze changes of precipitation hardening as a function of aging time. The composition of 718Plus used in this survey is given in Table 1.

A conventional heat treatment process is applied in this work. The specimens are solution annealed at 975 °C for 60 min, continued by water quenching and aging at 788 °C temperatures for different aging times (1, 5, 10, 25 and 50 h). Vickers hardness is determined using a Reichert-Jung Micro Duromat 4000 hardness tester equipped with a Vickers diamond pyramid indenter. The compression tests are reproduced twice for each point using a Bähr-Thermoanalyse DIL805A/D quenching and deformation dilatometer. The dimensions of the cylindrical specimens are 4 mm diameter and 8 mm length.

The specimens for TEM investigation are ground with silicon carbide paper to approximately 0.1 mm and electro-polished in a solution containing 5% perchloric acid and 95% ethanol at 32 V and −10 °C. They are cleaned in He plasma to remove all the oxides and impurities of the surface. An FEI Tecnai F20 FEGTEM is utilized at 200 kV acceleration voltage for microstructure analysis.

Transmission electron microscopy (TEM) was used to determine the mean radius, number density and phase fraction of the γ′ precipitates. Dark-field imaging was used to resolve the individual precipitates, combining the diffracted beams arising from the unique chemical ordering of the γ′ phase. Approximately 1000 precipitates were measured in Digital Micrograph for each heat treatment to determine the mean radius. Number density and phase fraction were calculated by measuring the number of precipitates in a known volume of the specimen. The volume was determined by area measurement from TEM images and thickness measurement using electron energy-loss spectroscopy (EELS) and the standard log-ratio method described in [4]. Only regions less than 100 nm thickness were used for this analysis to avoid inaccuracy due to overlap of precipitates. A correction factor was applied, according to the procedure described in [4], to correct for the fact that a proportion of precipitates intersect the foil surface.

3. Modeling of precipitation

To calculate the nucleation rate J of γ′ precipitates per unit volume and time, the classical nucleation theory [11] is used:

$$J = N_0 Z \beta^* \exp\left(\frac{-G^*}{k_B T_k}\right) \exp\left(\frac{\tau_{incub}}{t}\right), \quad (1)$$

where N_0 is the number of potential nucleation sites, Z is the Zeldovich factor, β^* is the condensation rate of solute atoms at a cluster of critical size, k_B is the Boltzmann constant, T_k is temperature, G^* is the energy required to form a nucleus of critical radius, τ_{incub} is the incubation time and t is time. G^* depends on the chemical driving force evaluated by CALPHAD-type thermodynamic parameters stored in mc_ni_v2.003, and the interfacial energy between matrix and precipitate. The interfacial energy is evaluated with the generalized broken bond (GBB) approach as described in Ref. [12] and taking into account interfacial curvature size effects [13].

The precipitate growth kinetics is simulated with the SFFK mean-field model for multi-component multi-phase systems [5,6]. In a precipitation environment of an arbitrary number of spherical particles nucleating and growing in a unit volume of matrix phase, the total Gibbs energy of the system is described by

$$G = \sum_{i=1}^{n} N_{0i}\mu_{0i} + \sum_{k=1}^{m} \frac{4\pi\rho_k^3}{3}\left(\lambda + \sum_{i=1}^{n} c_{ki}\mu_{ki}\right) + \sum_{k=1}^{m} 4\pi\rho_k^2\gamma, \quad (2)$$

where N_{0i} is the number of moles of component i in the matrix phase and λ is the contribution from elastic energy. μ, ρ and c denote chemical potential, radius and concentration, respectively. The index k refers to the index of individual precipitate size classes [6].

During isothermal heat treatment, the total free energy of the system decreases and the precipitate microstructure evolves. The difference in free energy between the initial and the evolved state is dissipated. The free energy dissipation takes place by interface movement, diffusion of atoms inside of the precipitates and diffusion of atoms in the matrix. The total rate of dissipation is given as the sum of these individual contributions. The rate of total free energy change is connected with the free energy dissipation rate using the thermodynamic extremum principle [14–16], and the system evolution is given by a set of linear equations, in which the rate of radius and chemical composition change of each precipitate is evaluated. To determine the evolution of the entire precipitate population, the rate equations are integrated numerically under the constraint of mass conservation. The integration is carried out based on the numerical Kampmann–Wagner approach [6,17]. For every time increment in the precipitation simulation and for each precipitating phase, the growth kinetics and the change in composition are evaluated based on the evolution equations [5] and the nucleation rate expression Eq. (1). Further details about the models and the numerical treatment of the evolution equations are given by Svoboda et al. [5] and Kozeschnik [18]. In MatCalc, the evolving precipitate properties under user-defined heat treatments are directly used for the simulation of yield strength.

4. Yield strength modeling

The final yield strength (σ_y) in annealed crystalline materials is constituted by grain boundary strengthening ($\sigma_{y,g}$), solid solution

strengthening ($\sigma_{y,s}$) and precipitation strengthening ($\sigma_{y,p}$), which are simply combined linearly [19] as

$$\sigma_y = \sigma_{y,g} + \sigma_{y,s} + \sigma_{y,p}. \quad (3)$$

In the following, the models for individual strengthening contributions to σ_y are briefly reviewed.

4.1. Grain boundary effect

Grain boundaries act as impenetrable barriers for dislocation movement, and contribute, together with the friction stress σ_i, to the yield strength of a crystalline matrix. This concept was formulated by Hall [20] and expanded by Petch [21] as

$$\sigma_{y,g} = \sigma_i + \frac{k_{lock}}{\sqrt{D}} \quad (4)$$

where σ_i is the friction stress of the crystal lattice to dislocation movement, k_{lock} is the locking parameter of grain boundary hardening and D is the grain diameter [21,22]. Thompson [23] determined the friction stress of Ni-based superalloys as $\sigma_i = 21.8$ MPa and $k_{lock} = 0.158$ MPa m$^{1/2}$.

4.2. Solid solution strengthening

The common equation describing the solid solution strengthening effect as reviewed by Butt [24] is

$$\sigma_{y,s,i} = k_{s,i} C_i^p. \quad (5)$$

here, $k_{s,i}$ is a strengthening constant for solute i, C_i is the concentration of solute i and p is a constant that, in general, varies between 1/2 and 1 [25]. $\sigma_{y,s,i}$ defines the yield strength increment due to solute i. In the proposed model of Labusch [26] and Nabarro [27], p is 2/3 although, in the case of superalloys, Felthman [28] proposed a value of $p = 1/2$.

To evaluate the yield strength in multicomponent systems, Gypen and Deruyttere [29] proposed a method to integrate the overall yield strength increment of different alloying components based on the following equation:

$$\sigma_{y,s} = \left(\sum_i (k_{s,i} C_i^p)^q \right)^{1/q} \quad (6)$$

where $q = 2$ and $p = 1/2$.

The strengthening constants $k_{s,i}$ of alloying elements found in Eqs. (5) and (6) are indispensable for the evaluation of the solid solution strengthening effect for $\sigma_{y,s}$. Mishima et al. [30] defined $k_{s,i}$ experimentally for different alloying elements in binary systems Ni–X, with X being an element from the transition metal group. Their results are summarized in Table 2. Later, Roth et al. [31] used these constants in a multi-component Ni-base system and found good agreement between experimental and simulation results, using the model for solid solution strengthening proposed by Feltham [28] and given in Eq. (6).

4.3. Precipitation strengthening

At the early stages of aging of heat-treatable alloys, coherent precipitates with sizes ranging from close to unit cell up to a few nanometers govern the precipitation strengthening contribution to σ_y. Lattice continuity (coherency) prevails at the precipitate–matrix interface, and the precipitate resistance force F is not high enough to bend an approaching dislocation strongly. This interaction between precipitate resistance force F in front of dislocation movement and the dislocation line tension T needs to be examined in order to distinguish the different regimes of precipitation strengthening from each other. Fig. 2 represents this relation for the case of early precipitation of coherent particles.

Fig. 2(A) shows a situation where the outer cut-off angle Ψ_c lies inside the limits of 120° and 180°. This region confines the regime of weak and shearable precipitates. Under prolonged aging, the precipitate resistance force increases as a consequence of increasing precipitate size and the outer cut-off angle Ψ_c decreases from 120° to 0°. This region confines the regime of strong and shearable precipitates (Fig. 2(B)).

Finally, for continued aging, precipitates often lose coherency or the precipitate resistance force in front of the dislocation movement increases beyond $2T$, $\Psi_c = 0°$. The precipitates are then no longer sheared by dislocations. This situation is shown in Fig. 2 (C). Non-shearing precipitates are by-passed by the dislocation, leaving behind a dislocation ring around the precipitate (Orowan mechanism).

4.3.1. Shearing mechanisms

A specific feature of 718Plus is that the strengthening particles $(Ni,Co)_3(Al,Ti,Cr,Nb)$ γ' remain coherent even after thousands of hours in service. This makes 718Plus a suitable model system to investigate the different strengthening contributions related to shearing. These are (i) coherency strengthening, (ii) anti-phase boundary (APB) strengthening, (iii) modulus strengthening and (iv) interfacial strengthening. The models describing these effects are reviewed in the following.

4.3.1.1. Coherency effect. The difference between lattice parameter of the precipitate and matrix produces a strain field around the precipitate, which interacts with the moving dislocation. Brown and Ham [32] proposed a shear strengthening equation for weak

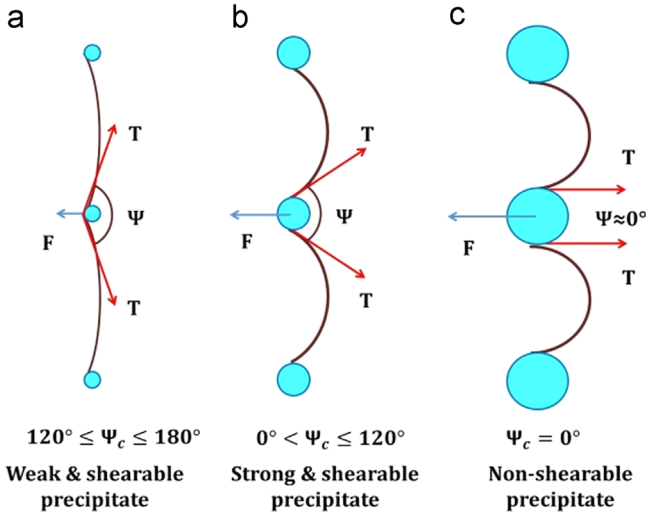

Fig. 2. Schematic interaction between a dislocation and precipitates with different sizes.

Table 2
$k_{s,i}$ Strengthening constants of different alloying elements in Ni, from Ref. [30].

Alloying element	Al	Co	Cr	Nb	C	Fe	Mo	Ti	W
Strengthening constant (MPa at Fraction$^{-1/2}$)	225	39.4	337	1183	1061	153	1015	775	977

and shearable precipitates based on Gerold and Haberkorn's [33] coherency model as follows:

$$\tau_{\mathrm{Coh,weak}} = k\left(\frac{G^3 b\varepsilon^3 r^3}{L_s^2 T(\theta)}\right)^{1/2}, \tag{7}$$

with

$$\varepsilon = \frac{1}{3}\left(\frac{1+\upsilon}{1-\upsilon}\right)\frac{\Delta a}{a}, \tag{8}$$

and

$$T(\theta) = \frac{Gb^2}{4\pi}\left(\frac{1+\upsilon-3\sin^2\theta}{1-\upsilon}\right)\ln\left(\frac{r_o}{r_i}\right) \tag{9}$$

k is a constant equal to 4.11 and 1.38 for edge and screw dislocation, respectively [9,32]. G is the shear modulus, b is the Burgers vector, r is the precipitate mean radius and L_s is the surface-to-surface distance between two precipitates. In Eq. (8), υ is Poisson's ratio, ε is the constrained strain produced by the stress free strain of linear lattice misfit δ [34], a is the lattice parameter of the matrix and Δa is the difference between lattice parameters of matrix and precipitate.

For shearable precipitates, the outer cut-off distance, r_o, is the distance between two particles along the dislocation line [9,32]. r_i is the inner cut-off distance, which is the dislocation core radius with values between b and $4b$ [9] and θ is the angle between the dislocation line and its Burgers vector in Eq. (9).

For strong and shearable precipitates, Brown and Ham [32] proposed the following strengthening equation:

$$\tau_{\mathrm{Coh,strong}} = \frac{m}{L_s}\left(\frac{T^3(\theta)G\varepsilon r}{b^3}\right)^{1/4}, \tag{10}$$

where m is equal to 2.1 and 2 for edge and screw dislocation, respectively.

The surface-to-surface distance between two particles is a key factor in the evaluation of precipitation strengthening. Sonderegger et al. [35] proposed a statistical model for the free distance between randomly distributed spherical particles as

$$L_s = \sqrt{\frac{\ln 3}{2\pi\sum_c n_{v,c} r_c} + (2r_{ss})^2} - 2r_{ss} \tag{11}$$

and

$$r_{ss} = \sqrt{\frac{2}{3}}\frac{\sum_c n_{v,c} r_c^2}{\sum_c n_{v,c} r_c}. \tag{12}$$

where r_c and $n_{v,c}$ are specific radius and number density of particles in an array of size classes.

4.3.1.2. Anti-phase boundary effect. Strengthening by the anti-phase boundary effect occurs when dislocations shear ordered particles. During shearing, the dislocations modify the local nature of chemical atomic bonds in the slip plane and produce energetically unfavorable atomic ordering in the precipitates. The shearing dislocations travel in groups, where the number of dislocations in a group depends on the type of order structure (e.g. face-centered cubic $L1_2$, tetragonal $D0_{22}$) and is important for the ability of precipitates to restore to the perfect order structure after the precipitate–dislocation interaction. The leading dislocation creates an anti-phase boundary in the precipitate and the trailing dislocation compensates the effect of the first one and restores the ordered structure again.

For weak precipitates, this mechanism contributes to the shear strength as [36]

$$\tau_{\mathrm{APB,weak}} = \left\{\frac{2T}{bL_s}\left[\frac{\pi\gamma_{\mathrm{APB}} r}{4T}\right]^{3/2} - \beta\frac{\pi}{3}\frac{\gamma_{\mathrm{APB}} r^2}{bL_s^2}\right\}, \tag{13}$$

where γ_{APB} is the anti-phase boundary energy of the precipitate and β is a constant between 0 and 1. As the trailing dislocation is expected to be straight, β is chosen to be close to 0.5, here [36].

For strong and shearable ordered precipitates, we utilize the expression proposed by Hüther and Reppich [37] with

$$\tau_{\mathrm{APB,strong}} = \left(\frac{2wT}{\pi bL_s}\right)\left(\frac{\pi^2\gamma_{\mathrm{APB}} r}{4wT} - 1\right)^{1/2} \tag{14}$$

where w is a parameter introduced for incorporation of the effect of remaining dislocation segments as well as some other uncertainties. Its value is assumed to be 2.8.

4.3.1.3. Modulus strengthening effect. If the dislocation energy inside and outside the precipitate varies due to different shear moduli of the precipitate and the matrix, this energy difference potentially improves the shear stress. For the weak mechanism, Nembach [38] obtained

$$\tau_{\mathrm{Mod,weak}} = \frac{2T}{bL_s}\left[\frac{\omega_1|G_p - G|b^2(\pi r/4b)^{\omega_2}}{2T}\right]^{3/2}, \tag{15}$$

where ω_1 and ω_2 are two constants equal to 0.05 and 0.85, respectively. G_p is the shear modulus of the precipitate. For strong and shearable precipitates, the modulus effect is represented as [9,32]

$$\tau_{\mathrm{Mod,strong}} = \frac{\omega_1|G_p - G|b^2(\pi r/4b)^{\omega_2}}{bL_s}. \tag{16}$$

4.3.1.4. Interfacial effect. A shearing dislocation produces two ledges after entering and leaving a precipitate. This increases the interfacial area in the affected regions, yielding an increase of yield strength as [9,32]

$$\tau_{\mathrm{Chem,weak}} = \frac{2T}{bL_s}\left[\frac{\gamma_{\mathrm{IFE}} b}{T}\right]^{3/2}, \tag{17}$$

for the weak mechanism and

$$\tau_{\mathrm{Chem,strong}} = \frac{2\gamma_{\mathrm{IFE}} b}{bL_s}, \tag{18}$$

for strong shearable precipitates. γ_{IFE} is the energy of the precipitate–matrix interface created by the shearing dislocation.

4.3.1.5. Superposition of shearing mechanisms. For the simultaneous effect of different shearing mechanisms to the total shearing stress, Ardell [9] proposed the following expression for the superposition of individual strengthening mechanisms:

$$\sigma_{y,p} = M(\tau_{\mathrm{Coh}}^q + \tau_{\mathrm{APB}}^q + \tau_{\mathrm{Mod}}^q + \tau_{\mathrm{Chem}}^q)^{1/q}, \tag{19}$$

where M is the average value for converting shear stress to tensile stress. In fcc polycrystalline materials, $M \approx 2.6$ [39]. q is an exponent, which lies between 1 and 2. Ardell [9] proposed a value of $q=1.8$ for contributions of different weak or different strong regimes.

4.3.2. Non-shearing mechanism

The strengthening formalism for spherical non-shearable precipitates described in Fig. 2(c) was developed by Orowan [40] and

modified to the generally accepted form by Brown and Ham [32] as

$$\sigma_{\text{Orowan}} = \frac{MGb}{2\pi\sqrt{1-\upsilon}} \frac{1}{L_s} \ln\left(\frac{\pi}{2}\frac{r}{r_i}\right). \quad (20)$$

This expression is utilized in the present investigation.

5. Result and discussion

In this section, the computed influence of grain size and solid solution strengthening on the yield strength of 718Plus is discussed. Then, the models of Section 4 are used for the simulation of precipitation strengthening. MatCalc version 5.60 (rel 0.005) is applied for all types of equilibrium and kinetic simulations. The thermodynamic database *mc_ni_v2.003.tdb* and the diffusion database *mc_ni_v2.003.ddb* are used in the thermo-kinetic simulations [3].

5.1. Grain size effect

In Nb-containing Ni-base superalloys, the δ phase is responsible for pinning of grain boundaries and, thus, limits free grain growth at high temperatures. This, in turn, means that the grain size strongly depends on the applied solution annealing temperature. In the present study, solution annealing below 1000 °C is applied, which is below the solvus of the δ phase in 718Plus. As a consequence, the measured grain size of 718Plus after quenching is small, approximately 20 μm, and the grain size effect produces an increment in the final yield strength equal to $\sigma_{y,g} = 56$ MPa (see Section 4.1).

5.2. Solid solution effect

Fig. 3 shows the evolution of the computed solid solution yield strength contributions of individual alloying elements in 718Plus during isothermal aging at 788 °C based on the results of the thermo-kinetic precipitation simulation (see next Section 5.3) and the strengthening parameters discussed in Section 4.2. After quenching and before aging, Nb has the strongest effect in solid solution strengthening (≈ 200 MPa) and Co has the weakest effect (≈ 12 MPa). During aging, the important effect of Nb diminishes, as Nb migrates from the matrix into the γ′ precipitates. The same applies to the γ′-forming elements Al and Ti. In summary, using the suggested $k_{s,i}$ values shown in Table 2 in the yield strength computation, we observe a decreasing $\sigma_{y,s}$ as a function of aging time. The remaining elements, such as Cr and Mo, which prefer to be dissolved in the matrix, cannot compensate for the loss of Nb, Al and Ti due to the formation of γ′.

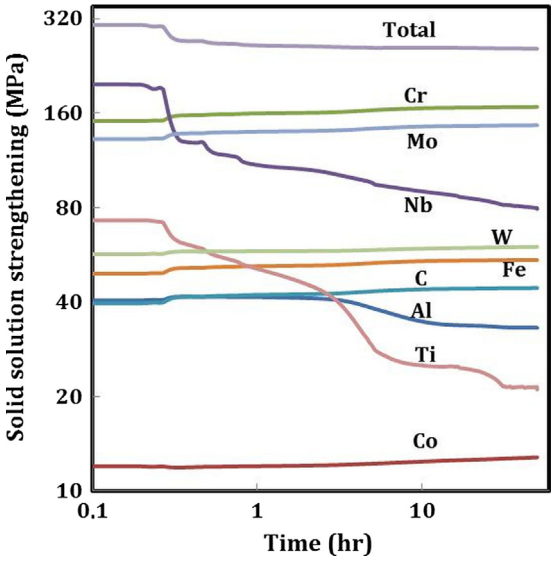

Fig. 3. Computed solid solution yield strength increments of different alloying elements based on the thermo-kinetic precipitation simulation.

5.3. Precipitation hardening effect

5.3.1. Experimental results

The precipitation strengthening equations in Section 4.3 build upon the knowledge of the number density and mean radii of precipitates from the thermo-kinetic simulation. Accordingly, the yield strength increases roughly proportional to the precipitate mean radius r and number density N_s, and inversely proportional to the precipitate free distance L_s. Consequently, the final yield strength after a specific heat treatment can be evaluated, if the precipitate distribution (number density and mean radii) and precipitate properties (lattice mismatch, etc.) are known. Experimentally, we have obtained these parameters by transmission electron microscopy (TEM) analysis. For isothermally heat-treated 718Plus, the evolution of the γ′ precipitate population is characterized by dark field TEM as shown in Fig. 4.

The size of the spherical γ′precipitates increases with aging time due to precipitate coarsening, while the number density of particles decreases. Fig. 5 shows the experimental points of the TEM measurements for (a) mean radius, (b) number density and (c) phase fraction of γ′ precipitates during the heat treatment together with the results of the thermo-kinetic simulation.

5.3.2. Simulation results

Fig. 5 demonstrates that the trends of the simulated γ′ precipitate sizes (a) and number densities (b) reproduce the experimental data well. The mean radius increases during aging, while the number density of γ′ precipitates decreases. The thermo-kinetic precipitation results are used as input parameters for the yield strength simulation, next.

Fig. 6(a) compares the simulated coherency strengthening effect in the weak and strong regimes to predictions based on the Orowan mechanism for γ′ precipitates. The lowest strengthening value is assumed to define the operative strengthening mechanism. The input parameters of our simulations are summarized in Table 3, where we have used strengthening parameters from the literature as well as parameters obtained from our present microstructural investigation. From the results, we observe that the weak strengthening regime depends mainly on the precipitate radius, which increases strongly in the first hours of heat treatment and continues to increase due to coarsening (Ostwald ripening). On the other hand, a decreasing coherency strengthening effect is observed during coarsening as a function of aging time in the strong strengthening regime. This behavior is related to the weak dependency of the coherency strong regime on the precipitate radius relative to the precipitate free distance according to Eq. (10).

Fig. 6(b) analyzes the computed individual yield strength increment due to the APB effect. This effect is stronger than the coherency effect. Somewhere in the middle of the present heat treatment, the strong mechanisms for anti-phase boundary strengthening replace the weak mechanisms. Fig. 6(c) shows the yield strength increase due to the modulus strengthening effect. Since the shear modulus of γ′ precipitates is close to the values of the 718Plus matrix (see Table 3), this effect makes up for a value of less than 10 MPa. The chemical effect is even more insignificant than the modulus effect; less than 5 MPa strengthening for the weak mechanism is computed (see Fig. 6 (d)).

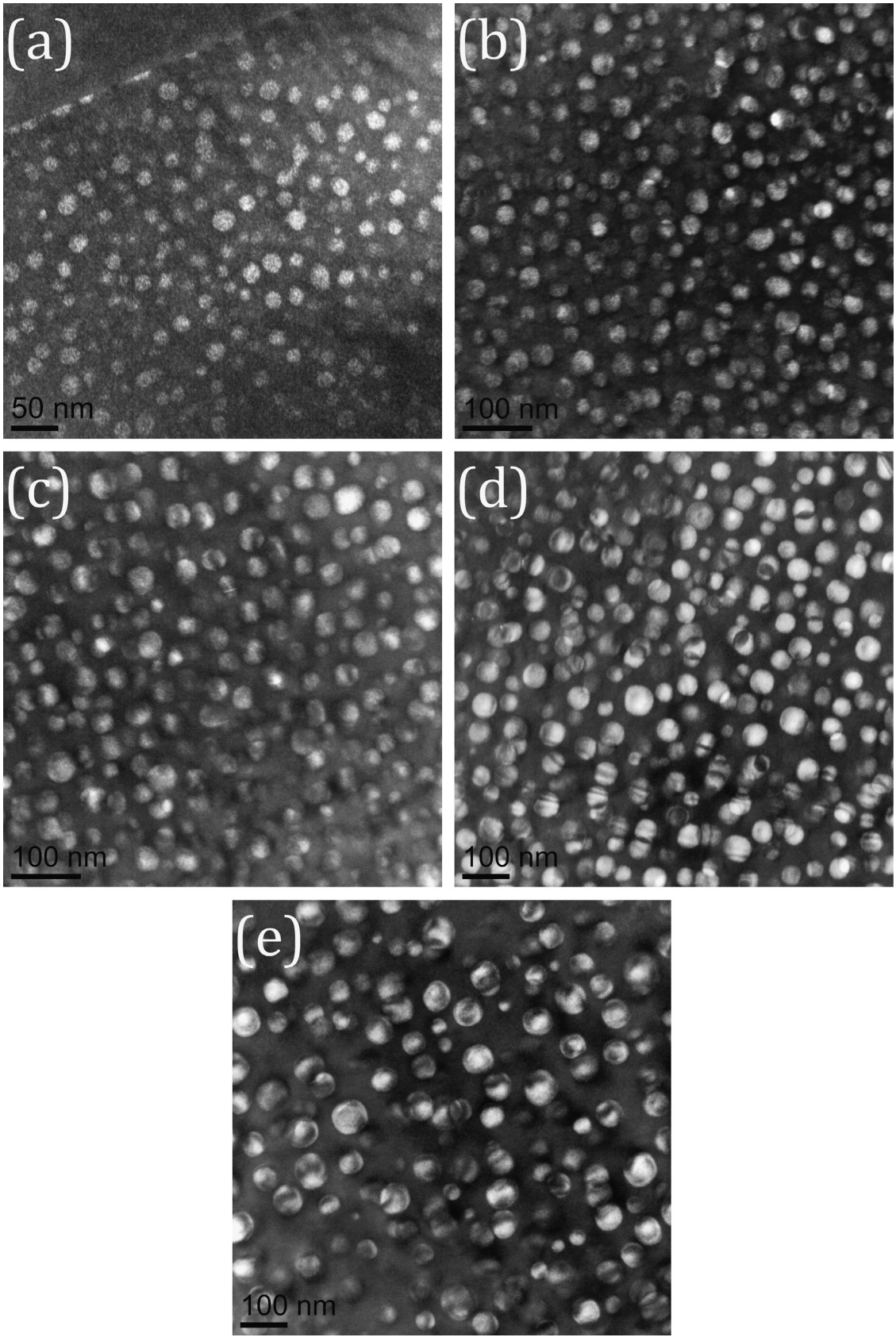

Fig. 4. Dark field images of 718Plus during aging at 788 °C for different times: (a) 1 h, (b) 5 h, (c) 10 h, (d) 25 h, and (e) 50 h.

Fig. 6(e) illustrates the simulated contributions of weak and strong regimes obtained from the coherency, APB, modulus and interfacial effects. From the plot, it is evident that the operative strengthening mechanism in 718Plus aged at 788 °C is weak and shearable at the early aging hours (before 10 h aging) and non-shearable at prolonged aging.

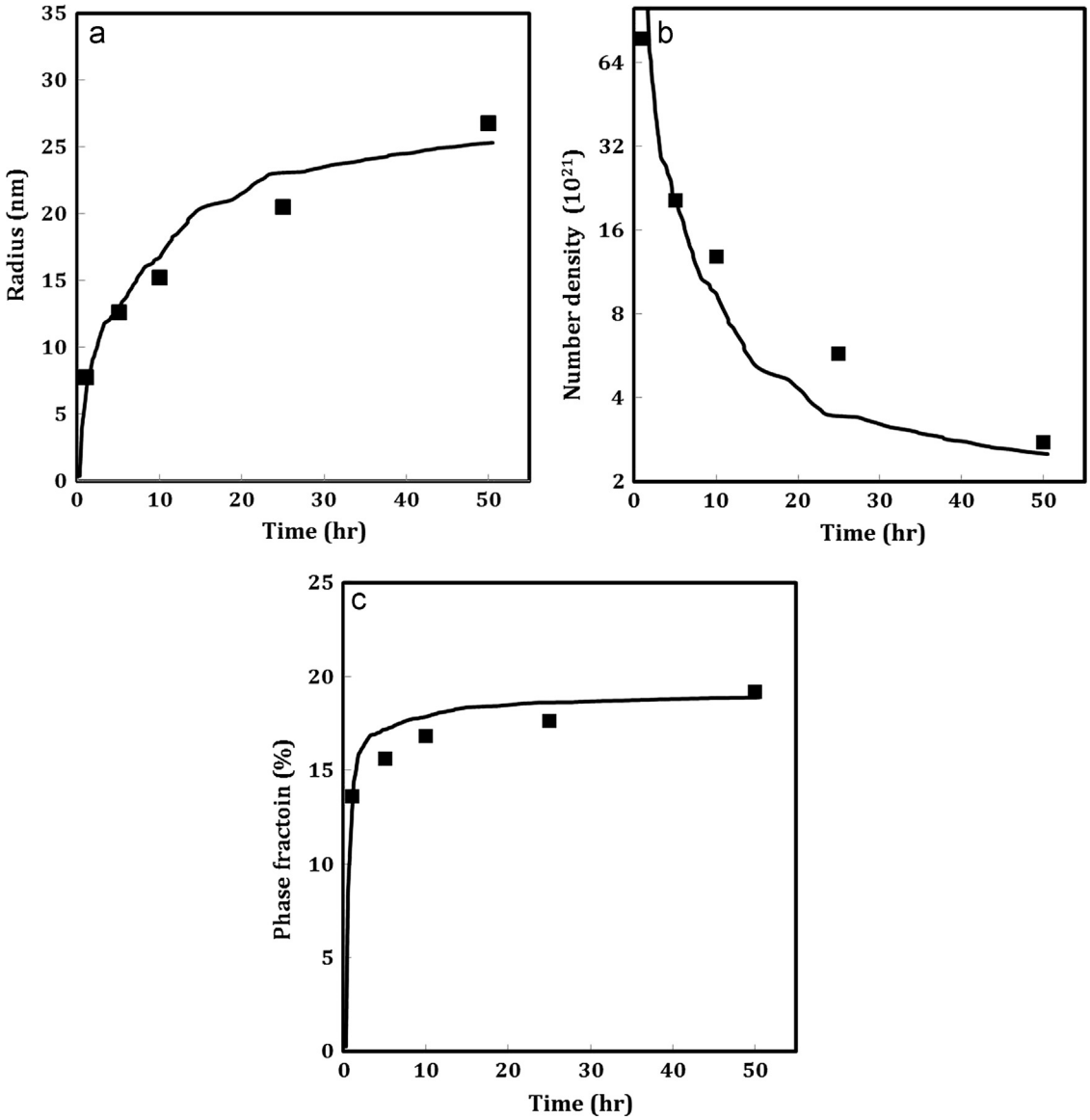

Fig. 5. Simulation result of (a) mean radii, (b) number densities and (c) phase fractions of γ′ aged at 788 °C compared with experimental TEM results (symbols).

The experimental total yield strength values, σ_y, illustrated in Fig. 6(f) show a maximum at $\sigma_y = 1095$ MPa after 10 h. From the simulation results, we conclude that, before 10 h, nucleation and growth of γ′ precipitates prevail and, thus, the effect of radius increment dominates over the effect of number density decrement during coarsening. This is also visible by a rapid increase in the volume fraction evolution, Fig. 5(c), in the first 10 h. The approximately constant volume fraction of γ′ is located inside the region of coarsening, where a yield strength reduction is observed.

Fig. 3 gives a clear indication of the relation between solid solution strengthening and precipitate evolution from nucleation and growth to coarsening. The yield strength due to constitutional alloying elements of γ′, such as Nb, Ti and Al, decreases at early aging time up to 10 h. Afterwards, the concentration of each alloying element in the matrix becomes almost constant and, thus, also the solid solution strengthening effect.

Fig. 6(f) summarizes our computed total yield strength evolution, σ_y, in 718Plus compared with results from compression tests, as well as the simulated contribution of individual strengthening contributions from intrinsic strength and grain size effect, solid solution strengthening and precipitation strengthening during isothermal aging at 788 °C. The grain size and intrinsic effects are practically constant because the grain size is unchanged during aging. The predicted decreased solid solution strengthening during aging is by far compensated by the amount of precipitation strengthening, which provides more than 65% of the total yield strength at peak strength.

6. Conclusion

Within a comprehensive computational framework for the evolution of precipitates during thermo-mechanical treatment, we demonstrate that the yield strength of the Ni-base superalloy Allvac 718Plus can be accurately predicted over the entire heat treatment cycle. The coupling of yield strength simulation with thermo-kinetic computation of the precipitate evolution shows that precipitation strengthening increases significantly with the volume fraction increase of γ′ precipitates. At peak strength, the phase fraction of γ′ becomes almost constant. Precipitate coarsening during prolonged aging at 788 °C has a negative effect on the final yield strength. The yield strength simulation, which is based on physical modeling and thermo-kinetic precipitation simulation, suggests that before 10 h aging, the operative strengthening

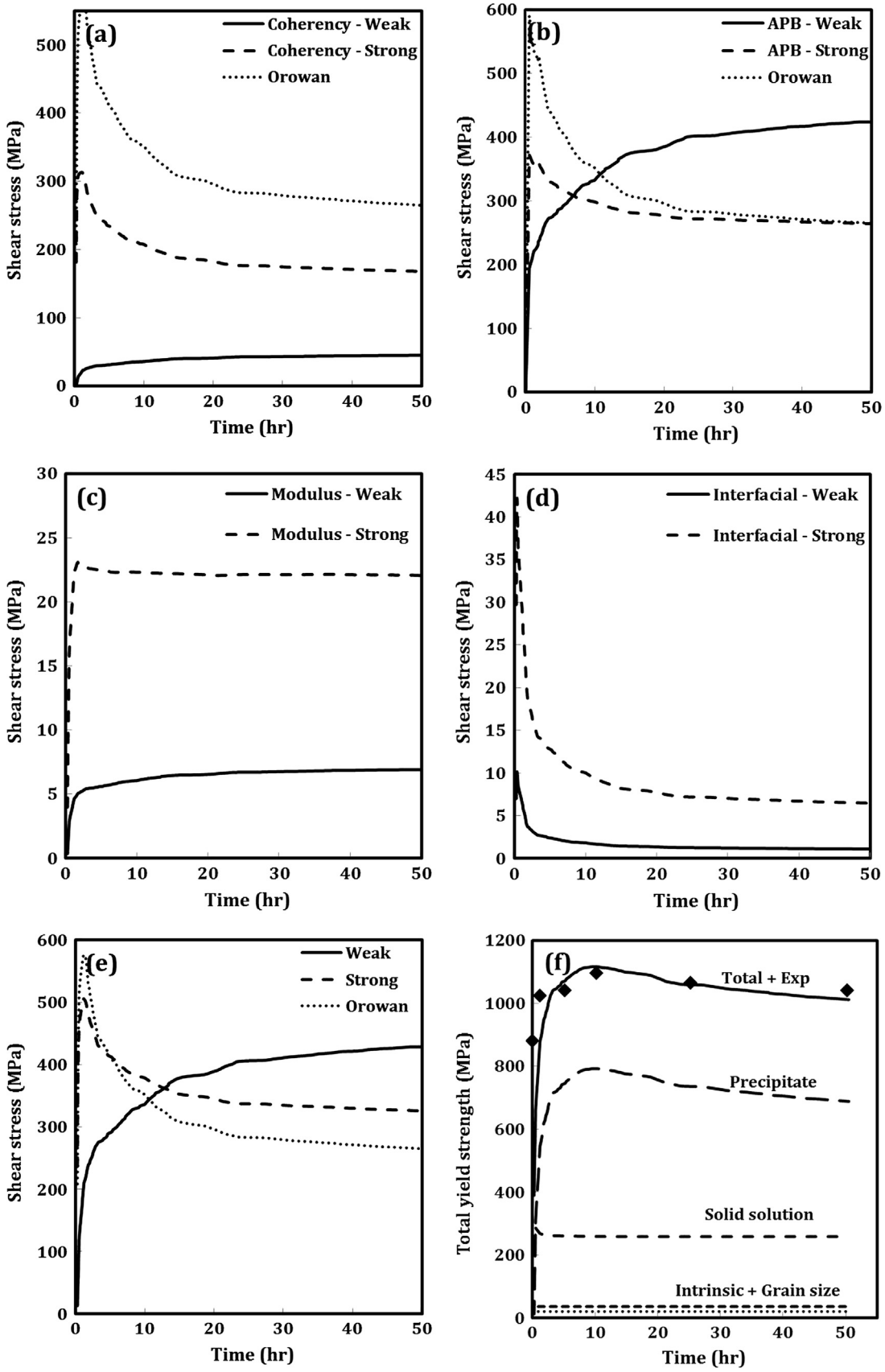

Fig. 6. Simulation result of strengthening; (a) coherency effect, (b) APB effect, (c) modulus effect, (d) interfacial effect, (e) combination of all weak and strong shearing mechanisms and (f) contribution of all strengthening components to σ_y. Results of compression tests are included (symbols).

Table 3
Strengthening parameters used in the precipitation hardening simulation.

Parameters	Values	Comments
M (Taylor factor)	2.6	From Ref. [39]
G (GPa)	80.1	From Ref. [41]
G_P (GPa)	77.8	From Ref. [8]
γ_{APB} (J m^{-2})	0.111	From Ref. [42]
γ_{IF} (J m^{-2})	0.135–0.16[a]	MatCalc thermodynamic database
δ	0.004	Measured
b (nm)	0.254	
ν	0.33	
r_i	2b	

[a] The interfacial energy is composition- and temperature-dependent.

mechanism in 718Plus is shearing. Afterwards, the strengthening is provided by the non-shearing mechanism. The dominant shearing mechanisms are the anti-phase boundary and coherency effects, which have the highest impact on the final yield strength in 718Plus.

References

[1] O.A. Idowu, O.A. Ojo, M.C. Chaturvedi, Mater. Sci. Eng. A 454–455 (2007) 389–397.
[2] W.D. Cao, US Patent No. 6,730,264B2, 2004.
[3] ⟨http://matcalc.tuwien.ac.at/⟩ (accessed 07.02.14).
[4] L. Whitmore, H. Leitner, E. Povoden-Karadeniz, R. Radis, M. Stockinger, Mater. Sci. Eng. A 534 (2012) 413–423.
[5] J. Svoboda, F.D. Fischer, P. Fratzl, E. Kozeschnik, Mater. Sci. Eng. A 385 (2004) 166–174.
[6] E. Kozeschnik, J. Svoboda, P. Fratzl, F.D. Fischer, Mater. Sci. Eng. A 385 (2004) 157–165.
[7] E. Kozeschnik, J. Svoboda, F.D. Fischer, Calphad 28 (4) (2005) 379–382.
[8] Yun-Jiang Wang, Chong-Yu Wang, Chin. Phys. B 18 (2009) 4339–4348.
[9] A.J. Ardell, Metall. Trans. 16A (1985) 2131–2165.
[10] I. Holzer, E. Kozeschnik, Mater. Sci. Eng. A 527 (2010) 3546–3551.
[11] K. Russell, Adv. Colloid Interface Sci. 13 (1980) 205–318.
[12] B. Sonderegger, E. Kozeschnik, Metall. Mater. Trans 40A (2009) 499–510.
[13] B. Sonderegger, E. Kozeschnik, Scr. Mater. 60 (2009) 635–638.
[14] L. Onsager, Phys. Rev. 37 (1931) 405–426.
[15] L. Onsager, Phys. Rev. 38 (1931) 2265–2279.
[16] J. Svoboda, I. Turek, F.D. Fischer, Philos. Mag. 85 (2005) 3699–3707.
[17] R. Kampmann, R. Wagner, Acta Scr. Met. Ser. (1984) 91–103.
[18] Ernst Kozeschnik, Modeling Solid-State Precipitation, Momentum Press, LLC, New York, NY, 2013 (First Published by Momentum Press®, LLC).
[19] R. Schnitzer, S. Zinner, H. Leitner, Scr. Mater. 62 (2010) 286–289.
[20] E.O. Hall, Proc. Phys. Soc. London B 64 (1951) 747–753.
[21] N.J. Petch, J. Iron Steel Inst. 174 (1953) 25–28.
[22] G.E. Dieter, Mechanical Metallurgy, third ed., MaGraw-Hill Book Co., New York, NY, USA, 1986.
[23] Anthony A.W. Thompson, Acta Metall. 23 (1975) 1337–1342.
[24] M.Z. Butt, J. Mater. Sci. 28 (1993) 2557–2576.
[25] T. Suzuki, Jpn. J. Appl. Phys. 20 (1981) 449–462.
[26] R. Labusch, Acta Metall. 20 (1972) 917–927.
[27] F.H.N. Nabarro, Philos. Mag. 35 (1977) 613–622.
[28] P. Feltham Br, J. Appl. Phys. 1 (1968) 303–308.
[29] L.A. Gypen, A. Deruyttere, J. Mater. Sci. 12 (1977) 1028–1038.
[30] Y. Mishima, S. Ochiai, N. Hamao, M. Yodogawa, T. Suzuki, Trans. Jpn. Inst. Met. 27 (1986) 656–664.
[31] H.A. Roth, C.L. Davis, R.C. Thomson, Metall. Mater. Trans. A 28 (1997) 1329–1335.
[32] LM. Brown, R.K. Ham, in 'Strengthening Methods in Crystals Elsevier Publishing', ed. Kelly and R. B. Nicholson, Elsevier, Amesterdam, The Netherlands, 1971, pp. 9–135.
[33] V. Gerold, H. Haberkorn, Phys. Status Solidi B 16 (1966) 675–684.
[34] J.D. Eshelby, Proc. R. Soc. A 241 (1957) 376.
[35] B. Sonderegger, I. Holzer, E. Kozeschnik, Ch. Sommitsch, Comp. Methods Mater. Sci. 11 (2011) 148–153.
[36] E. Nembach, Prog. Mater. Sci. 45 (2000) 275–338.
[37] W. Huther, B. Reppich, Z. Metall. 69 (1978) 628–634.
[38] E. Nembach, Phys. Status Solidi A 78 (1983) 571–581.
[39] B. Clausen, T. Lorentzen, T. Leffers, Acta Mater. 46 (1998) 3087–3098.
[40] E. Orowan, Symposium on Internal Stresses in Metals and Alloys, Session III Discussion, Institute of Metals, London, England, 1948, pp. 451–453.
[41] F.J. Garcia-Revillo Sanz, Optimum Design Methodology for a Test Rig Turbine Disc (Final thesis), School of Engineering (ICAI) Mechanical Engineering, Comillas Pontifical University, Madrid, Spain, 2013.
[42] J. Douin, P. Veyssiere, P. Beauchamp, Philos. Mag. A 41 (1986) 21.